



THE ATOMIC-SCALE LIMITS OF MAGNETISM AND SUPERCONDUCTIVITY EXPLORED BY ELECTRON EXCITATIONS IN TUNNELING SPECTROSCOPY

DOCTORAL THESIS

by Carmen Rubio Verdú

Supervised by Prof. José Ignacio Pascual Chico

Donostia, January 2019

A mis padres, Carmen y Juan.

A mis iaios, Lola y Juan.

A mis abuelos, Carmen y Fernando.

Abstract

Understanding the energy scales that govern magnetism in a single atom provides the ultimate piece of information towards its application into new technologies such as organic spintronics. Its realization depends on the efficient interaction of electron current with spins. Therefore, a fundamental approach towards a comprehensive description of the interactions between the single spins and their environment is needed.

This Thesis presents the study of magnetism and superconductivity at the atomic scale by means of Low-Temperature Scanning Tunneling Microscopy and Spectroscopy (STM/STS) under ultra-high vacuum conditions.

The detection of the single spins is carried out by the use of STS. Scattering of tunneling electrons with the spins leads to spectral features around zero energy, whose linewidth reveals the interplay of the relevant energy scales present in the system, namely magnetic anisotropy and the Kondo effect.

For the case of transition metal atoms on an insulating layer, we investigated the energy scaling of the different processes and found that they could be tuned by modifying the adsorption site, or by adsorbing hydrogen atoms. The later strongly modified the magnetic behaviour of the atom though the *d*-orbital filling, hence modifying the spin.

Molecular magnets represent an interesting model case of an atomic spin in the presence of a robust magnetic anisotropy induced by the ligand field. We investigated its behavior when placed on a metallic surface, and studied the new interactions arising due to the scattering of electrons by the localized spin. Iron porphyrins present an integer spin distributed along the whole molecule, host by two spin-polarized orbitals hybridized with molecular states. Here we show that the distinct interaction of each orbital with the substrate gives rise to two spin excitation pathways that we could selectively excite by the choice of the tip position within the molecule. The effect of such interactions are further investigated in a bimetallic organic platform, where intramolecular spin-spin interactions are expected.

Superconducting substrates offer a unique platform to investigate sin-

gle spins. Their interaction gives rise to localized bound states inside the superconducting gap, thus exhibiting long lifetimes that enable the study of magnetic phenomena with high energy resolution. In this context, we extended our studies on iron porphyrin molecules on a superconducting lead substrate, and found that the multiorbital character of the integer spin transforms here into a complex multichannel configuration. The molecular systems is found to be partially quenched into a spin $S = 1/2$ due to an underscreened Kondo many-body ground state, where each subgap excitation is associated to a channel with very different coupling with the substrate.

Finally, motivated by the search of new superconducting platforms, we investigate the crystalline two-dimensional NbSe₂ superconductor. The presence of weak disorder prompts the emergence of multifractal eigenstates that govern the local characteristics of the order parameter. In spite of the spatial fluctuations of the superconducting gap, phase coherence holds, and superconductivity manifests in the mesoscopic scale.

The results shown here were obtained in collaboration with the group of Prof. Nicolás Lorente and Prof. Daniel Sánchez-Portal, who performed first-principle Density Functional Theory simulations. The novel molecular platforms used for the study of exchange coupling were synthesized by the group of Prof. Pei Nian Liu in collaboration with the group of Prof. Nian Lin. The analytic model that predicts the spatial variations of the superconducting gap governed by multifractal eigenstates was developed by Prof. Antonio M. García-García.

Resumen

El entendimiento de las escalas energéticas que gobiernan el magnetismo en un solo átomo proporciona la información definitiva hacia su aplicación en nuevas tecnologías, como espintrónica orgánica. Su materialización depende de que la interacción entre la corriente de electrones y los espines sea eficiente. Por lo tanto, es necesario abordar el tema desde un punto de vista fundamental, proporcionando una descripción completa de las interacciones entre los espines individuales y su entorno.

Esta Tesis estudia los fenómenos de magnetismo y superconducibilidad a escala atómica por medio de Microscopía y Espectroscopía de Efecto Túnel a bajas temperaturas (STM/STS) en condiciones de ultra-alto vacío.

La detección de los espines se realiza a través de STS. La dispersión de los electrones túnel con los espines genera la aparición de rasgos distintivos espectroscópicos a energía cero, cuyos detalles vienen determinados por las escalas de energía relevantes para el sistema, que son anisotropía magnética y el efecto Kondo.

Para el caso de un átomo de metal de transición en una capa aislante, investigamos cómo escalan los diferentes procesos presentes, y concluimos que pueden manipularse modificando el lugar de adsorción o enlazando átomos de hidrógeno. Esta última aproximación modificó fuertemente el comportamiento magnético del átomo a través del llenado de los orbitales *d*, modificando por tanto su espín.

Los imanes moleculares son un supuesto muy interesante de un espín protegido por una anisotropía magnética alta inducida por el campo cristalino. Su comportamiento fue investigado al depositarse en un sustrato metálico, y estudiamos las nuevas interacciones que aparecen debido a la dispersión de los electrones con el espín localizado. Las porfirinas de hierro tienen un espín entero que se distribuye a lo largo de toda la molécula en dos orbitales polarizados en espín hibridado con estados moleculares. En esta Tesis mostramos que la diferente interacción de cada orbital con el sustrato da lugar a dos caminos de excitación de espín que pueden ser seleccionadas con la posición de la punta en la molécula. El efecto de estas interacciones se investiga en mayor profundidad en una plataforma orgánica bimetálica,

en la que se esperan interacciones espín-espín intramoleculares.

Los sustratos superconductores son una plataforma única para investigar espines individuales. Su interacción da lugar a estados ligados espacialmente localizados y energéticamente situados dentro del gap superconductor, que exhiben tiempos de vida largos, lo cual permite el estudio de los fenómenos magnéticos con gran resolución energética. En este contexto, extendimos nuestros estudios de porfirinas de hierro a un sustrato superconductor, y encontramos que el carácter multiorbital del espín entero se transforma en este caso en una configuración multicanal compleja. El sistema molecular se encuentra parcialmente apantallado, dando lugar a un espín $S = 1/2$ debido a un estado fundamental de many-body underscreened Kondo, donde cada estado intra-gap se asocia con un canal que se acopla de manera distinta al sustrato.

Finalmente, motivados por la búsqueda de nuevas plataformas superconductoras, investigamos el superconductor cristalino bidimensional NbSe₂. La presencia de desorden débil favorece la aparición de estados multifractales que gobiernan las características locales del parámetro de orden. A pesar de las fluctuaciones espaciales del gap superconductor, la coherencia de fase se mantiene, y el estado superconductor se manifiesta en la escala mesoscópica.

Estos resultados han sido obtenidos en colaboración con el grupo del Prof. Nicolás Lorente y del Prof. Daniel Sánchez-Portal, que realizaron simulaciones *ab initio* de Teoría del Funcional de Denstidad (DFT). Las nuevas plataformas moleculares utilizadas para el estudio de acople magnético fueron sintetizadas en el grupo del Prof. Pei Nian Liu en colaboración con el grupo del Prof. Nian Lin. El modelo analítico que predice las variaciones espaciales del gap superconductor, gobernadas por estados multifractales, ha sido desarrollado por el Prof. Antonio M. García-García.

Contents

Introduction	1
1 Experimental Methods	5
1.1 Scanning Tunneling Microscopy	5
1.2 Scanning Tunneling Spectroscopy	7
1.3 Inelastic Electron Tunneling Spectroscopy	8
1.4 Experimental set-up	9
I Atomic-scale magnetism	11
2 Magnetism at the atomic scale	13
2.1 Single-impurity Anderson model	13
2.2 The Kondo effect and its spectral properties	15
2.3 Magnetocrystalline Anisotropy	17
2.4 Outline of Part I	17
3 Control of magnetic anisotropy of single magnetic atoms on an insulating layer	19
3.1 Magnetic ground state of chromium adatoms on two adsorption sites	20
3.2 Tuning the magnetic anisotropy by hydrogenation of transition metal atoms	23
3.3 Iron adatoms as a prototypical highly anisotropic system . . .	26
3.4 Conclusions	27
4 Orbital-selective spin excitations in a magnetic porphyrin	29
4.1 Surface adsorption and spin excitations on FeTPP	30
4.2 Higher order scattering processes	33
4.3 Frontier orbitals of FeTPP	36
4.4 Conclusions	39

5 Surface-induced quench of intramolecular exchange coupling in bimetallic porphyrin complexes	41
5.1 Three molecular structures	42
5.2 Spectroscopic fingerprints of 2-FeDPP	44
5.2.1 Vanishing of exchange coupling upon surface adsorption	45
5.3 Interpretation of the magnetic ground state of each independent Fe ion	47
5.3.1 Entering the mixed-valence regime	48
5.4 Conclusions	50
 II Local distortions of Superconductivity	 51
6 Effects of magnetic impurities and weak disorder on superconductivity	53
6.1 Superconductivity in the STM	55
6.2 Deviations from the clean limit: magnetic impurities and weak disorder	57
6.2.1 Magnetic impurities as point scatterers	57
6.2.2 Two-dimensional superconductivity in the presence of weak disorder	59
6.3 Outline of Part II	61
 7 Multiple Shiba bound states in the underscreened Kondo regime	 63
7.1 The Moiré molecular superstructure	63
7.1.1 Dark and bright FeTPP: two states of the same molecule	65
7.1.2 Tuning the magnetic anisotropy in dark FeTPP molecules	76
7.2 Conclusions	79
 8 Multifractal superconductivity in single-layer NbSe₂	 81
8.1 Spatial inhomogeneities of the superconducting gap	82
8.2 Statistical analysis of the SC gap width	86
8.3 Theoretical modelling of the probability distribution of the superconducting gap	87
8.4 Conclusions	89
 Appendix	 91
 9 Conclusions and Outlook	 99
 References	 112

Publications	i
Resumen Extendido	iii

Introduction

Magnetism is a collective phenomenon. Ferromagnetism emerges due to two quantum-mechanical effects: spin and exchange. Materials whose atoms have unpaired electrons in their *d*-orbitals present an associated spin, which can align parallel or antiparallel to the neighbouring atoms as a result of the exchange interaction. However, if we reduce the size of the system down to the single-atom limit, we find that even in the presence of unpaired electrons, there is no preferential direction for them to align: atoms are isotropic. And here is where magnetocrystalline anisotropy plays an important role, breaking the degeneracy of the three spatial dimensions and conferring a preferential direction for the spin. When we measure the magnetic anisotropy energy of a system, we are measuring the stability of such magnetization.

Magnetic stability is crucial in the field of magnetic memories, which storage information by the pattern of magnetic materials. As the size of the material is reduced from macroscopic dimensions, its capability to stay magnetized is reduced until the superparamagnetic limit is reached and the average magnetization is zero, which sets a limit on the storage density of hard disk drives. Therefore, the industry demands for new approaches towards the stabilization of magnets in the nm-scale, which involve the fundamental understanding of the single-atom spins. One approach towards the stabilization of an atomic magnetic moment is to embed it in an organic molecule.

Molecular magnetism is a field that comprises the great efforts done since the 1970s to obtain organic ferromagnetic materials. The original idea was to use the metallic properties of the organics to induce such mesoscopic magnetic order, which has been shown to be extremely difficult at room temperature [?]. Nevertheless, such approach initiated a whole research field that focuses on the understanding of each magnetic entity, paving the way to emerging technologies such organic spintronics [1–6].

The access to the magnetic properties of such molecular magnets has been accomplished mainly by the use of SQUID magnetometry [?] or by X-ray radiation, namely X-ray photoelectron spectroscopy (XPS), X-ray ad-

sorption spectroscopy (XAS) and X-ray magnetic circular dichroism (XMCD) [?]. However, in spite of the rich information that these techniques provide about the bulk magnetism, the behavior of the single units is hidden by the spatial averaging nature of such measurements.

The development of the Scanning Tunneling Microscope (STM) in 1981 provided access to surfaces at the atomic level [?, ?]. By the use of the STM tip as a local probe, we can interrogate single atoms and molecules, and spatially resolve their electronic and magnetic properties.

The STM gives access to individual magnetic moments through Scanning Tunneling Spectroscopy (STS). The magnetic moment defines the atomic spin S , which governs the spectral properties of single atoms and molecules. Careful choice of the platform to accommodate such individual spins may offer distinct pieces of information. Metallic substrates generally tend to hybridize the magnetic impurities with their electron Fermi sea and introduce scattering processes resulting in the Kondo effect [7], thus providing information about the coupling of the impurity's spin to the substrate. Insulating surfaces, however, decouple the magnetic moment from the electron bath, and unveil the preferential orientation of the atomic spin.

One of the major tasks of this PhD Thesis was the detection of the excitation of such spins [8], as well as unraveling the effect of variations in the transition metal atom d -orbital occupation and on the environment. Furthermore, we introduce local variations to manipulate the atom's magnetic ground state, either through the impurity's adsorption site, the bonding of a volatile molecule to the impurity or by embedding it into an organic core.

A step further into the understanding of individual spins is to study their effect on a superconducting substrate. When a dilute amount of magnetic impurities is placed on top of a superconductor, they create a potential that locally distorts the Cooper pairs bath, while the mesoscopic superconducting characteristics remain unaltered [?]. The coupling of the impurity to the substrate create Yu-Shiba-Rusinov bound states [9–11], which can be studied down to the μeV energy range in STS measurements performed with superconducting STM tips [?, 12, 13]. Therefore, we can resolve, energetically and spatially, each of the coupling channels between the magnetic impurity and the superconductor underneath.

In the search of new superconducting materials, we find Transition Metal Dichalcogenides as a new platform of crystalline layered materials that can be isolated down to the single-layer limit. In this regard, single-layer NbSe₂ is envisioned as an ideal system for the study of superconductivity in two dimensions, as an exotic arena for the study of the effect of magnetic impurities.

Outline

The contents of this Thesis are organized as follows:

Section 1 introduces the experimental methods, namely Low-Tempertaure Scanning Tunneling Microscopy and Spectroscopy.

Part I is devoted to the study of magnetism at the atomic scale.

Section 2 reviews the problem of a single-magnetic impurity in terms of the Anderson model, and relates it with the relevant energy scales that play a role in such systems.

Section 3 shows the coexistence of magnetic anisotropy and the Kondo effect in single magnetic atoms placed on an insulating layer.

Section 4 focuses on the orbital-selective excitation of a molecular spin due to the distinct hybridization of each channel with the substrate.

Section 5 reports the spin excitation on a multi-center molecular platform, where the presence of a metallic surface presumably quenches the intramolecular exchange coupling.

Part II focuses on the local distortions of superconductivity.

Section 6 serves as a review of the basic concepts of superconductivity and how magnetic impurities and weak disorder affect the many-body condensate.

Section 7 shows the emergence of multiple in-gap excitations due to the coupling of a magnetic molecule with a superconducting substrate in the underscreened Kondo regime.

Section 8 highlights the emergence of the multifractal regime in a weak-disordered two-dimensional superconductor.

Section 9 Summarizes the results of this Thesis and gives an outlook and perspectives for the future.

Chapter 1

Experimental Methods

This Thesis explores the limits of magnetism and superconductivity at the atomic scale with the use of a single technique: Scanning Tunneling Microscopy. The study of single atoms and single molecules is carried out under ultra-high-vacuum conditions to ensure the cleanliness of the sample surface. Furthermore, low temperatures are used to stabilize the single units and to study their electronic properties beyond the thermal limit through Scanning Tunneling Spectroscopy.

1.1 Scanning Tunneling Microscopy

The working principle

In 1986 the Nobel Prize in Physics was awarded to Gerd Binnig and Heinrich Rohrer for the design of the Scanning Tunneling Microscopy (STM), four years after their invention [?, ?, ?]. The Tunneling Effect, a quantum-mechanical process that allow particles to cross potential barriers that classically could not overcome, is the working principle of the STM. A metallic tip is placed at a few Angstroms distance of a surface and, through the application of a DC bias voltage between them, a tunneling current I_t flows through the vacuum barrier. The exponential decay of the tunneling current with the tip-sample distance allows the control of the tip height with picometer sensitivity. Once the tip-sample distance is defined with the feedback parameters (namely tunneling current and bias voltage), the STM can scan the surface in the XY directions recording the tip height (constant-current mode) or the tunneling current (constant-height mode). As a result, a topographic map of the surface area is obtained.

Quantum mechanics: description of the tunneling current

Electrons have a finite probability to tunnel from tip to sample [?]:

$$|\psi(z)|^2 = |\psi(0)|^2 e^{-2\kappa z} \quad , \quad \kappa = \sqrt{\frac{m_e}{\hbar^2}(\Phi_t + \Phi_s - eV)} \quad (1.1)$$

where $\psi(0)$ and $\psi(z)$ represent the electron wavefunction at positions 0 and z . κ represents the decay rate of the wavefunction inside the tunneling barrier, m_e is the electron mass, \hbar is the reduced Planck constant and Φ_t and Φ_s are the tip and metal workfunctions, respectively.

Bardeen [?] developed a formalism that described independently the wavefunction of tip and sample as ψ_ν and ψ_μ , respectively. Therefore, the tunneling current is described as

$$I = \frac{2\pi e}{\hbar} \sum_{\mu,\nu} \{ f_t(E_\nu - eV) [1 - f_s(E_\mu)] - [1 - f_t(E_\nu - eV)] f_s(E_\mu) \} \times |M_{\mu\nu}|^2 \delta(E_\mu - E_\nu) \quad (1.2)$$

where $f(E)$ is the Fermi distribution function, E_μ and E_ν are the energies of the states ψ_μ and ψ_ν . The δ function ensures energy conservation, and thus only elastic tunneling processes are taken into account. $M_{\mu\nu}$ is the transition matrix element between states ψ_μ and ψ_ν , given by [?]:

$$M_{\mu\nu} = -\frac{\hbar^2}{2m_e} \int_S d\mathbf{S} (\psi_\mu^* \nabla \psi_\nu - \psi_\nu \nabla \psi_\mu^*) \quad (1.3)$$

Substituting the summation of discrete states by the integral over the energy range through the density of states of tip ρ_t and sample ρ_s [?]:

$$I = \frac{2\pi e}{\hbar} \int_{-\infty}^{\infty} \rho_t(E - eV) \rho_s(E) [f_t(E - eV) - f_s(E)] \times |M(E)|^2 dE \quad (1.4)$$

Approximating the Fermi-Dirac distributions with a step functions ($T=0$) leads to

$$I = \frac{2\pi e}{\hbar} \int_{E_F}^{E_F + eV} \rho_t(E - eV) \rho_s(E) |M(E)|^2 dE \quad (1.5)$$

The Tersoff-Hamann approximation estimates the tunneling current to be provided by the last atom in the tip apex. Furthermore, considering the voltage range to be very small around the Fermi level, the tunneling current expression simplifies to

$$I = \frac{32\pi^3 e^2 \Phi^2 R^2 V}{\hbar \kappa^4} e^{2\kappa R} \rho_t(E_F) \rho_s(\mathbf{r}_0, E_F) \quad (1.6)$$

where R is the curvature radius of the tip and \mathbf{r}_0 is the position of the center of curvature of the tip. Therefore, for small biases the tunneling current is linearly dependent on the bias and the density of states of tip and sample.

1.2 Scanning Tunneling Spectroscopy

The linear dependence of the tunneling current with the density of states confers the STM the capability of probing the electronic structure of the system under study.

The tunneling current can also be described in terms of the tunneling transmission dependence of the tip-sample distance $T(z, E, eV)$ [?, ?]

$$I(V) \propto \int_{E_F}^{E_F + eV} \rho_t(E - eV) \rho_s(E) T(z, E, eV) dE \quad (1.7)$$

Since the tunneling transmission depends not only on the tip-sample distance and on the energy but also on the applied bias voltage, differentiation of equation 1.7 with respect to the bias voltage leads to

$$\begin{aligned} \frac{dI}{dV} &\propto \rho_t(E_F) \rho_s(E_F + eV) T(z, E_F + eV, eV) + \\ &+ \rho_t(E_F - eV) \rho_s(E_F) T(z, E_F, eV) + \\ &+ \int_{E_F}^{E_F + eV} \rho_t(E - eV) \rho_s(E) \frac{dT(z, E, eV)}{dV} dE + \\ &+ \int_{E_F}^{E_F + eV} \rho_s(E) \frac{d\rho_t(E - eV)}{dV} T(z, E, eV) dE \end{aligned} \quad (1.8)$$

Assuming constant transmission coefficient and ρ_t ,

$$\frac{dI}{dV} \propto \rho_t(E_F)\rho_s(E_F+eV)T(z, E_F+eV, eV) + \rho_t(E_F-eV)\rho_s(E_F)T(z, E_F, eV) \quad (1.9)$$

The first term in eq. 1.9 dominates at $V > 0$ and the second term at $V < 0$. Therefore, measuring dI/dV gives access to the density of states of the sample at a give energy eV .

Experimental obtention of the dI/dV

The dI/dV signal is obtained with a lock-in amplifier. In this technique, a small AC voltage is added to the DC bias voltage. As a consequence, the modulated tunneling current is sensitive to the slope of the $I - V$ characteristics around the selected DC bias value, and can be expanded in a Taylor series

$$I(V + V_{mod} \sin(\omega t)) \sim I(V) + \frac{dI(V)}{dV} V_{mod} \sin(\omega t) + \frac{1}{2} \frac{d^2 I(V)}{dV^2} V_{mod}^2 \sin^2(\omega t) + \dots \quad (1.10)$$

We can obtain a magnitude proportional to the differential conductance dI/dV by measuring the amplitude of the first harmonic frequency. In the same way, the second harmonic is proportional to the second derivative of the current $d^2 I/dV^2$, which is very sensitive to small changes in the dI/dV signal. This signal is typically employed to enhance the weak inelastic signal in vibrational spectroscopy over the dominating elastic components. In this Thesis we employ it to enhance small changes of spin-excitation inelastic signal with magnetic field, as we show in Section 4.

1.3 Inelastic Electron Tunneling Spectroscopy

A significant part of this Thesis focuses on atomic-scale magnetism. In order to access the spin of a single atom, we make use of the capability of tunneling electrons to transfer energy and angular momentum through the scattering with such magnetic impurities, and open an additional tunneling channel: the inelastic channel [?, ?, ?, ?, ?, 14].

A magnetic impurity possess discrete energy levels that can be probed with the STM tip. By sweeping the bias voltage at a constant tip height, the tunnelling current increases at a constant rate due to the elastic tunnel of electrons. However, when the applied bias voltage matches the energy difference between the ground state and the first excited state, electrons can make such excitation by inelastic tunneling. Therefore, two paths, elastic and inelastic, contribute to the increase in the tunneling current. The

increase in the I - V slope results in a step in the dI/dV - V curve at the threshold energy of the excitation. While the elastic channel connects initial and final state coherently, the inelastic channel involves a transition. Such transition can be described by intermediate virtual states and, as we will show in Section 4, their nature define the details in the lineshape of the inelastic spin excitations.

1.4 Experimental set-up

All the experimental results included in the present Thesis were obtained in a commercial low-temperature STM with a base temperature of 1.2 K under ultra-high-vacuum (UHV) conditions developed by SPECS GmbH. Such low base temperature is reached by a Joule-Thomson cycle. A close circuit continuously flows helium gas into a small pot placed on top of the STM head, which is pumped with a scroll pump. The expansion of the helium gas reduces the temperature from 4.2 K to 1.2 K. The STM head can perform in both scanning tunneling and atomic force modes, and has a X-Y sample course motion and exchangeable STM/AFM tips. A vacuum magnet placed around the STM head can apply up to $B = 3$ T out-of-plane magnetic field. In order to enhance the energy resolution of the STS measurements, we included an LC filter in the bias just before the STM head and a π -filters in the high-voltage piezo connector.



Figure 1.1: Picture of the SPECS UHV-LT-STM system used during this Thesis.

The whole system consists on three independent UHV chambers as

shown in Fig. 1.1. The preparation chamber is equipped with a sputter ion-gun, a sample heating-stage and a mass spectrometer. The molecular-beam-epitaxy (MBE) chamber includes a home-made Knudsen cell evaporator and a commercial four-pocket evaporator developed by Dodecon. The STM chamber contains a metal evaporator used to evaporate metals directly on the cold surface inside the STM. The STM head hangs from springs in order to filter-out high-frequency vibrations, and is isolated from low-frequency mechanical vibrations with pneumatic feet that lift the whole system. We used an external AMETEK 7270 DSP lock-in amplifier. Analysis of STM and STS data was performed with the WSxM [15] and SpectraFox [16] software packages.

The monocrystals used in this Thesis (namely, Cu(100), Au(111) and Pb(111)) were cleaned under UHV conditions by several cycles of Ar sputtering and subsequent annealing. Pb(111) was also grown *in situ* on top of graphene/SiC in the MBE chamber. The single-layer NbSe₂ samples were grown at Lawrence Berkeley National Laboratory (LBNL) and Stanford University and capped with selenium. We removed the capping layer under UHV conditions by annealing to $\sim 300^\circ \text{ C}$ and subsequently transferred it to the STM. The iron porphyrin molecules used in this Thesis are commercially available at Sigma Aldrich. They were sublimated from a commercial Dodecon evaporator at $\sim 350^\circ \text{ C}$.

Part I

Atomic-scale magnetism

Chapter 2

Magnetism at the atomic scale

A magnetic impurity placed on a surface experiences the effect of the hybridization with the host electron bath. In this Section we will revise the problem of a single-magnetic impurity with regard to the Anderson model, that introduces the terms of exchange and charge scattering, necessary for the understanding of the Kondo effect. Furthermore, we will show that the asymmetric environment imposed by the surface lifts the degeneracy of the impurity d -orbitals through the crystal field, which in the presence of strong spin-orbit coupling interactions, gives rise to magnetocrystalline anisotropy.

2.1 Single-impurity Anderson model

In 1961 Philip Warren Anderson described the interaction of a half-filled d -atomic orbital with the electronic continuum of a host metal substrate assuming a band structure with s -character [17]. Anderson modeled such localized magnetic state with the Hamiltonian

$$H = H_{0f} + H_{0d} + H_{sd} + H_{corr} \quad (2.1)$$

where H_{0f} is the unperturbed energy of the free-electron system, H_{0d} is the unperturbed energy of the d state, H_{sd} is the interaction among s and d levels and H_{corr} accounts for the Coulomb repulsion between two electrons at the d orbital:

$$H_{0f} = \sum_{k,\sigma} \epsilon_k c_{k\sigma}^\dagger c_{k\sigma} \quad (2.2)$$

$$H_{0d} = \sum_{\sigma} \epsilon_d c_{d\sigma}^\dagger c_{d\sigma} \quad (2.3)$$

$$H_{sd} = \sum_{k,\sigma} V_{dk} (c_{k\sigma}^\dagger c_{d\sigma} + c_{d\sigma}^\dagger c_{k\sigma}) \quad (2.4)$$

$$H_{corr} = U_d n_{d\uparrow} n_{d\downarrow} \quad (2.5)$$

where ϵ_k is the energy of the free-electron state of momentum k , ϵ_d is the energy of the half-filled atomic orbital with respect to the Fermi level, V_{dk} is the interaction potential between an electron in the host with wave vector k and the localized d level, and $c_{k\sigma}$ and $c_{k\sigma}^\dagger$ are the destruction and creation operators for conduction electrons, and $c_{d\sigma}$ and $c_{d\sigma}^\dagger$ for the localized impurity. The term U_d represents the Coulomb repulsion energy of the d state, and n is the number operator $n_{d\uparrow} = c_{d\uparrow}^\dagger c_{d\uparrow}$.

The single-impurity Anderson model thus describes a singly-occupied state located at an energy position ϵ_d , whose unoccupied counterpart is at $\epsilon_d + U_d$, as sketched in Fig. 2.1a (note that $\epsilon_d < 0$). In order to relate such high-energy excitations of the many-body Hamiltonian with an effective low-energy model, Schrieffer and Wolff [18] formulated a transformation that provides a microscopic description of the system in terms of the single-impurity Anderson model and the Kondo Hamiltonian.

Such energy level is subject to hybridization with the Fermi sea of the host, which introduce scattering processes with the impurity state. We distinguish between two scattering amplitudes: exchange scattering J and potential scattering \mathcal{U} . Exchange scattering mechanisms can flip the spin of the impurity, while the potential term only introduces charge scattering. In the absence of potential scattering $\mathcal{U} = 0$, the system is found in the particle-hole symmetry point ($2|\epsilon_d| = U_d$). The Schrieffer-Wolff transformation [18] provides the expressions for both scattering amplitudes [19]:

$$J = \frac{2}{\pi} \Gamma^2 \left(\frac{1}{\epsilon_d} - \frac{1}{\epsilon_d + U_d} \right) \quad (2.6)$$

$$\mathcal{U} = \frac{2}{\pi} \Gamma^2 \left(\frac{1}{\epsilon_d} + \frac{1}{\epsilon_d + U_d} \right) \quad (2.7)$$

where $\Gamma \propto |V_{dk}|^2$ [18] is the broadening of the occupied state due to hybridization with the substrate, J the spin-spin exchange scattering and \mathcal{U} the potential scattering amplitude. While J is always negative, \mathcal{U} can take either sign. As we will show in the next Section, such exchange J term represents Kondo scattering events.

2.2 The Kondo effect and its spectral properties

In 1936, W. J. de Haas and G. J. van den Berg [?] measured the evolution of the resistance of metallic wires at low temperatures. They observed that the resistance reached a minimum at a certain temperature and increased upon further reduction of the temperature, and studied the influence of the purity of the metal. According to their results, the unexpected increase of the resistance at low temperatures was not related to the vibrations of the lattice.

In 1968, Jun Kondo proposed that the increase of resistance at low temperatures was caused by the presence of magnetic impurities in the wires [7]. Kondo investigated the exchange scattering of conduction electrons by magnetic impurities and found a logarithmic dependence of the resistance with the temperature that explained earlier experiments on metallic wires.

A phenomenological description conceives a magnetic impurity coupled to the Fermi sea of the metallic host with a strength J . If the coupling to the substrate is strong enough, spin-flip scattering is very efficient and result in the screening of the magnetic impurity by the conduction electrons, which tend to align antiferromagnetically, driving the system towards a non-magnetic ground state: the many-body Kondo singlet. Since the dominant contribution to the electrical resistance in metals arises from the scattering of the conduction electrons, such scattering with the magnetic impurity will additionally increase the resistance.

Some years later, in 1988, it was predicted [?, ?] that the Kondo effect could also be observed in quantum dots with odd occupation, and indeed several transport experiments [?, ?, ?, ?, ?, ?] found evidence for the predicted zero-voltage resonance. In terms of the single-impurity Anderson model, the impurity density of states in the Kondo regime is characterized by a narrow, logarithmic zero-energy resonance, whose width is determined by the coupling to the electron bath. Additionally, singly-occupied and unoccupied d -level states appear at ϵ_d and $\epsilon_d + U$, respectively as shown in Fig. 2.1a (please note that $\epsilon_d < 0$).

The emergence of such state at zero energy can be understood in terms of the virtual spin-flip processes shown in Fig. 2.1b-e. In order to rationalize the Kondo effect in the STM configuration, we sketch a magnetic impurity with spin down coupled to a metallic substrate (left) in the presence of a metallic STM tip (right). At the initial state, the singly-occupied d -level hosts a single electron with spin down (2.1b). Due to the finite exchange coupling J to the metallic host, there is certain probability for the processes depicted in Fig. 2.1c-d to take place: the spin-down electron may hop off the impurity (2.1c) or a substrate electron can tunnel into the impurity (2.1d). Therefore, once the system relaxes back, there is no preferential

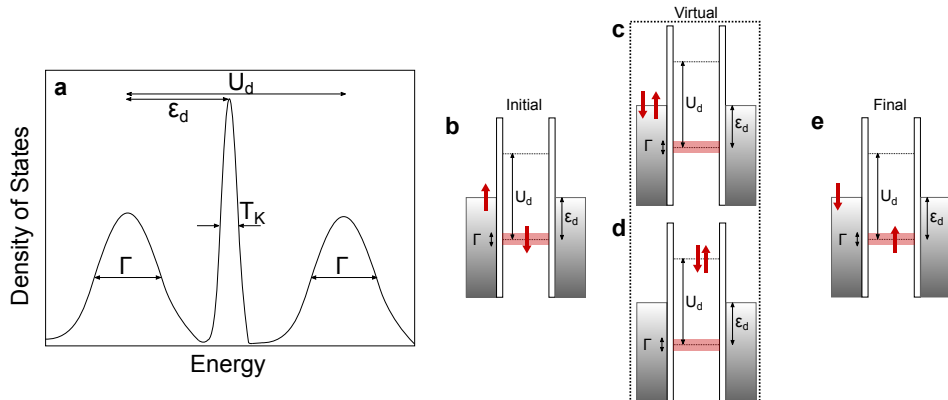


Figure 2.1: a, Sketch of the Density of States of the Anderson single-impurity model in the Kondo Regime. Both axis show arbitrary units but the energy would be in the eV range. The broadening due to the hybridization of the occupied orbital with the substrate is represented by Γ . The width of the Kondo resonance is T_K . b-e, Schematic energy diagram of an energy level ϵ_d occupied by a single electron. The initial (b), virtual (c,d) and final (e) states depict the spin-flip process of the magnetic impurity by a host electron of opposite spin via two possible virtual processes, giving rise to the Kondo effect.

direction for the spin in the impurity final state. The underlying principle for Kondo resonance emerging at the Fermi level is the quantum interference of both virtual processes in 2.1c,d. Since the spin-flip processes are virtual, they occur at zero energy, and therefore the renormalized density of states exhibits a zero-voltage peak.

In most atomic and molecular systems the magnetic moment is hosted by several occupied atomic orbitals. In this case, the Hund's intra-atomic energy scale partially hinders spin-flip interactions of an individual orbital hybridized with the metallic host. The spectral properties of the Kondo effect vary depending on the number of spins and the number of channels connecting the atomic impurity with the substrate.

A different scenario emerges when in addition to Hund's energy, an additional energy scale is introduced in the system by asymmetries in the crystal field around the magnetic atom. Different overlap of the atomic orbitals with the environment breaks the degeneracy of the d -shell, and the spin is bound to lie in a set of well defined spin-polarized orbitals. In the presence of spin-orbit coupling, the spin orientation is locked to the orientation of the angular momentum of the spin hosting orbital, resulting in a net preference of the spin alignment along certain spatial directions: the

magnetocrystalline anisotropy.

2.3 Magnetocrystalline Anisotropy

A quantum spin $S > 1/2$ possesses a multiplet of all the $2S + 1$ possible states. Such multiplet is degenerate for a free atom. However, in the presence of crystal field and spin-orbit coupling, they split following the spin Hamiltonian [20]

$$\hat{H}_{CF} = D_{xx}S_x^2 + D_{yy}S_y^2 + D_{zz}S_z^2 = DS_z^2 + E(S_x^2 + S_y^2) \quad (2.8)$$

$$(2.9)$$

where $\mathbf{S} = S_x, S_y, S_z$ is the spin operator, and $D = D_{zz} - \frac{1}{2}D_{xx} - \frac{1}{2}D_{yy}$ and $E = \frac{1}{2}(D_{xx} - D_{yy})$. The spin Hamiltonian assumes that the orbital moment of the impurity is quenched, as it usually occurs in magnetic impurities on surfaces, and that it can be treated as a perturbation.

One can see that $D = 0$ when $D_{xx} = D_{yy} = D_{zz}$, i. e. in cubic symmetry. In axial symmetry, $D_{xx} = D_{yy}$, and therefore $E = 0$. We can express the energies of the multiplet $2S + 1$ with just two parameters: D and E . By convention, z is defined to maximize $|D|$ and to have $E > 0$. While D splits energy levels of different $|S_z|$ components, E mixes them in the meV energy range. In the following, we will refer to them as axial and transverse anisotropy parameters, respectively.

2.4 Outline of Part I

In the following we will show how the two effects presented above, the Kondo effect and magnetocrystalline anisotropy, coexist in single atoms and molecules. We will show in Section 3 that chromium and iron adatoms present distinct magnetic ground state determined by their d -orbital filling and hybridization with the insulating substrate. Furthermore, we will present the manipulation of their magnetic properties by the local adsorption of a single hydrogen molecule.

As discussed above, the Schrieffer-Wolff transformation [18] showed that a magnetic impurity interacts with a metallic host through exchange Kondo (J) and potential scattering (\mathcal{U}) terms. In Section 4 we show the effect that both interactions have in a magnetic porphyrin molecule, and how their strength and sign determine the spectroscopic lineshape exhibited by iron porphyrins.

Finally, we will interrogate the effect of a second magnetic impurity in the study of atomic-scale magnetism. In Section 5 we show a molecular

magnet hosting two iron atoms that, in absence of further interactions, are magnetically coupled. We observed that, upon surface adsorption, such exchange coupling is suppressed and that the organic backbone determines the magnetic properties of each individual iron atom.

Chapter 3

Control of magnetic anisotropy of single magnetic atoms on an insulating layer

The ultimate frontier of magnetism relies on the single-atom limit. Unpaired electrons in the orbitals of a free atom provide a finite spin, but the isotropic environment of a free-atom prevents the emergence of magnetism. A surface that accommodates such adatom imposes a preferential direction for the spin through the so-called magnetocrystalline anisotropy [20], and therefore the adatom exhibits a net magnetic moment. In addition, the coupling to the electron bath of the substrate introduces scattering events could give rise to the screening of the magnetic moment due to the Kondo effect [7,21,22].

The local control of two competing energy scales - magnetic anisotropy and the Kondo effect - would then lead to the design of single-atom magnets, whose magnetic moment is determined by the *d*-shell occupancy of the atom, the crystal field splitting and the coupling to the surface [?]. Tuning the crystal field through the adsorption configuration and the chemical environment are thus fundamental approaches towards the understanding of magnetically stable atomic spins.

In this Section we explore the manipulation of the magnetic ground state of metal atoms on an insulating Cu₂N/Cu(100) surface. We show the control of both spin and magnetic anisotropy by the adsorption of a hydrogen molecule in Cr and Fe adatoms, which leads to opposite trends for CrH₂ and FeH₂ species as reproduced by Density Functional Theory (DFT) simulations carried out by Dr. Roberto Robles (ICN2, Barcelona, Spain) and Prof. Nicolás Lorente (CFM and DIPC, San Sebastián, Spain).

3.1 Magnetic ground state of chromium adatoms on two adsorption sites

We used the insulating nature of a single-layer of Cu₂N to decouple the magnetic moment of transition metal atoms from the Fermi sea of the metal underneath. Such decoupling layer of Cu₂N was grown on a Cu(100) crystal by N₂ sputtering and subsequent annealing to $T = 400^\circ\text{C}$. Then, we deposited on top Cr atoms at low temperature ($T < 15 \text{ K}$), as can be seen in Fig. 3.2a. The bright stripes in the STM topograph correspond to the remaining metallic copper due to the incommensurability of the Cu₂N layer with respect to the Cu(100) atomic lattice [23].

We found that Cr adatoms adsorb on top of Cu (75%) or N (25%) surface atoms, as we determined by atomic resolution images (see Fig. 3.2b,c). The Cu adsorption site involves a direct contact with the metallic substrate in addition to a bond to the two neighboring N atoms. However, impurities on the N site experience a more axial environment since they only bond to the surface N atom. The distinct coupling to the substrate that Cr impurities undergo on each adsorption site determines their magnetic moment and spin orientation, as we will show in the following.

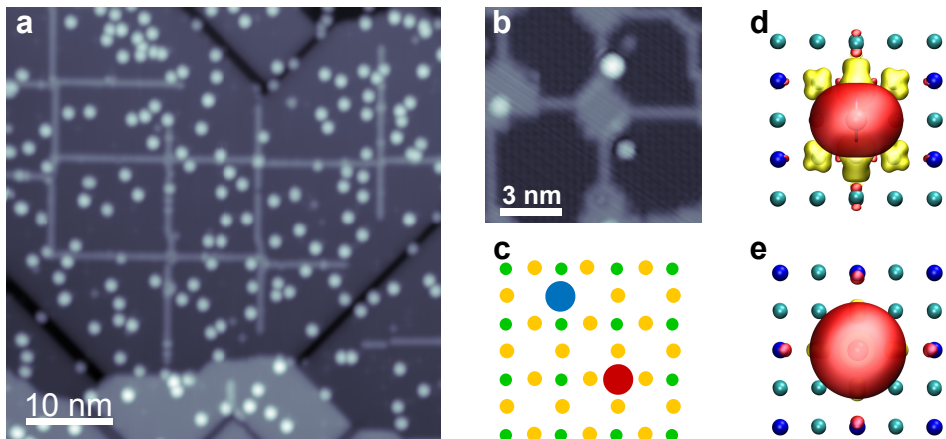


Figure 3.1: a, STM topograph of the Cu₂N surface with Cr atoms deposited on top ($V_S = 1 \text{ V}$, $I = 50 \text{ pA}$). b, Atomic resolution of the Cu₂N surface showing Cr adatoms on Cu (up) and N (down) sites ($V_S = 100 \text{ mV}$, $I = 100 \text{ pA}$). c, Sketch of the Cu₂N surface (top view) representing Cu (yellow) and N (green) sites. The Cr adatoms are shown in blue (Cu site) and red (N site). d, e, Spin-polarized isosurface of the Cr adatom on Cu and N sites, respectively, obtained by DFT simulations. Yellow and red represent each of the two spin directions (the isocontour is $0.005 \text{ e}/\text{\AA}^3$).

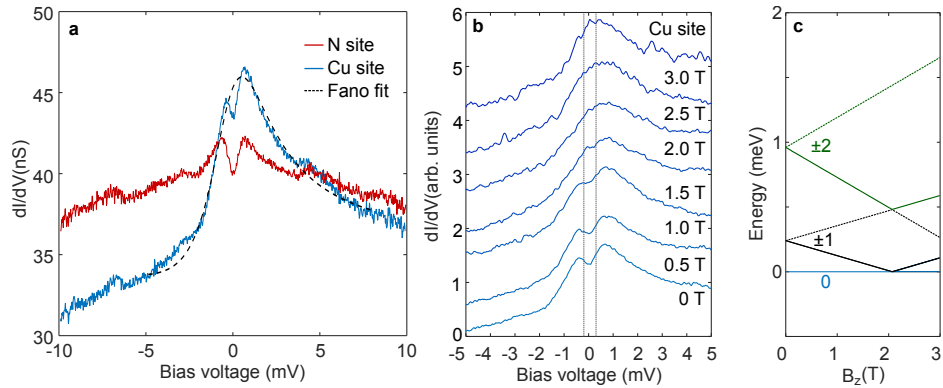


Figure 3.2: **a**, dI/dV spectra of Cr adatoms siting on N (red) and Cu (blue) adsorption sites on the Cu_2N surface. We show the fit to a Fano function in black dashed line that shows a $T_K = 24$ K. **b**, Magnetic field dependence of the spin excitation found on Cr adatoms sitting on the Cu site. ($V_S = 10$ mV, $I = 400$ pA, $V_{rms} = 50$ μ V). **c**, Simulation of the evolution of the spin states with the magnetic field.

Figure 3.2b shows the dI/dV spectra of Cr impurities on top of Cu (blue) and N (red) adsorption sites. We found that both configurations give rise to energy-symmetric steps at $V_S = \pm 0.24$ and ± 0.30 mV for Cu and N sites, respectively. We interpret them in terms of spin excitations [24], where the energy of the inelastic excitation is given by the bias voltage at the step. For the Cu site, we found that the inelastic excitation is enclosed in a wide resonance centered at zero bias, indicative of the Kondo effect. Since the coupling of the magnetic impurity to the electron bath is responsible for the Kondo screening, we can conclude that Cr impurities on the Cu site experience a stronger hybridization with the Fermi sea than those on the N site.

In order to account for the coupling strength, we fit the blue curve in Fig. 3.2b to a Fano function [25] as shown in black dashed line. From the half-width half-maximum of the zero-bias resonance, we extract a Kondo temperature of $T_K \sim 24$ K. DFT simulations found that Cr impurities on the Cu site present a $S = 2$. In terms of the phenomenological spin Hamiltonian [20, p. 15] in eq. 2.8, an excitation at $V_S = \pm 0.24$ meV corresponds to an axial magnetic anisotropy parameter $D = +0.24$ meV. Therefore, $T_K > D$, and then the Kondo effect screens the impurity spin before anisotropy comes into play. Thus, the role of magnetic anisotropy is to prevent complete screening by the electron bath [?]. The two energy scales coexist and give rise to such a lineshape: Kondo scattering events are responsible for the resonance centered at zero bias, and magnetic anisotropy produces a small

yet sizable energy splitting, due to the excitation from the ground state $|m_S = 0\rangle$ to the first excited state $|m_S = \pm 1\rangle$ at $V_S = \pm 0.24$ mV. We found that the inelastic excitation vanishes under the presence of an out-of-plane magnetic field, corroborating its magnetic origin.

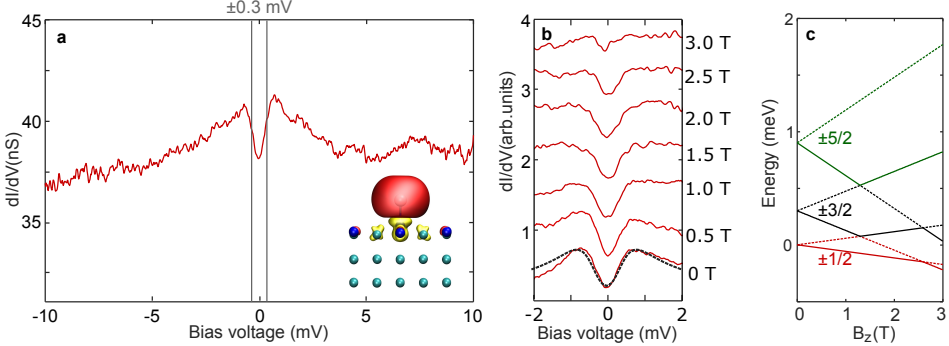


Figure 3.3: **a**, Characteristic dI/dV spectrum of Cr adatoms adsorbed on top of surface N atoms ($V_S = 10$ mV, $I = 400$ pA, $V_{rms} = 50$ μ V). Inset: Spin-polarized isosurface of the Cr adatom obtained by DFT simulations, where yellow and red represent each of the two spin directions (the isocontour is 0.005 $e/\text{\AA}^3$). **b**, Effect of an out-of-plane magnetic field on the spin excitation observed on Cr impurities ($V_S = 10$ mV, $I = 400$ pA). **c**, Simulation of the magnetic field dependency of the S_z spin states of the Cr atom.

Chromium atoms sitting on the N site also show signatures of Kondo scattering events, visible as logarithmic tails above the excitation threshold $V_S = \pm 0.30$ mV (see Fig. 3.3a). The fact that we do not observe a well-developed zero bias resonance indicates a reduced coupling to the electron bath with respect to the Cu site. Under the presence of an external magnetic field, the inelastic excitation vanished at $B \sim 3$ T (see Fig. 3.3b).

In order to unveil the mechanisms that drive the spectral line-shape of the Cr atoms on the N site, we performed DFT simulations that obtained a total spin $S = 5/2$ with an easy-plane configuration. In the inset of Fig. 3.3a we show an isosurface of the electronic density difference between majority and minority spins, which shows a low hybridization with the substrate. We quantified the strength of the magnetocrystalline anisotropy by means of the phenomenological spin Hamiltonian [20], assuming the spin and easy-plane configuration determined by DFT, obtaining an axial magnetic anisotropy parameter $D = 0.15$ meV. Such axial anisotropy splits the ground state $|m_S = \pm 1/2\rangle$ from the first excited state $|m_S = \pm 3/2\rangle$, being this the transition responsible for the observed inelastic excitation.

The response of the spin excitation to an applied magnetic field confirms the assignment of an easy-plane configuration confined to the sample

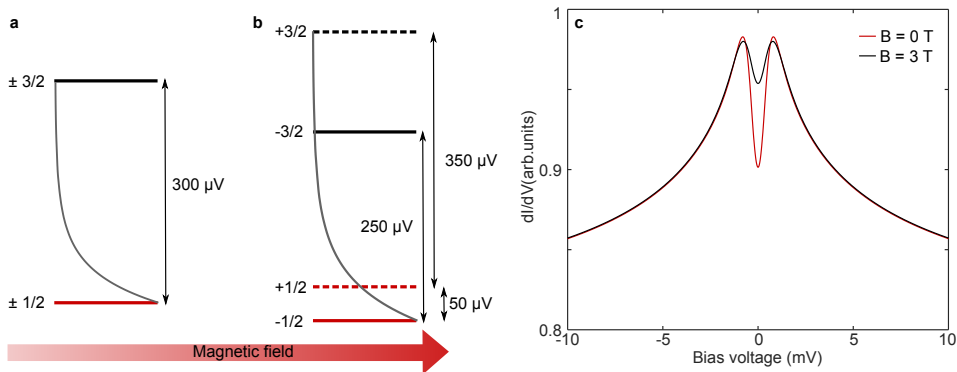


Figure 3.4: a, b, Representation of the ground state $|m_S = \pm 1/2\rangle$ and first excited state $|m_S = \pm 3/2\rangle$ at $B = 0$ T and $B = 3$ T, respectively. The grey line depicts the Boltzmann distribution at $T = 1.2$ K. Simulated [19] dI/dV spectra with the values extracted from the fit in Fig. 3.3.

plane as determined by DFT. We observed that the intensity of the inelastic excitation decreased as the out-of-plane magnetic field was increased, and almost vanished at $B = 3$ T (see Fig. 3.3b). The Zeeman energy splits each $|m_S = \pm 1/2\rangle$ and $|m_S = \pm 3/2\rangle$ doublet, leading to additional excitations as sketched in Fig. 3.4a, b. At zero temperature and $B = 3$ T, two inelastic excitations at $V_S = 50$ μ V and $V_S = 250$ μ V should be observed. However, at $T = 1.2$ K both $|m_S = -1/2\rangle$ and $|m_S = +1/2\rangle$ are populated following a Boltzmann distribution, as shown in Fig. 3.4b. Therefore, a third excitation at $V_S = 350$ μ V is expected at finite temperature. However, the three inelastic excitations are blurred by the limited energy resolution at $T = 1.2$ K, and consequently only a fainter dip is observed at $B = 3$ T as corroborated in the simulated [19] dI/dV spectra in Fig. 3.4c.

3.2 Tuning the magnetic anisotropy by hydrogenation of transition metal atoms

The low magnetic anisotropy found for Cr adatoms on the N site agrees with the half-shell filling of the d -orbitals for a $S = 5/2$. It is comparable to the values reported for Mn ($S = 5/2$) [?] and much smaller than that of Fe ($S = 2$) [8]. In this Section we report that the addition of a hydrogen molecule changes the d -orbital occupation, having dramatic effects on both magnetic ground state and anisotropy.

We exposed the sample to a controlled atmosphere of hydrogen at $T = 1.4$ K. We observed a change in the apparent height of the Cr impurities

by 1/3 after hydrogen adsorption (see Fig. 3.5), and a large enhancement of the inelastic excitation energy (see Fig. 3.5a). The conductance spectrum no longer showed the low-energy spin excitation of Fig. 3.3a but exhibited instead inelastic conductance steps at $V_S = 0.4$ mV, 3.1 mV and 23.0 mV (see Fig. 3.5a). The two lowest excitations resemble the well-known $S = 2$ spectrum of Fe/Cu₂N [8] (see Fig. 3.7 below), suggesting a change in the total spin moment caused by hydrogen adsorption. We observed that the high-energy inelastic excitation decreased its energy value by isotope substitution with deuterium, which implies a vibrational origin.

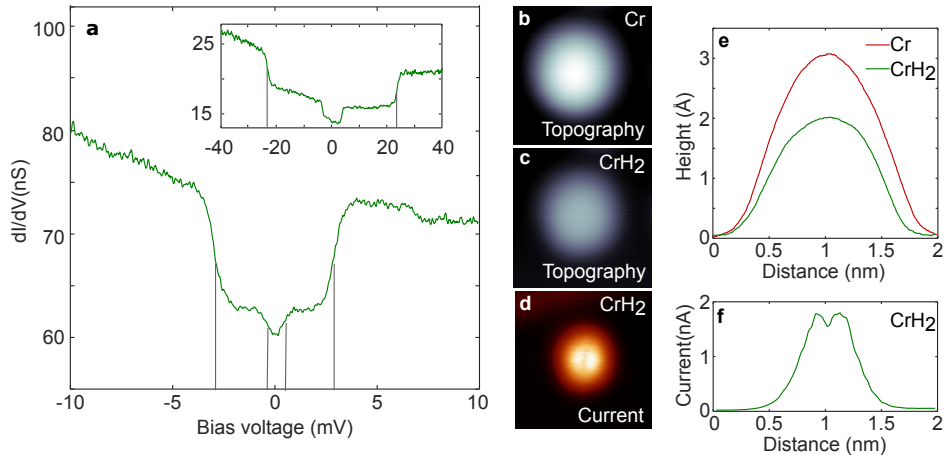


Figure 3.5: a, dI/dV spectra of CrH₂ showing three inelastic steps at ± 0.4 , 3.1 and 23.0 mV ($V_S = 10$ mV, $I=1$ nA). A zoom out of the ± 40 mV energy range is shown in the inset ($V_S = 40$ mV, $I=1$ nA). b, Constant-current topography of a Cr adatom whose apparent height is 300 pm ($V_S = 50$ mV, $I=10$ pA, 2×2 nm²). c, Constant-current topography of CrH₂ on the very same atom whose apparent height has been reduced to 200 pm ($V_S = 50$ mV, $I=10$ pA, 2×2 nm²). d, Constant-height current image of CrH₂ ($V_S = 10$ mV, $I=2$ nA, 2×2 nm²). e, Height profile of Cr and CrH₂ in b and c, respectively. f, Current profile of CrH₂ in d.

In Figure 3.5d we show a constant height current image where two bright lobes are clearly visible. Such nodal plane (see Fig. 3.5f) suggest the presence of two atomic hydrogens bound to the Cr adatom rather than molecular hydrogen, which implies the low-temperature dissociation of the hydrogen molecule [26–32]. The transition metal atom could be dehydrogenated by voltage pulses or scans at $V_S > 1$ V, recovering the single-atom shape and spectroscopic features. This proves that atomic hydrogen (two, presumably) is responsible for the spectral changes.

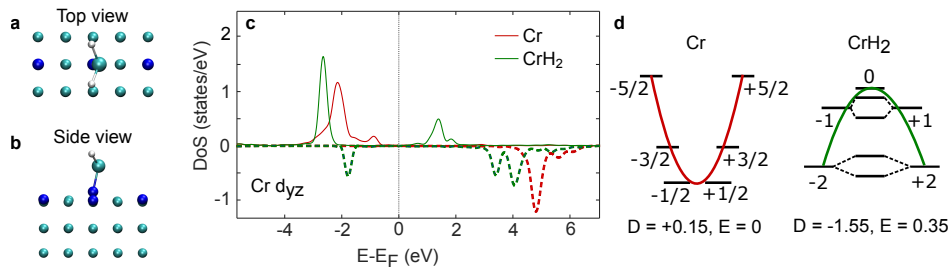


Figure 3.6: a, b, Top and side views of the DFT relaxed structure of CrH₂. c, Density of States (DOS) of the d_{yz} orbitals of Cr (red) and CrH₂ (green). Solid (dashed) lines represent majority (minority) states. d, Magnetic anisotropy energy diagrams for Cr and CrH₂.

DFT simulations found that the most stable structure for the hydrogenated Cr is with two hydrogen atoms in the configuration shown in Fig. 3.6a,b. This is in agreement with the nodal plane observed in the high-current images in Fig. 3.5d, which highlights the two-fold symmetry of the system. The hydrogen molecule dissociates by the Cr atom, and the transition metal atom becomes laterally displaced from the perpendicular axis over the substrate N site. The displacement from the axial position is expected to cause a large distortion of the ligand field felt by the Cr atom.

To fully interpret the large increase in the excitation energy, we compare the d -orbital occupation obtained from the projected density of states (PDOS) of Cr and CrH₂ (see Fig. 3.6c). The pristine Cr atom shows the spin distributed over the five singly-occupied d orbitals, leading to a total spin $S = 5/2$. Hydrogenation reduces the spin-polarization in the d_{yz} orbital and therefore no longer contributes to the total spin S (see Fig. 3.6c). Therefore, the presence of hydrogen decreases the total spin of the system from $S = 5/2$ to $S = 2$. The occupation of the d_{yz} orbital has also the additional effect of distorting the anisotropic environment of the Cr atom, switching from an easy-plane to an easy-axis configuration. Simulation of the differential conductance spectra by the phenomenological scattering model provided by Ternes [19] finds an increase in a factor of ten in the $|D|$ axial anisotropy parameter from $D_{\text{Cr}} = +0.15$ meV to $D_{\text{CrH}_2} = -1.55$ meV and the appearance of transverse magnetic anisotropy $E_{\text{CrH}_2} = 0.35$ meV (Fig. 3.6d). The presence of the two hydrogens along the y direction increases the anisotropy along that axis [33] and, as a consequence, it carries on a switch from yz -easy-plane to x -easy-axis configuration as sketched in Fig. 3.6d. Therefore, the inelastic excitations found at $V_S = \pm 0.4$ mV and ± 3.1 mV correspond to spin excitations from the ground state $|\psi_0\rangle = (|+2\rangle - | -2\rangle)$ to the two first excited states $|\psi_1\rangle = (|+2\rangle + | -2\rangle)$ and $|\psi_2\rangle = (|+1\rangle - | -1\rangle)$.

As mentioned above, the spectral lineshape of CrH₂ resembles the one of Fe adatoms on Cu₂N [8], and in fact both show a $S = 2$ ground state and an easy-axis magnetic anisotropy conformation. Nevertheless, according to our DFT simulations, chromium shows the easy-axis along the hollow direction while Fe atoms have it along the N row of the Cu₂N surface. Furthermore, CrH₂ sits on top of a N surface atom, while Fe adsorbs on the Cu site. In spite of the obvious similarities, the effect of hydrogen adsorption on Fe adatoms drives a decrease on the magnetic anisotropy as we will show in the next Section.

3.3 Iron adatoms as a prototypical highly anisotropic system

To address the hydrogenation effect and depict a more general picture of hydrogen adsorption on magnetic impurities, we revisited a well-known prototypical system that presents large both axial and transverse magnetic anisotropy: Fe atoms on the Cu₂N surface [8]. Most Fe impurities adsorb on Cu sites and bond to the two neighboring surface N atoms [8]. As it has been previously shown, Fe on Cu₂N [8] present spin excitations at $V_S = 0.2$ mV, 3.8 mV and 5.7 mV (see Fig. 3.7a) that reflect the large axial and transverse anisotropy found in the system, which amounts to $D = -1.55$ and $E = 0.31$ meV.

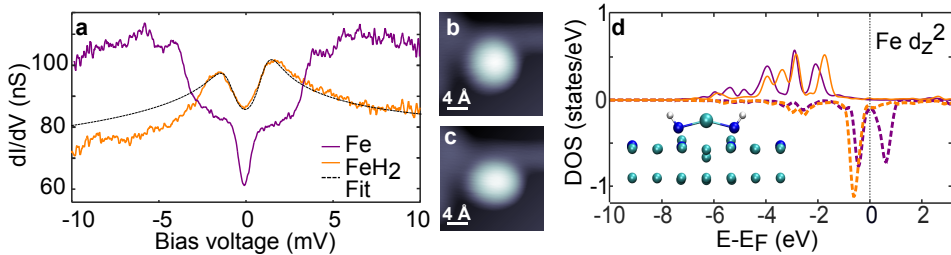


Figure 3.7: **a,** dI/dV spectrum of Fe (purple) and FeH₂ (orange) ($V_S = 10$ mV, $I=1$ nA). **b,** Constant-current topography of the Fe adatom after H₂ removal ($V_S = 50$ mV, $I=10$ pA, 3×3 nm²). **c,** Constant-current topography of FeH₂ showing an elongated shape ($V_S = 50$ mV, $I=10$ pA, 3×3 nm²). **d,** Density of States (DOS) of the d_{z^2} orbitals of Fe (purple) and FeH₂ (orange). The DFT relaxed structure of CrH₂ is shown in the inset.

We dosed H₂ on a Cu₂N sample with Fe atoms. In this case, the Fe atoms acquired an elongated shape, maintaining an apparent height of around 200

pm (see Fig. 3.7b,c). In contrast to the multiple spin excitations found in the pristine atoms, hydrogenated iron actually showed a single inelastic step at $V_S = 0.75$ mV but enclosed on a wide resonance centered at zero bias as shown in Fig. 3.7a. As described for the case of Cr atoms, this is indicative of a low anisotropic environment where Kondo scattering events are responsible for the broad zero-bias resonance. However, as we will describe below, the effect of hydrogen atoms on Fe over the Cu site is fundamentally different from the case of Cr on the N site.

In agreement with the elongated appearance of FeH_2 in the STM images (Fig. 3.7b,c), DFT simulations revealed that hydrogen atoms bond to the adjacent N atoms rather than to the Fe impurity, as shown in the inset of Fig. 3.7d (note that Fe lies on top of the surface Cu atoms). Similarly to the Cr case, upon hydrogen adsorption the total spin moment is reduced. We found that the saturation of the N surface atoms by hydrogen decreases the net charge transfer from the Fe adatom from $\Delta N_{Fe} = -0.86 \text{ e}^-$ to $\Delta N_{Fe} = -0.67 \text{ e}^-$. This leads to a reorganization of the d -orbitals occupation where the minority spin states of the d_{z^2} become fully occupied, quenching its spin-polarization (see Fig. 3.7d). The d_{xy} , d_{xz} and d_{yz} orbitals remain singly occupied leading to the total spin $S = 3/2$.

Close inspection of the magnetic anisotropy parameters obtained by the fit [19] of the dI/dV spectra in Fig. 3.7a revealed a suppression of the transverse magnetic anisotropy E accompanied by a reduction in the axial parameter down to $D = 0.38$ meV (Fig. 3.7a). In addition, the hydrogen distorts the Cu_2N lattice by displacing the N atoms, which increases the Fe-N bond distance and therefore enhances hybridization with the surface Cu atom (see inset in Fig. 3.7d). The resulting scattering from the electron bath gives rise to the Kondo tail observed in the STS measurements (Fig. 3.7a), split by the spin excitation due to the remaining axial magnetic anisotropy.

3.4 Conclusions

Our combined STM measurements and DFT calculations prove the controlled manipulation of the magnetic properties of Cr and Fe impurities. We found that the total spin and the coupling to the substrate of Cr adatoms can be controlled by the adsorption site, leading to $S = 2$ or $S = 5/2$ on Cu and N sites, respectively. The Cu site favours a higher hybridization with the electron bath, visible in the dI/dV spectra as a broad Kondo tail, while the N site leads to a low-anisotropic half-shell filled for the Cr impurities.

We found that the adsorption of a hydrogen molecule by Cr impurities on the N site changed the d -shell occupancy leading to a decrease in the total spin to a value of $S = 2$. The presence of hydrogen in Cr adatoms

undergoes a transition from weak easy-plane to strong easy-axis anisotropy. Furthermore, magnetic anisotropy was substantially enlarged, presumably due to the displacement from the axial position by the presence of the two hydrogen atoms.

We found obvious similarities in the spectroscopic lineshape of CrH₂ and Fe impurities on the Cu₂N substrate. However, the presence of hydrogen decreases magnetic anisotropy in the Fe case, as opposed to Cr impurities. This can be understood due to the dissociation and subsequent bond of the hydrogen to the neighbouring surface N atoms, instead of the direct interaction with the Fe impurities. As in the Cr case, hydrogen slightly changes the Fe adsorption site, pulling it down towards the metal and enhancing its hybridization. As a consequence, Kondo scattering events become stronger and develop a zero-bias resonance for FeH₂.

Chapter 4

Orbital-selective spin excitations in a magnetic porphyrin

Porphyrin molecules offer a versatile platform for studying magnetism down to the single atom. The porphyrin core accommodates the magnetic impurity, and the ligands attached at the periphery decouple it from the substrate. Thus, a variety of ligands and magnetic atoms can be combined in order to tune the magnetic ground state, the hybridization with the substrate and even the coupling between different porphyrins. Indeed, the broad range of possible properties together with the high stability of these organic molecules have been the breeding ground for the emergence of many works studying the manipulation of the molecular spin by spatial distortions [34–41], or by tuning the molecular interaction with the local environment [13, 42–46].

In this Section we show the study of the magnetic properties of iron tetraphenyl porphyrin (FeTPP) molecules. Spatially-resolved tunneling spectra reveal that the inelastic spin excitation extends beyond the iron site, changing shape and symmetry along the molecule. Combining Density Functional Theory simulations performed by Dr. Ane Sarasola (UPV/EHU and DIPC, San Sebastián, Spain), Dr. Aran García-Lekue (DIPC, San Sebastián, Spain) and Prof. Daniel Sánchez-Portal (CFM and DIPC, San Sebastián, Spain) with a phenomenological scattering model [19], we show that the extension and lineshape of the inelastic signal are due to excitation pathways assisted by different frontier orbitals.

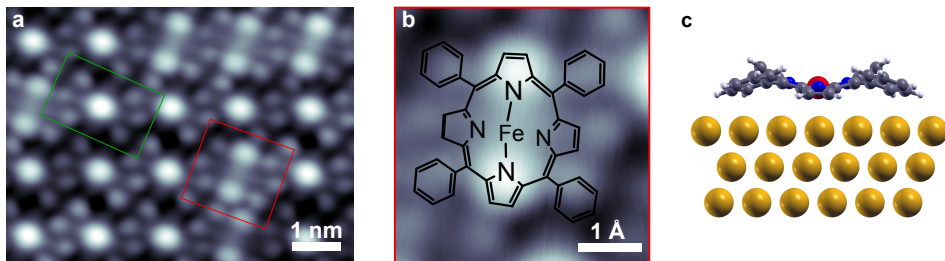


Figure 4.1: a, Topographic STM image ($7 \times 5 \text{ nm}^2$) of a close-packed island of FeTPP (red box) and FeTPP-Cl (green box) molecules on Au(111). ($V_S = 0.25 \text{ V}$, $I=10 \text{ pA}$). b, Zoom of a single FeTPP molecule and molecular structure superimposed. c, Cross section of the DFT relaxed structure of the FeTPP on the Au(111) surface (3 gold layers) showing the saddle conformation acquired upon adsorption.

4.1 Surface adsorption and spin excitations on FeTPP

STM images show that the porphyrin molecules arrange in close-packed islands on the Au(111) surface (Fig. 4.1a) and appear with a protrusion at the center (green box in Fig. 4.1a) that is attributed to the Cl ligand of the intact FeTPP-Cl molecule. A fraction of the molecules exhibits instead two lobes. They correspond to the dechlorinated species FeTPP (Fig. 4.1b) which adopt a saddle conformation upon adsorption (Fig. 4.1c). FeTPP molecules can be controllably obtained by removing the Cl ligand from the FeTPP-Cl molecules using tunneling electrons (see Fig. 4.2) or by annealing the substrate [37]. The dechlorination process changes the Fe oxidation state from Fe^{+3} to Fe^{+2} and decreases the total spin from $S = 3/2$ to $S = 1$ [37, 38, 47].

STS measurements over the molecules reveal steps in conductance at symmetric bias values (see Fig. 4.2), associated to the onset of inelastic tunneling [14, 24]. While the steps on the FeTPP-Cl molecules appear at $V_S = \pm 1.7 \text{ mV}$ (Fig. 4.2d), the removal of the Cl ligand increases the excitation energy to $V_S = \pm 7.4 \text{ mV}$ (Fig. 4.2e).

In both cases, the inelastic spectra show a dependence with the applied magnetic field (see Fig. 4.3), which agrees with changes of the spin-multiplet of Fe-porphyrin moieties [37, 38, 48]. In the case of the FeTPP-Cl molecule, a dip at zero bias appears with magnetic field, associated to the Zeeman splitting of the $S_z \pm 1/2$ ground state, expected for a high half-integer spin with easy-plane anisotropy [37, 38, 48] (see Fig. 4.3a). The effect of the magnetic field on the dechlorinated porphyrin FeTPP is more faint for the small magnetic fields available, but still visible as a slight change in the

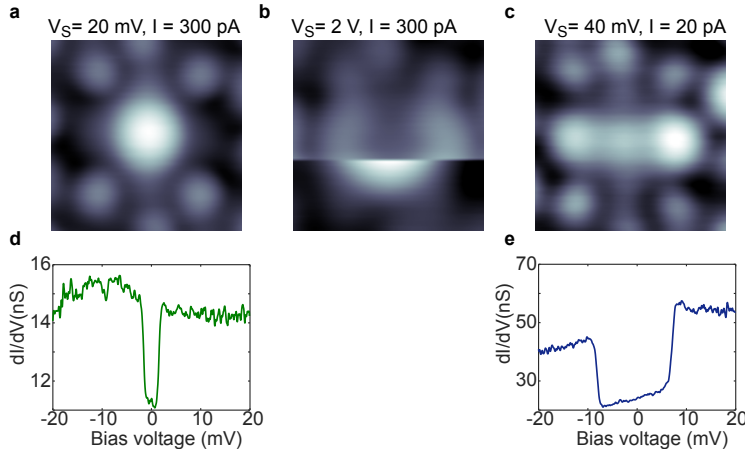


Figure 4.2: a, STM topography of a FeTPP-Cl molecule. b, STM topography of the dechlorination process. The STM tip started to scan the molecule from the bottom part of the image and in the middle of the scan the chlorine ligand was removed. c, STM topography of the dechlorinated FeTPP molecule. d, dI/dV spectra over the chlorinated FeTPP-Cl molecule. e, dI/dV spectra over the FeTPP molecule.

slope of the step at the excitation energy (see Fig. 4.3b). To resolve these changes, we measured the second derivative of the current. At $B_z = 0 \text{ T}$, a single peak is observed. The peak broadens with increasing B_z and evolves into a split peak at $B_z = 2.8 \text{ T}$ (see Fig. 4.3d). This confirms the expected magnetic ground state of FeTPP, an integer spin with easy-plane anisotropy, in which the magnetic field splits the $S_z = \pm 1$ excited states. We show in Fig. 4.3e-f the expected behaviour of the ground state and first excited state of FeTPP-Cl and FeTPP, respectively, which match the experimental results. We, thus, associated these steps to spin excitations induced by tunneling electrons, and discard any possible vibrational origin [49].

We find a striking spatial distribution of the spectroscopic features of the FeTPP species (see Fig. 4.4a). While the energy position of the inelastic conductance steps remains the same ($V_S = \pm 7.4 \pm 0.5 \text{ mV}$) all over the molecule, their symmetry varies as we move off-center towards the brighter pyrroles. A stacking plot of point dI/dV spectra across the FeTPP molecule (Fig. 4.4b) shows inelastic steps with a rather symmetric lineshape over the pyrroles and with strong antisymmetric character over the Fe site. It is remarkable that the energy positions of the conductance steps remain nevertheless constant, indicating that the same excitation is the origin for the inelastic features across the molecule. The spin excitation is only observed along the axis formed by the brighter pyrroles (marked in the inset in Fig.

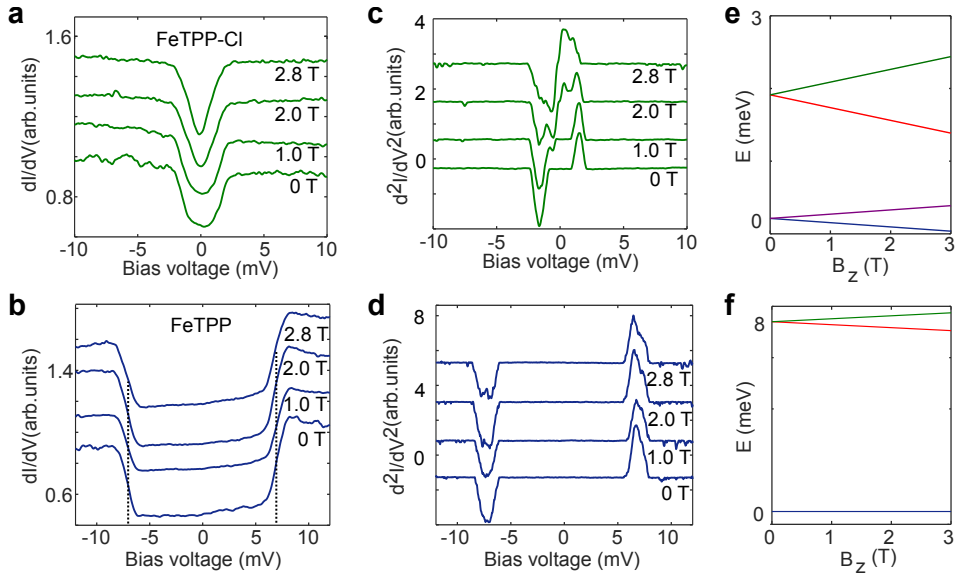


Figure 4.3: a, b, dI/dV spectra of FeTPP-Cl and FeTPP molecules as the out-of-plane magnetic field is increased, respectively. c, d, d^2I/dV^2 spectra of FeTPP-Cl and FeTPP molecules as the out-of-plane magnetic field is increased, respectively. e, f, By diagonalization of the spin Hamiltonian, we obtained the expected magnetic field dependence of the ground state and first excited state showing the Zeeman splitting of FeTPP-Cl and FeTPP, respectively.

4.4b), and is absent over the two other pyrroles (grey dashed line in Fig. 4.4a).

In a first approximation, the spin excitation energy is determined by the magnetic anisotropy of the molecule on the surface, which can be modeled with a phenomenological spin Hamiltonian [20, p. 15] $\hat{H}_s = D\hat{S}_z^2 + E(\hat{S}_x^2 - \hat{S}_y^2)$, where $\hat{S}_x, \hat{S}_y, \hat{S}_z$ are the three components of the spin operator, and D and E the axial and transverse anisotropy parameters, respectively. We find that the inelastic step splits by applying a magnetic field perpendicular to the surface, in accordance with Zeeman shifts of a $S=1$ multiplet. Hence, the excitation at $V_s = \pm 7.4$ mV corresponds to a transition from the $|m_S = 0\rangle$ ground state to the $|m_S = \pm 1\rangle$ multiplet, and the excitation energy is the axial anisotropy constant $D = 7.4$ meV (similar to the one reported for FeTPP crystals [50]).

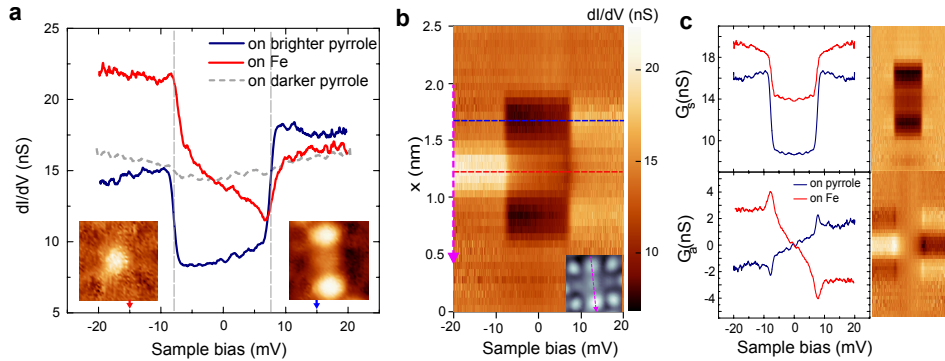


Figure 4.4: a, Characteristic dI/dV spectra of FeTPP measured over one of the two bright pyrrole groups (blue) and over the central Fe ion (red). As a reference, we add a spectrum acquired over the dark pyrroles with the same tip (dashed grey), showing the absence of features in this range. ($V_S = 20$ mV, $I=300$ pA, $V_{rms} = 50$ μ V). The insets are 1.7×1.7 nm² constant current dI/dV maps at $V=-15$ mV and $V=+15$ mV of the topography image shown as inset in b. b, Stacking plot of point dI/dV spectra (40 curves, 2.5 nm) along the axis of a FeTPP molecule (as shown in the inset). c, Symmetric ($G_s = \frac{1}{2}(G_{V>0} + G_{V<0})$) and antisymmetric ($G_a = \frac{1}{2}(G_{V>0} - G_{V<0})$) components of the dI/dV spectra of a and their flattened spatial distribution along the axis of the FeTPP molecule, as in b.

4.2 Higher order scattering processes

The above spin-model successfully predicts excitation energies and transition rates [20]. However, to fully describe the spectral shape of inelastic tunneling processes spin-electron interactions must be taken into account. Electron scattering mechanisms contributing to the inelastic signal can be described by Hamiltonian terms of the form $H_{int} \simeq \mathcal{U} + J \cdot \mathbf{s} \cdot \mathbf{S}$. The exchange term J describes the transfer of energy and angular momentum by electrons (with spin \mathbf{s}), and accounts for excitations of the molecular spin \mathbf{S} . The potential scattering term \mathcal{U} reflects charge scattering processes by partially occupied localized states [18, 19], and its role has typically been disregarded in magnetic systems.

Most of the scattering processes contribute to the tunneling conductance with bias-symmetric components. Asymmetry in the spectra of Kondo systems has been generally attributed to Fano-like interference of the exchange-scattering channel with other tunneling paths [51]. While in the present case Kondo-screening can be excluded due to the large anisotropy, high-order scattering processes still apply. In particular, it has been shown [19]

that the presence of a potential scattering channel can produce a peculiar bias-asymmetry in the conductance spectra. A finite \mathcal{U} amplitude leads to antisymmetric components in the dI/dV spectra, arising already at biases below the excitation energy and with small logarithmic peaks/dips at the excitation onset. As a result, the shape of the inelastic features in dI/dV spectra reflect the degree of particle-hole asymmetry of the system (Fig. 4.6).

Following this interpretation, we separate the symmetric G_s and antisymmetric G_a parts of the spectra in Fig. 4.4a,b as indicated in the caption. The resulting plots (Fig. 4.4c) reveal that the inelastic fraction in the symmetric component is larger over the pyrrole groups by a factor of 3 (inelastic fraction $\frac{\Delta G_s}{G_s}$ amounts to 0.9 and 0.3 over pyrroles and Fe, respectively), while the antisymmetric component G_a has opposite sign on each site, and is 2 times larger over the Fe ion. Furthermore, the G_a component shows characteristic dips and peaks at the onset of excitation, which resemble the antisymmetric components of higher order terms associated to a non-zero potential scattering amplitude, rather than other known sources of asymmetry, such a Fano-like interference with other tunneling channels.

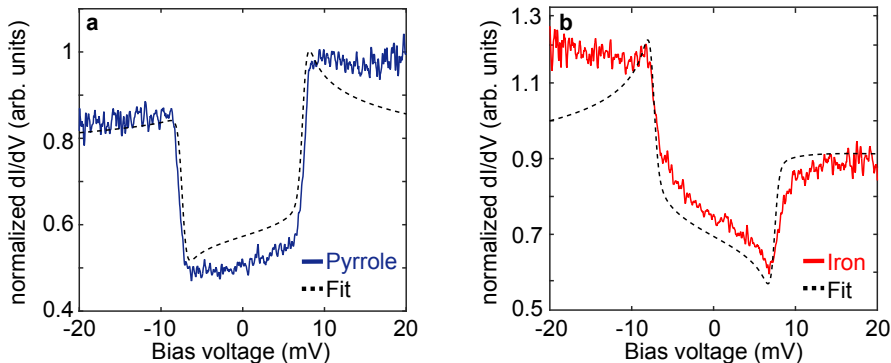


Figure 4.5: a, dI/dV spectra of FeTPP measured over the pyrrole (solid line) and the fitting results (dashed line) b, dI/dV spectra of FeTPP measured over the Fe (solid line) and the fitting results (dashed line).

position	D (meV)	U	$\rho_s J$	$-\epsilon_d/U_d$
pyrrole	7.4	-0.4	-0.2	0.7
iron	7.4	0.8	-0.2	0.1

Table 4.1: Table I: Fitting parameters for the experimental results shown in Figure 4.5.

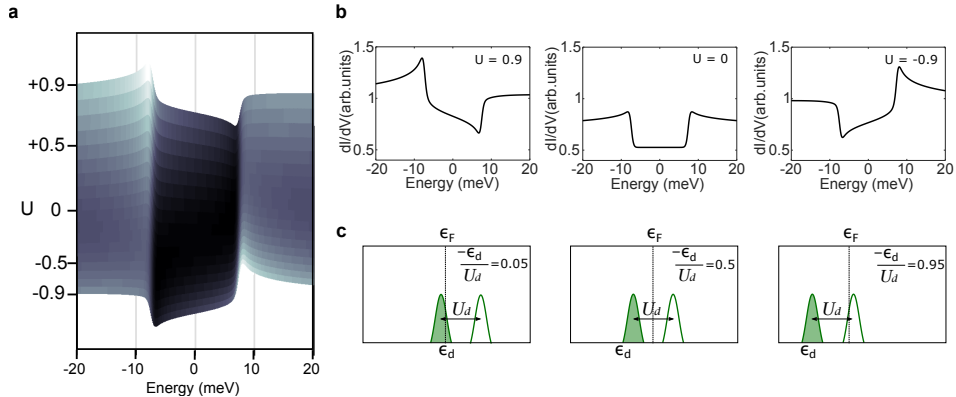


Figure 4.6: a, Evolution of the simulated dI/dV spectra with the ratio of potential and exchange scattering amplitudes $U = \frac{U}{J}$ [19]. b, Three representative cases, namely electron-hole symmetry ($U = 0$) and mixed-valence regime ($U = \pm 0.9$). c, Representation of the single-impurity Anderson model parameters for the three selected cases in b.

We thus fitted the dI/dV spectra of Fig. 4.4a using a (second-order scattering) phenomenological model developed by Ternes [19] (for fit results see Fig. 4.5 and Table 5.1). The stronger antisymmetric component of the curve taken over the Fe ion is reproduced using a large and positive ratio between potential and exchange scattering amplitudes, i.e. $U = \mathcal{U}/J = 1 + 2\frac{\epsilon_d}{U_d} = 0.8$, whereas the opposite and weaker antisymmetric component of the curve taken on the pyrroles is due to a smaller and negative ratio, $U = -0.4$. In Fig. 4.6a we show the evolution of the asymmetry in the spectra as we sweep the parameter U . The inelastic spectra show a characteristic asymmetry, that changes sign as we move from the hole ($U = 0.9$) to the particle ($U = -0.9$) mixed-valence regimes, while at the particle-hole symmetry point the spectrum is symmetric. Three cases are individually plotted for clarity in Fig. 4.6b, resembling the asymmetry found in the experiments.

The microscopic Anderson model [17–19] provides a physical interpretation for the phenomenological parameter U obtained from the fit to the experimental spectra. As described by the Schrieffer-Wolff transformation [18], U depends linearly on the ratio between energy position of the singly occupied spin state and the on-site Coulomb energy ϵ_d/U_d . This relation conveys information about the relative alignment of the spin energy levels with respect to the Fermi energy. In Fig. 4.6c we included the representation of the orbital energy position for the three cases shown in Fig. 4.6b.

From the fitting of our experimental data for the more symmetric STS lineshape taken on the pyrroles, we obtain $\epsilon_d = -0.7U_d$, which can be interpreted as a spin state close to the electron-hole symmetry point ($\epsilon_d = -0.5U_d$), where potential scattering would be absent ($U = 0$). In contrast, from spectra on the Fe site we obtain $\epsilon_d = -0.1U_d$ a situation where the spin is close to the mixed-valence regime and the potential scattering is significant. Although both scenarios deviate from the electron-hole symmetry point, on the central Fe ion the situation is extreme and, therefore, the spectra shows a larger antisymmetric component. Furthermore, the larger electron-hole symmetry over the pyrrole groups agrees with the larger inelastic fraction over this point [52]. Even if the Anderson model does not capture the complexity of the spin density distribution of a metal-organic system, it still provides a suitable interpretation for the energy alignment of the orbitals mediating the excitation in terms of electron-hole asymmetry.

4.3 Frontier orbitals of FeTPP

The energy alignment of the FeTPP frontier orbitals can be explored in spectra measured in a wider bias range. In consistency with the above-described picture, we find two electronic resonances around the Fermi level, each showing a different linewidth and spatial dependence (Fig. 4.7a). While a sharp resonance appears at $V_S = +150$ mV on the pyrroles, a broad state is found at negative bias over the Fe site. The dI/dV stacking plot along the molecular axis (4.7b) captures these differences, and reveals an orbital pattern similar to that of the spin excitations (Fig. 4.4b). The dI/dV maps in Fig. 4.7c further localize the positive and negative frontier orbitals along two of the four pyrroles and over the Fe center, respectively. This agrees with a molecular symmetry breaking, also observed in the spin excitation maps (Fig. 4.4a). We note that the broad negative-bias resonance on the Fe ion crosses through zero bias, revealing a situation close to the mixed-valence regime, in agreement with the outcome of the Anderson model from above.

In order to identify the orbital character of the frontier spectral features of FeTPP on Au(111) we analyzed its electronic configuration and spin state by means of DFT simulations based on the SIESTA code [53]. We find that adding a Hubbard-like term with $U_d = 2$ eV to describe the Coulomb interactions between electrons in the Fe $3d$ shell is crucial to reproduce the orbital alignment around E_F observed in the experiment [54]. For the free-standing molecule, our results confirm the well-known multi-configurational character of the ground state of FeTPP [55, 56]. Correspondingly, we found almost degenerate solutions with quite different fillings of the levels associated with the metallic center and the same total spin. On the Au(111)

surface the molecule adopts a distorted saddle configuration, as previously reported for porphyrins on surfaces [39]. Fig. 4.8a shows the density of states of FeTPP/Au(111) projected on Fe *d* orbitals (PDOS). The FeTPP on Au(111) has a magnetic moment of $2.12 \mu_B$ ($S = 1$) shared between frontier states, which have strong character on d_{z^2} and d_π orbitals of the Fe ion (see the sketch in Fig. 4.8b). The d_{xy} and $d_{x^2-y^2}$ -derived states are fully occupied and empty, respectively, and largely localized due to their weak interaction with the metal substrate. The d_{z^2} -derived state has a net spin polarization of $0.75 \mu_B$ and is quite broadened as a consequence of its large hybridization with the substrate. The d_π -derived states appear with a broken degeneracy caused by the saddle-like distortion of the molecular backbone on the substrate. The lowest energy configuration finds d_{yz} orbital with larger spin density, while the d_{xz} is almost completely occupied and, thus, exhibits a substantially smaller spin polarization. Namely, the spin polarization coming from the d_π orbitals is dominated by the contribution from d_{yz} . The computed PDOS thus pictures the multi-orbital character of the spin polarization of this system.

The spatial spin excitation pattern observed in the experiment is a consequence of different molecular states involved in the tunneling through the molecule. In Fig. 4.8b we compare the PDOS on Fe orbitals and on the upper-pyrrole groups (bright pyrroles). The former resemble the dI/dV spectrum at the center of the molecule (Fig. 4.7a) with larger DOS at the negative part of the energy spectrum plus some weight above E_F . This proves that the tunneling transmission on the Fe ion is governed by Fe *d*-resonances. The larger overlap of this Fe-*d* manifold with E_F , closer to a mixed-valence configuration, is the main cause of the larger asymmetry of the spin excitation features observed over the Fe site. In contrast, the PDOS on the upper-pyrrole atoms exhibit only a resonance at positive energy, which correlates with the dI/dV peak measured over the protruding pyrrole groups (Fig. 4.7a). The resonance is composed of pyrrole states and empty d_{yz} components of the Fe ion, having a strong hybrid Fe-ligand character. As a consequence, this resonance becomes weakly spin-polarized (Fig. 4.8c). The absence of spin excitation over the lower pyrroles agrees with the lack of spin polarization of the hybrid ligand- d_{xz} states. Therefore, tunneling through pyrrole-Fe hybrid states can effectively excite the spin of the Fe ion [45], whereas the smaller overlap of the d_{yz} resonance with E_F agrees with the more symmetric excitation lineshape observed in the experiment.

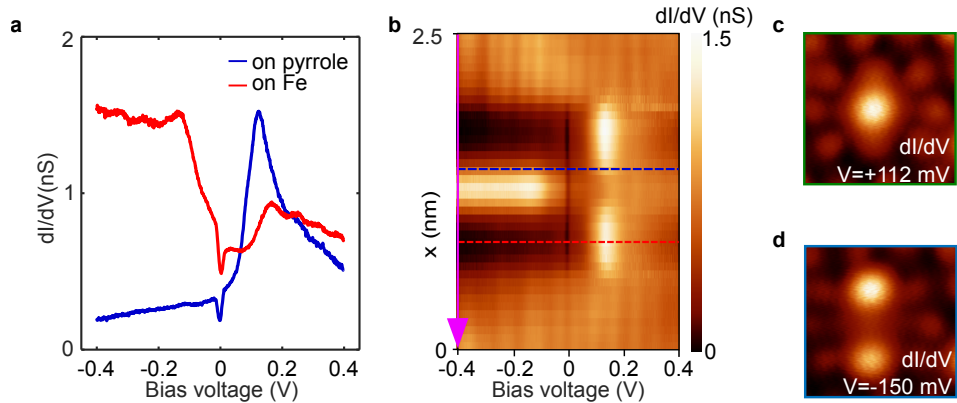


Figure 4.7: a, dI/dV spectra of FeTPP measured on the two bright pyrrole groups (blue) and on the central Fe atom (red) ($V_s = 0.4$ V, $I=300$ pA, $V_{rms} = 2$ mV). The spectra is measured in a wider range as in Fig. 4.4a to capture the shape and position of frontier orbitals. b, Stacking plot of point dI/dV spectra (40 curves, 2.5 nm) along the FeTPP molecule showing the spatial localization of dI/dV signal along the axis determined by the two bright pyrroles. c, d, Constant height conductance maps at the energy of the resonances observed in a.

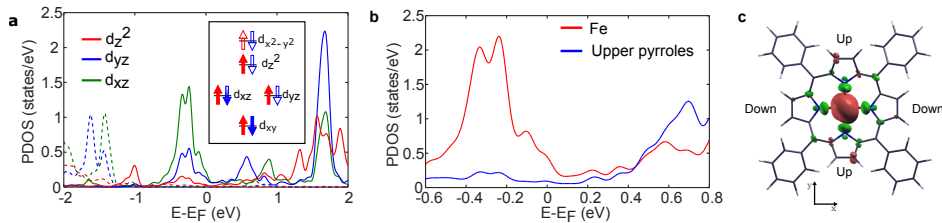


Figure 4.8: a, Spin-polarized DOS of the FeTPP/Au(111) system projected on Fe d_{xz} , d_{yz} and d_{z^2} orbitals (dashed/solid lines represent majority/minority spin states). Inset: Simplified scheme describing the occupation of Fe 3d levels for the adsorbed FeTPP (red/blue arrows indicate majority/minority spin states). The partial color filling of the d_{π} multiplet represents the distribution of their net spin 1/2 polarization obtained from DFT, which is essentially localized in the d_{yz} orbital; the total molecular spin is $S = 1$. b, Total DOS of the FeTPP/Au(111) system projected on Fe states and on C and N states of the upper pyrrole moieties. c, Spin polarization isosurface obtained for the FeTPP/Au(111) system by subtracting occupied states with spin up and down (red/green describe spin density isosurfaces); upper pyrroles are at the top & bottom of the structure; the Au(111) surface has been omitted from the plot for clarity).

4.4 Conclusions

In summary, we have demonstrated that the spin excitation of a S=1 metal-organic molecule can be selectively excited through two different inelastic tunneling channels. Every channel is mediated by a molecular state with different spatial extension and produces inelastic features with a characteristic asymmetry. We have shown that the asymmetry is a consequence of the spin-polarized molecular state being out of the particle-hole symmetric case. Thus, interpretation of the inelastic spectra in terms of a phenomenological scattering model can be used to detect the alignment of spin-hosting states in molecular magnets and to infer their proximity to a mixed-valence configuration.

Chapter 5

Surface-induced quench of intramolecular exchange coupling in bimetallic porphyrin complexes

In previous sections we have shown the study of single spins in two different environments: on top of an insulating layer (Section 3) and embedded in a organic molecule (Section 4). The control of the atomic spin states requires stable magnetic structures. This can be accomplished by the arrangement of single atoms in compact structures [?, ?], where the direct exchange interaction between the d -orbitals drives the ferro or antiferromagnetic order. In that context, the bottom-up approach towards obtaining stable spins resulted in the realization of molecular magnets [?], where a high spin is accomplished due to the indirect coupling between transition metal atoms coordinated with organic ligands.

If two spins are far away, no direct interactions are expected. However, the proximity of the two magnetic impurities may enable an interaction (exchange coupling), producing the spontaneous alignment of their magnetic moments. Direct exchange requires the overlap of the atomic orbitals of the two magnetic adatoms. At intermediate distances, indirect exchange coupling may arise via two different mechanisms: Ruderman-Kittel-Kasuya-Yosida (RKKY) [57–59] and superexchange [60, 61]. The first describes the indirect interaction between two magnetic moments through the scattering with the conduction electron band [62]. Superexchange mechanisms describe the indirect coupling between two magnetic moments through a non-magnetic bridge, which mediates virtual hopping processes between the two spins [?, 63].

In this Section we propose a platform for studying indirect magnetic coupling in an organic molecule composed by two porphyrin cores. Each of them hosts an iron atom that possess a magnetic moment oriented in the molecular plane. DFT simulations found a strong superexchange interaction between the Fe atoms for the free molecules, that quenches when the molecule was relaxed on the metallic surface. Furthermore, substrate-activated dehydrogenation processes lead to three different molecular structures. We found that distortions among the two porphyrin cores affect both the electronic configuration and the magnetic anisotropy configuration of each Fe atom. The planarization of the organic platform leads to the shift of an electronic state close to the Fermi level, driving the system towards the mixed valence regime.

This is the result of an interdisciplinar collaboration with Dr. Deng-Yuan Li and Dr. Pei Nian Liu (Shanghai Key Laboratory of Functional Materials Chemistry and Institute of Fine Chemicals, China), who synthesized the organic molecules; Dr. Guowen Kuang and Prof. Nian Lin (Hong Kong University), who designed the experiment; and Dr. Paula Abufager (Instituto de Física de Rosario, Argentina) and Prof. Nicolás Lorente (CFM and DIPC, San Sebastián, Spain) who carried out the DFT simulations.

5.1 Three molecular structures

Figure 5.1a shows the chemical model of the synthesized free-ion double porphyrin molecules investigated here. Two diphenyl-porphyrin (2-DPP) cores are covalently connected via a C-C bond. Due to intramolecular steric hindrance, in the relaxed structure of the free molecule, the two porphyrin cores are rotated with respect to each other. The molecules were vacuum sublimated on a clean Au(111) surface at room temperature. We co-deposited Fe atoms to induce the metalation. Subsequent annealing to $T = 200$ °C triggered the metalation of the double porphyrin and the formation of 2-FeDPP.

Upon adsorption, most of the 2-FeDPP molecules arrange in self-assembled molecular chains as shown in Fig. 5.1b, stabilized by the interaction of the phenyl rings. We found three kinds of molecular species, according to their sub-molecular structure in STM images (Fig. 5.2a-c). All the species showed the four phenyl groups at the periphery of the molecule, and most of them (78 % of the cases inspected) with two additional fainter lobes at the Fe sites (see Fig. 5.2c). However, a smaller fraction appeared instead with either one (19%) or two (3%) brighter protrusions at the positions of the inner pyrrole groups (Fig. 5.2b and 5.2a, respectively). We attribute these bright protrusions to the up-lifted inner pyrrole groups of the

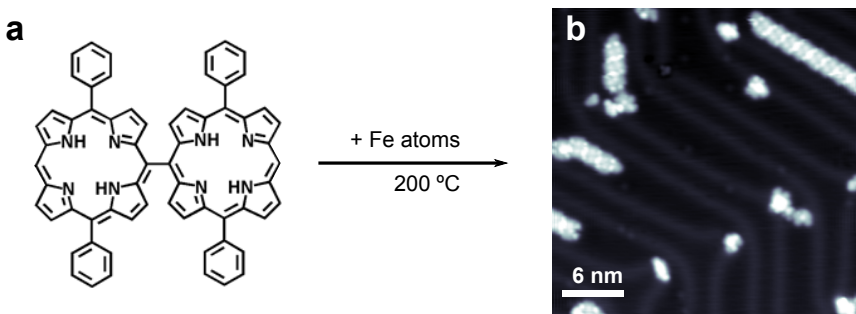


Figure 5.1: a, Molecular model of the double porphyrin before metalation. b, Constant-current STM topograph showing several self-assembled chains of molecules. ($V_S = -1$ V, $I = 10$ pA).

2-FeDPP as a consequence of the steric hindrance, as represented with grey shade in Figs. 5.2d-f. The planar adsorption configuration imposed by the metal surface forces the two porphyrin cores to lie parallel, resulting in the twist of the pyrroles due to the steric hindrance between them. Therefore, we attribute the absence of such protrusion in the species of Fig. 5.2b and 5.2c to the creation of either one or two additional intramolecular covalent bonds between the two porphyrin cores through a surface-activated dehydrogenation process [64]. As indicated in the molecular structures of Figs. 5.2d-f, the new covalent bonds connects the two porphyrin cores, leading to the partial or complete planarization of the 2-FeDPP molecule, respectively.

Density Functional Theory (DFT) simulations of the adsorbed molecular structures confirm our assignment. 2-FeDPP undergoes an overall planarization of the molecular structure upon adsorption on the metal surface, with a distortion of the two coincident pyrroles. Simulation of the two cyclodehydrogenated species of Fig. 5.2b,c support that the additional intramolecular covalent bonds increases the planarization of the molecules. To further corroborate the interpretation of submolecular structure of Figs. 5.2a-c, we simulated the STM images of the adsorbed species as Density of States (DOS) maps at constant height over the sample. According to the Tersoff-Hamman approximation [?], these maps render the basic details of the STM topographs at zero energy, which can be interpreted at different bias values. The results, shown in Fig. 5.2g-i, reproduce fairly well the experimental STM images. The Fe ions appear as faint protrusions at the center of each porphyrin core, and the presence of a twisted pyrrole is imaged as a brighter feature at the joint between them. In the following, we refer them as *twisted*, *half-fused* and *fused*, respectively.

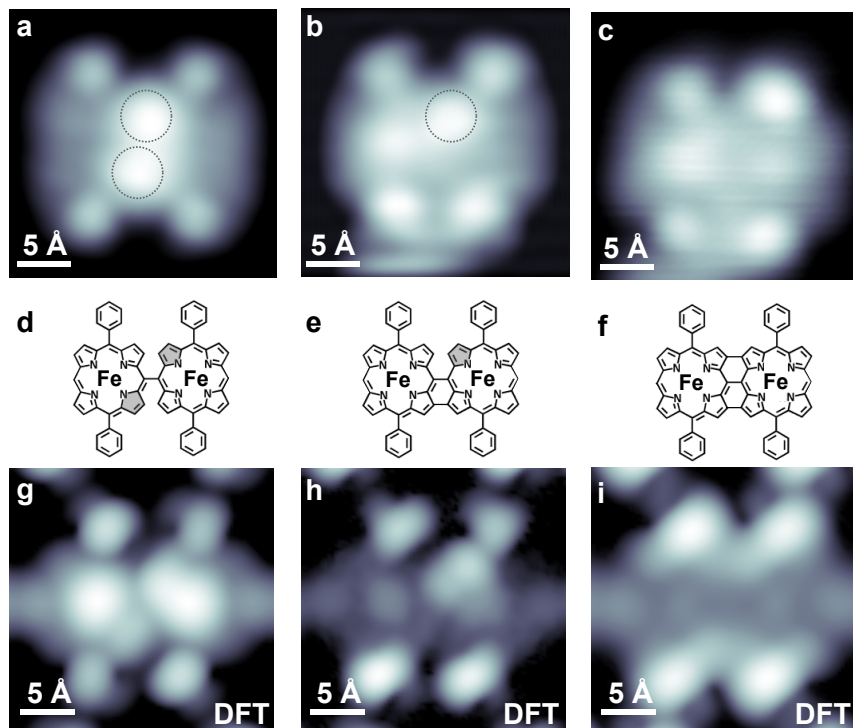


Figure 5.2: a-c, Constant-current STM topographs of the three kinds of molecules found (twisted, half-fused and fused, respectively). ($V_S = -0.25$ V, -1 V, 0.1 V, respectively. $I = 10$ pA). d-f, Molecular model of the three kinds of metalized molecules. g-i, DFT simulation of STM topographs (-0.5 V, -1 V, 1 V, respectively). The relaxed structures preserve two Br atoms at the meso positions that in the experiments are presumably gone at the annealing temperatures.

5.2 Spectroscopic fingerprints of 2-FeDPP

To explore the magnetic properties of the Fe centers in each of the 2-FeDPP species, we performed dI/dV spectra, which shows that each molecular structure has different magnetic properties. *Twisted* molecules show identical dI/dV spectra on both Fe positions: a narrow double step at $V_S = \pm 0.9$ and ± 4.1 mV (see Fig. 5.3a). *Half-fused* molecules showed different spectroscopic signatures on the two Fe sites: one showed a higher energy step at $V_S = \pm 7.4$ mV while the other Fe site showed inelastic excitations at $V_S = \pm 0.9$ and ± 4.1 mV, identical to the ones exhibited by *twisted* molecules (see Fig. 5.3b). Surprisingly, in the *fused* molecules the low-energy features

appeared fainter, describing an asymmetric lineshape in the energy range of $V_S = \pm 5$ mV.

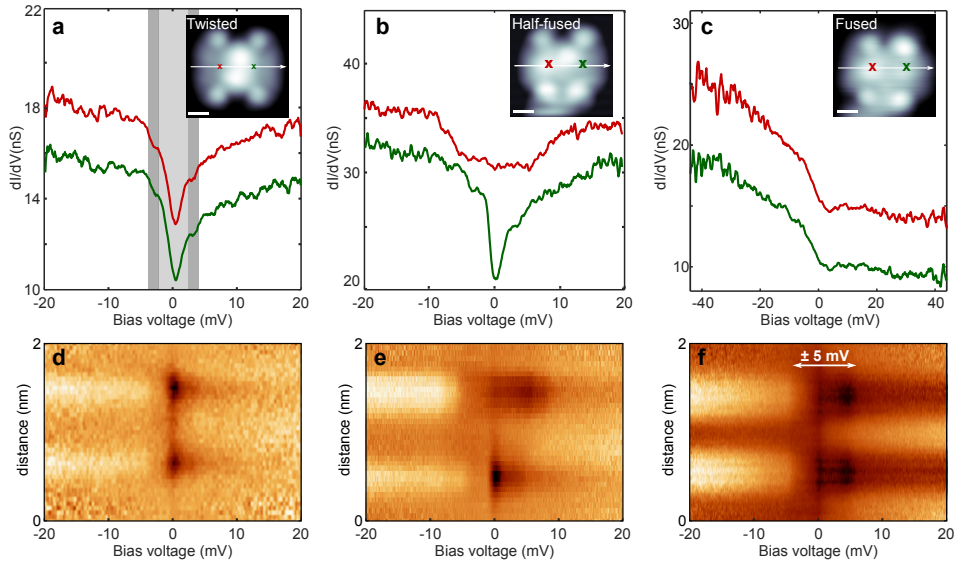


Figure 5.3: a, b, c dI/dV spectra measured at the Fe positions as indicated in the insets. (The scalebar represents 5 Å). d, e, f, Stacked-plot of dI/dV spectra along the molecules as indicated in the insets in a, c, e, respectively. ($V_{S,a,b,d,e,f} = 20$ mV, $V_{S,c} = 40$ mV, $I = 300$ pA).

5.2.1 Vanishing of exchange coupling upon surface adsorption

The energy-symmetric steps in dI/dV spectra are attributed to inelastic tunneling [14,24], and for magnetic species they can be related to excitations of the molecular spin multiplet in the presence of magnetic anisotropy and spin-spin interactions. As shown in Fig. 5.3d-f, the inelastic features in the three species appeared localized at the Fe sites and fade away between them. Furthermore, *half-fused* molecules show in one of the Fe sites the characteristic spin excitation spectra of single Fe porphyrins [41,65], while on the other Fe site showed that of the *twisted* species. Hence, magnetic coupling between the two Fe centers appears to be negligible.

The absence of intramolecular exchange coupling between the two Fe spins deduced from the experiments contrasts with the strong magnetic coupling in gas-phase, as computed by DFT. Table 5.1 lists the values of E_{FM-AFM} , the total energy difference between the parallel (FM) or anti-parallel (AFM) alignment of the spins at each Fe ion. We find that the

indirect exchange interactions between the Fe magnetic moments amounts to values around 10 meV for all the cases, and switches from AFM to FM as the molecule is converted from *twisted* to *fused*. However, upon adsorption on the gold surface, DFT also finds that the exchange interaction between the Fe centers vanishes and the spins can be pictured as independent, in agreement with our experimental results (see Table 5.1).

	$E_{FM-AFM, Twisted}$	$E_{FM-AFM, Half-fused}$	$E_{FM-AFM, Fused}$
Gas phase	+10 mV	-9.6 mV	-12 mV
On-surface	0 mV	-0.4 mV	+0.9 mV

Table 5.1: Energy difference between parallel and antiparallel spin configurations for the three kinds of molecules obtained by DFT simulations both in gas phase and on-surface.

The large magnetic coupling obtained by DFT for the free-molecular species are attributed to superexchange between the Fe *d*-orbitals located at each porphyrin core through the π -orbitals of the conjugated organic system. Superexchange interactions couple magnetic impurities indirectly via an intermediate non-magnetic bridge, which mediates high-order virtual hopping processes between the orbitals. The strength of superexchange interactions depend on both the electronic overlap between orbitals of bridge and magnetic centers, and on their relative energy alignment [63].

The π -aromatic backbone that links the two porphyrin cores represents such non-magnetic bridge that couple the two Fe magnetic atoms. Upon adsorption on the gold substrate, it is expected that interactions between the π -platform and the surface arise. One possibility to explain the disappearance of the superexchange interactions is such hybridization with the metallic Fermi sea, that open new hopping channels between the organic bridge and the electron bath of the surface, and quench those between the Fe atoms.

To investigate alternative scenarios for the origin of the quenching of intramolecular magnetic interacions, we computed the projected density of states (PDOS) of all three kinds of molecules. The most clear effect of the adsorption on the electronic configuration is the reorganization of the spin polarization among the Fe *d*-orbitals (see Fig. 5.4). In the gas phase, the three molecular species show spin-polarized d_{z^2} and d_π Fe orbitals contributing to the total spin $S = 1$. Upon adsorption on the gold surface, the total spin remains unchanged in every Fe ion, but hybridization with the substrate leads to the doubly-occupancy of the Fe d_{z^2} orbital, quenching its spin polarization. Conversely, the d_{xz} becomes singly-occupied and con-

tributes to the total spin. Such reorganization in the orbital distribution might lead to the disappearance of the superexchange interactions due to the different overlap of the Fe d -orbitals.

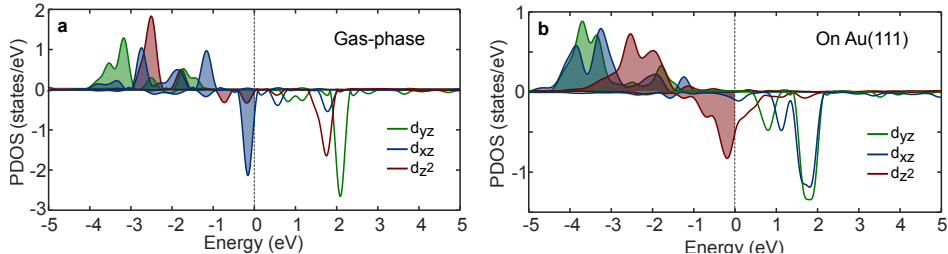


Figure 5.4: Density of states of 2-FeDPP projected on the d orbitals of one of the Fe atoms (PDOS) **a**, in gas phase and **b**, on Au(111).

5.3 Interpretation of the magnetic ground state of each independent Fe ion

We have attributed the inelastic steps observed in the dI/dV spectra of Fig. 5.3 to the excitation of the spin multiplet of the Fe ion in the presence of magnetic anisotropy imposed by its ligand field. The strength of the magnetic anisotropy energy (MAE) can be determined from the energy position of the inelastic steps by modelling with the phenomenological spin Hamiltonian [20, p. 15] $\hat{H}_s = D\hat{S}_z^2 + E(\hat{S}_x^2 - \hat{S}_y^2)$, where $\hat{S}_x, \hat{S}_y, \hat{S}_z$ are the three components of the spin operator, and D and E the axial and transverse anisotropy parameters, respectively. DFT simulations reveal that all three species maintain a $S = 1$, independently of the number of C-C bonds between the pyrrole groups, and that the spin is preserved upon adsorption on the Au(111) surface. Hence, we consider spin excitations among the $S_z = \pm 1, 0$ multiplet.

Single FeDPP molecules present an easy-plane anisotropy configuration confined to the molecular plane, as shown in Section 4. However, the double step featured by *twisted* molecules (at $V_S = \pm 0.9$ and ± 4.1 mV, indicated with shade areas in Fig. 5.3a) reveals the presence of transverse magnetic anisotropy E in an easy-axis configuration, as a consequence of the distortion of the molecular structure by the twisted pyrroles. Such narrow spin excitation remains in the twisted side of the *half-fused* molecules. In these species, a wider, single-step arises on the second Fe site (Fig. 5.3b), leading to an axial anisotropy parameter $D=+7.4$ meV. This value is similar to the axial MAE measured on single Fe porphyrin molecules on Au(111) sur-

faces [65–67]. We note that in the gas phase structure of *half-fused* species both Fe ions are surrounded by identical ligand field. Hence, the different splitting of the spin multiplet on the adsorbed case indicates that one of the two porphyrin cores lies planar on the surface, increasing the axial anisotropy to values close to the single FeTPP case, while the other remains with a twisted pyrrole, and behaves similarly to the double twisted species. This configuration is confirmed by the three-dimensional relaxed structures simulated by DFT and shown in Fig.5.5, where *half-fused* molecules present one porphyrin core planar (Fig.5.5, left) and a twisted one (Fig.5.5, right).

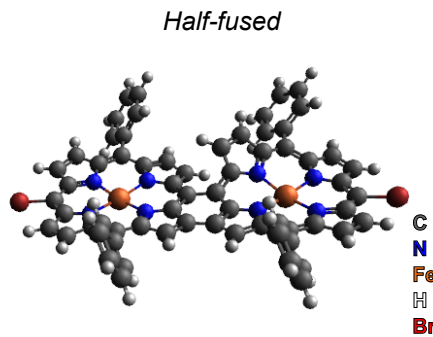


Figure 5.5: On-surface three-dimensional relaxed structure of *half-fused* 2-FeDPP molecule as obtained by DFT. The gold substrate has been removed for clarity.

5.3.1 Entering the mixed-valence regime

An intriguing observation is the rather faint and quite asymmetric spectral features of the *fused* molecules, in clear contrast with the sharp steps usually observed in these systems. As shown in the spectral map of Fig. 5.3f, the signal appears localized over the Fe ions, where a characteristic spectral onset is visible at $V_S = \pm 5$ mV (arrow in Fig. 5.3f), and vanishes in between the iron sites. In spite of the faint lineshape, the characteristic width of ± 5 mV and its spatial localization over each Fe site indicate that it can be attributed to the spin polarization of the magnetic centers.

As we showed in Section 4, asymmetric components in inelastic spectra are attributed to higher order scattering processes when a spin system is out of the particle-hole symmetry point [19, 65, 68]. In that scenario, potential scattering becomes relevant, introducing charge scattering processes that do not flip the spin but affect the spectral lineshape of the the inelastic excitation. To correlate this faint spectral features with the alignment of the energy level hosting the spin, we performed longer-range STS over the

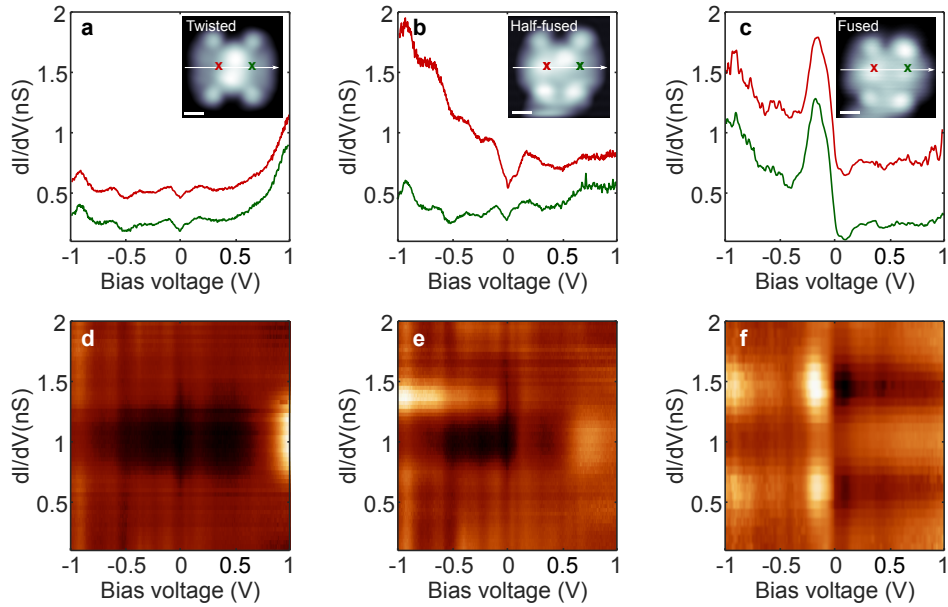


Figure 5.6: a, b, c, Long-range dI/dV spectra measured at the Fe positions in *twisted*, *half-fused* and *fused* molecules as indicated in the inset, respectively. d, e, f, Stacked-plot of dI/dV spectra measured along each molecule ($V_S = 1$ V, $I = 500$ pA).

Fe sites (see Fig. 5.6a, b, c). We found that *fused* molecules show an intense electronic resonance centred at $V_S = -200$ mV with strong presence at the Fermi level (see Fig. 5.6c). The resonance reproduces the spatial pattern found for the low-energy spectra shown in Fig. 5.3f, spatially localized over the Fe sites as shown in Fig. 5.6f. Such strong resonance close to E_F is absent on both *half-fused* and *twisted* molecules, which instead show smoother spectral patterns (see Fig. 5.6d, e).

The peculiar resonance structure overlapping with the Fermi level of *fused* 2-FeDPP molecules suggest that the system is close to the mixed-valence regime. In the extreme case of a spin-polarized orbital lying at the Fermi level, strong charge fluctuations are predicted to fade out the sharp spin excitation onset and renormalize the spectral lineshape [68]. Indeed, that behaviour is observed in *fused* molecules, where the faint onsets at $V_S = \pm 5$ mV are reminiscent of the inelastic spin excitation.

We thus propose here that the interaction between the porphyrin cores through the π -conjugated system renormalizes the electronic structure, driving the system towards the mixed-valence regime as inferred from the long-range dI/dV spectra shown in Fig. 5.6.

5.4 Conclusions

We have shown the iron metalation of newly synthesized double porphyrins. The three-dimensional structures react intramolecularly upon surface adsorption and high-temperature annealing, leading to the partial (*half-fused*) or total (*fused*) planarization of the organic structures. Such structural changes result in three molecular conformations with distinct magnetic properties. All three *twisted*, *half-fused* and *fused* species present a $S = 1$ on each Fe site. Surprisingly, surface adsorption quenched the superexchange magnetic coupling between the Fe atoms in all three cases, presumably due to the hybridization of the organic π -backbone with the Fermi sea of the substrate. Therefore, each Fe site depicted an independent magnetic ground state, governed by the porphyrin core conformation and the coupling of the Fe d -orbitals to the Au(111) substrate. Such interaction drive *fused* molecules towards the mixed-valence regime, leading to the observed asymmetric lineshape of the spin excitation.

Part II

Local distortions of Superconductivity

Chapter 6

Effects of magnetic impurities and weak disorder on superconductivity

Three years after the liquefaction of helium, superconductivity was discovered in 1911 by Heike Kamerlingh Onnes [69] in Leiden. He observed the disappearance of the electrical resistance as the temperature was lowered below a critical value T_c characteristic of each material. Together with the critical temperature, superconductors are characterized by a critical magnetic field H_c , above which superconductivity is quenched [70]. It was not until 1954 that Corak *et al.* [71,72] established the existence of an energy gap Δ ($\sim k_B T_c$) from the measurements of the specific heat of superconductors.

The microscopic description of superconductivity by Bardeen, Cooper and Schrieffer (BCS) [73] showed that a weak attractive force caused by electron-phonon interactions causes an instability of the Fermi sea ground state of the electron gas with respect to the formation of bound pairs of electrons (Cooper pairs), occupying states with equal energy and opposite momentum and spin [74]. BCS theory predicted that a minimum energy of $E_g(T = 0) \approx 3.5k_B T_c$ is required to break a Cooper pair and create two quasi-particle excitations.

A different approach towards the understanding of superconductivity was carried out by Ginzburg and Landau (GL) [75] in 1950. GL theory introduced the concept of a complex pseudowavefunction ψ as an order parameter describing superconducting electrons, where $n_s = |\psi(r)|^2$ is the local density. In 1959, Gor'kov [76] brought both approaches together and showed that the GL theory was a limiting form of BCS theory, valid near T_c and in which $\psi \propto \Delta$. Thus, ψ can be conceived as the wavefunction of the Cooper pairs.

Hence, superconductors are characterized by a many-body condensate of Cooper pairs with wavefunction $\psi(r) = |\psi(r)| e^{i\varphi(r)}$, whose phase is maintained over macroscopic distances. Since particle number N and phase φ are conjugate variables, there is an uncertainty relation limiting the precision with which they can be simultaneously known:

$$\Delta N \Delta \varphi \gtrsim 1 \quad (6.1)$$

The physical meaning of the superconducting phase was first described by Josephson [77], who predicted the tunneling of Cooper pairs through a superconductor-insulator-superconductor junction even at zero bias voltage, giving rise to the so-called Josephson current

$$I_s = I_c \sin(\varphi_1 - \varphi_2) = I_c \sin(\Delta\varphi) \quad (6.2)$$

where I_c is the maximum critical current that the junction can support and φ_1 and φ_2 are the phases of each superconductor. If a voltage difference V is applied across the junction, the phase difference evolves such as

$$\frac{d(\Delta\varphi)}{dt} = 2 \cdot e \cdot V / \hbar \quad (6.3)$$

Therefore, an alternating current of amplitude I_c and frequency $2eV/\hbar$ will flow across the junction. Given Equations 6.2 and 6.3, the coupling free energy stored in the junction can be obtained by integrating the electrical work done by the current source in changing the phase [74]

$$F = \int I_s V dt = \int I_s (\hbar/2e) d(\Delta\varphi) = \int I_c \sin(\Delta\varphi) (\hbar/2e) d\Delta\varphi \quad (6.4)$$

$$F = \text{constant} - \frac{\hbar I_c}{2e} \cos(\Delta\varphi)$$

From Equation 6.4, one can see that the energy is minimum when the two phases are equal, so that $\Delta\varphi = 0$. Consequently, the current flowing through the junction is $I_s = 0$. Therefore, the Josephson current is a measure of the coupling between the phases of the two superconducting electrodes.

There are two length scales that govern the superconducting state: penetration depth and coherence length. The penetration depth λ describes the distance that a magnetic field penetrates into a superconductor, since magnetic fields are expelled from the interior of the superconductor due to the Meissner effect [70]. The coherence length ξ characterizes the real-space distance over which $\psi(r)$ can vary without an energy increase.

6.1 Superconductivity in the STM

The tunneling regime in the STM provides a natural insulator barrier that can be used to study metal-insulator-superconductor junctions [?]. The differential conductance dI/dV probes the energy gap of the superconductor and exhibits quasiparticle resonances at $V_s = \pm\Delta$, which limit the superconducting gap.

However, finite temperatures introduce thermal broadening at the Fermi level of the metallic tip, which limit the energy resolution. Therefore, to study the superconductor characteristics in the μeV energy range, we coated the tip with superconducting material [?, ?, ?, 13]. Such superconductor-insulator-superconductor junction gives rise to the quasiparticle spectrum shown in Fig. 6.1a, where the width of the superconducting gap corresponds to 4Δ . Since we used a Pb(111) substrate and a Pb-covered tip, the quasiparticle peaks are expected at $V_S \approx \pm 2.7 \text{ meV}$ [78].

Close inspection of the quasiparticle excitation spectrum in Fig. 6.1a reveals split coherence peaks at $V_S \approx \pm 2.7 \text{ mV}$. They correspond to two superconducting gaps separated by $V_S = 150 \mu\text{eV}$ [78]. It has been shown that the lead Fermi surface is composed by two Fermi sheets, an isotropic one with $s-p$ character and a tubular one with $p-d$ character [79] (see Fig. 6.1b,c). Since each provides a different pairing energy for the Cooper pairs due to different electron-phonon coupling [80], two peaks arise in the dI/dV spectrum.

For comparison, we show in Fig. 6.1d the dI/dV spectrum obtained with a lead-terminated tip on a $\sim 100 \text{ nm}$ Pb film grown on Graphene/SiC. While the coherence peaks appear at $V_S \approx \pm 2.7 \text{ mV}$ as in the Pb(111) crystal, their splitting is missing. We attribute this to the small film thickness compared to the Pb coherence length scale [81], which washes out the anisotropy of the Fermi surface [82].

When decreasing the distance between the superconducting tip and sample, subgap peaks emerge as a consequence of the coupling between the electrodes. In Fig. 6.2 we show a dI/dV spectrum obtained on a Pb(111) surface with a lead-covered tip at closer tip-sample distances as the ones shown in Fig. 6.1. First, a peak at zero bias appears due to the Josephson effect [77], as described in Section 6, revealing the coupling of the phases of the two superconductors through the vacuum barrier. Furthermore, two peaks appear at the energy values of $\pm\Delta$ and correspond to the first Andreev reflection [83, 84]. They are predicted to occur at the energies $\pm(\Delta_{tip} + \Delta_{sample})/m$, with $m = 2, 3, 4, \dots$ [85–87]. As sketched in Fig. 6.2b, at $eV = \Delta$, a hole tunnels from the right SC into the left SC and is reflected back as an electron, annihilating a Cooper pair in the left superconductor that is transmitted to the right superconductor.

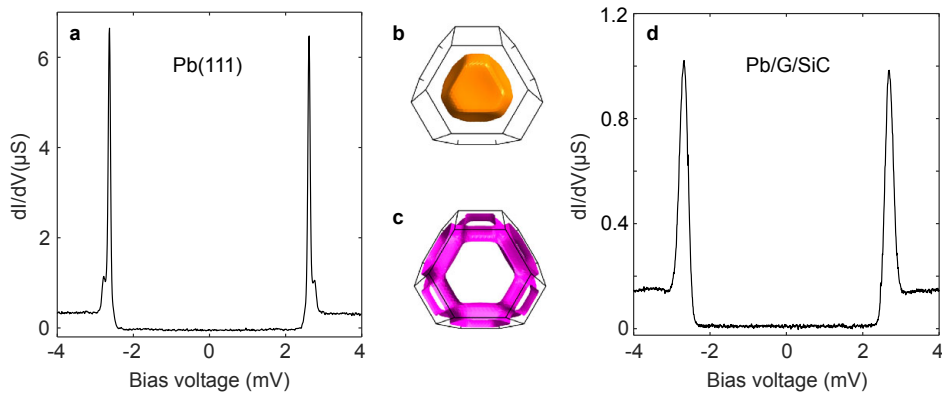


Figure 6.1: a, dI/dV spectrum obtained on a Pb(111) crystal with a lead-terminated tip ($V_S = 4$ mV, $I = 100$ pA, $V_{rms} = 10$ μV). b, c, Isotropic and tubular Fermi surfaces of Pb(111) extracted from [?, 78], respectively. d, dI/dV spectrum obtained on a Pb film of ~ 100 nm with a lead-terminated tip. ($V_S = 5$ mV, $I = 100$ pA, $V_{rms} = 25$ μV)

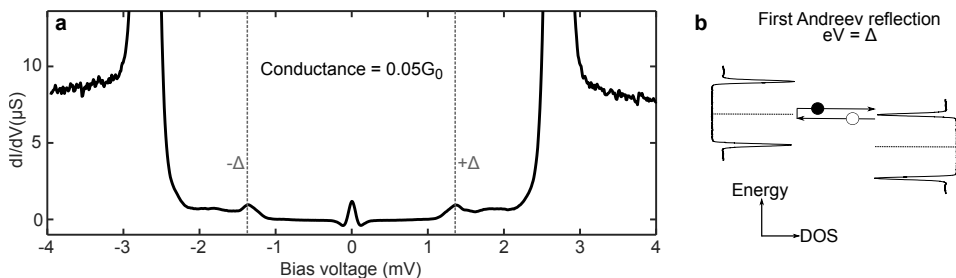


Figure 6.2: a, dI/dV spectrum obtained on a Pb(111) crystal with a lead-terminated tip at a closer distance than in Fig. 6.1. The value of the superconducting gap $\pm\Delta$ is indicated as well as the conductance at the tip-sample separation set for the measurement. ($V_S = 4$ mV, $I = 14$ nA, $V_{rms} = 10$ μV) b, Sketch of the first Andreev reflection at $eV = \Delta$ in a symmetric SC-insulator-SC junction.

6.2 Deviations from the clean limit: magnetic impurities and weak disorder

In the previous section, we depicted a general picture of the characteristics of clean, three-dimensional superconductors. Nevertheless, the deviations from such clean limit may reveal new phases of superconductivity. In the next sections we will explore the distortions of the superconducting state by two different approaches: the insertion of magnetic impurities and the reduction of the material's dimension from 3D to 2D.

6.2.1 Magnetic impurities as point scatterers

A dilute amount of magnetic impurities placed on a superconductor create a potential that locally distorts the Cooper pairs bath. The magnetic moment of the impurities couples to the Cooper pairs' with a coupling strength J , creating a bound state. The coupling between the spin and the coherent superconducting state can be probed through the excitation of such Yu-Shiba-Rusinov (Shiba) bound states [9–11]. They appear as pairs of sharp, energy-symmetric resonances within the superconducting gap Δ as shown in Fig. 6.3a. The energy of such bound state has been shown to be [9–11, 88]

$$\epsilon = \Delta \frac{1 - (JS\pi\rho_s)^2}{1 + (JS\pi\rho_s)^2} \quad (6.5)$$

where ρ_s is the DOS at the Fermi level in the normal state.

In the simplest case of a $S = 1/2$ impurity, a single Shiba state arises at energy ϵ . Nevertheless, as soon as the magnetic moment $S > 1/2$, several Shiba resonances might emerge. Two scenarios have been discussed as the origin of multiple Shiba states: either each spin-polarized d -orbital acts as an independent point scatterer, or the splitting of the S_z components by the presence of magnetocrystalline anisotropy at the impurity gives rise to the low-energy excitations [12, 89–96].

The interaction between magnetic impurities and superconductors was first described [10] within a classical picture: a local point magnetic field. However, such simplified model fails to describe the many-body effects that arise due to the quantum nature of an atomic spin. Later works properly depicted the competition between the superconducting correlations and the screening of the impurity magnetic moment by the Kondo effect in a quantum spin [?]. The ratio between the coupling strength $k_B T_K$ to the bath and the Cooper pairs' order parameter Δ drives the system across a quantum phase transition (QPT) between two regimes: the free spin ($k_B T_K \ll \Delta$) and the Kondo-screened regime ($k_B T_K \gg \Delta$) [13, 97–99]. As sketched in Fig. 6.3b, when $k_B T_K \ll \Delta$, the magnetic impurity ground state remains as

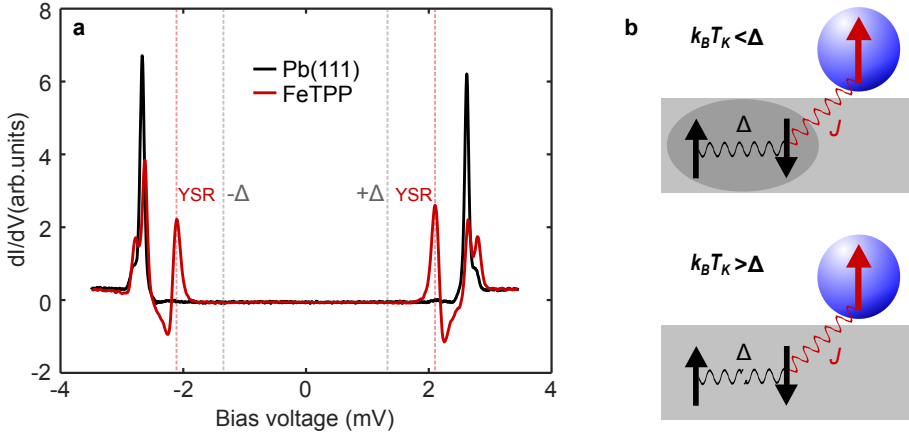


Figure 6.3: a, dI/dV spectrum obtained on the clean Pb(111) surface (black) and on the magnetic porphyrin (red), the latter showing Shiba states (YSR) within the superconducting gap. b, Sketch of the two regimes that define the ratio between the coupling to the substrate $k_B T_K$ and the superconducting gap Δ : free-spin ($k_B T_K \ll \Delta$) and Kondo-screened ($k_B T_K \gg \Delta$).

a free-spin of S value, locally distorting the Cooper pairs' bath. Conversely, when $k_B T_K \gg \Delta$, a Cooper pair breaks and couples antiferromagnetically to the magnetic moment, leading to a ground state $S = S - 1/2$. This QPT is characterized as the crossing of the Shiba resonance through the Fermi level as the system approaches $k_B T_K = 0.3\Delta$ in a single-channel configuration.

While the strength of the exchange coupling J between the magnetic impurity and the superconducting substrate is reflected in the energy position of the Shiba state ϵ , the different intensity of the Shiba resonances at positive and negative energy is caused by broken particle-hole symmetry by a finite potential scattering term \mathcal{U} , [18,19] and reflects the electron and hole amplitudes of the Bogoliubov quasiparticle u and v , respectively [?, 100]. Following the notation in [95]:

$$u^2, v^2 = \frac{2\alpha\pi\rho_s\Delta(1 + (\alpha \pm \beta)^2)}{((1 - \alpha^2 + \beta^2)^2 + 4\alpha^2)^{3/2}} \quad (6.6)$$

where ρ_s is the Density of States in the normal state, $\alpha = \pi\rho_s JS$ and $\beta = \pi\rho_s \mathcal{U}$ (note that \mathcal{U} is the potential scattering amplitude described in Section 2).

At the quantum phase transition, $k_B T_K \gg \Delta$, the crossing of the electron and hole amplitudes of the Bogoliubov quasiparticle through the Fermi energy is accompanied by a reversal in the intensity of the resonances

at positive and negative bias voltage. Therefore, once the sign of \mathcal{U} is determined, one can deduce from the symmetry of the Shiba states the regime at which the magnetic impurity is, in terms of free-spin or Kondo-screened [13,93,98,101]. Electron (hole) components of the Bogoliubov quasiparticle will appear at positive energies in the free-spin (Kondo-screened) case.

The physical origin of the multiple Shiba states can be deduced from their spatial distribution. Independent spin-polarized impurity orbitals hybridize differently with the superconductor. Therefore, the spatial map of each Shiba excitation depict a distinct real-space distribution that reflects the symmetry of each spin-polarized orbital [?, 96].

An alternative scenario involves the presence of magnetocrystalline anisotropy, in which each Shiba resonance corresponds to one component of the multiplet $m_S = \pm S$. Previous works [89] showed that, a spin $S = 1$ system in the presence of magnetic anisotropy, the split Shiba peaks intensity describe a Boltzmann distribution in a free-spin situation ($k_B T_K \ll \Delta$) or equal areas in a Kondo-screened ground state ($k_B T_K \gg \Delta$) [13, 93, 98, 101].

A more realistic picture relies on the low-symmetry adsorption that magnetic impurities usually experience on a surface. In a spin $S = 1$, two exchange channels might arise. In the absence of magnetic anisotropy, the ground state is $S = 1 - 1/2 = 1/2$, and two Shiba resonances appear as in-gap states: one excitation to $S = 1$ and a second one to $S = 0$. In such multichannel configuration, one exchange constant dominates, and therefore gives rise to a more intense Shiba state as compared to the second channel.

6.2.2 Two-dimensional superconductivity in the presence of weak disorder

According to the Anderson theorem [?], the characteristics of a superconductor are not affected by the presence of nonmagnetic impurities. However, Bogoliubov-de Gennes theory of superconductivity [?] showed that, under the presence of weak disorder, spatial fluctuations of the order parameter are expected. In the limit of strong disorder, quantum interference of non-interacting electrons induces their spatial localization, which leads the material to an insulating state through the so-called Anderson transition [102]. In the vicinity of the transition preceding localization, these systems display eigenstates being neither extended nor localized (see sketch in Fig. 6.4) that show strong fluctuations of their amplitudes at all length scales. Such near-critical eigenstates exhibit multifractal character, i.e., they are formed by interwoven sets of different fractals, each characterized by its own non-integer dimension [103–105]. These critical eigenstates and their correlations are of fundamental relevance for the functionality of materials

in the presence of disorder since the multifractal regime dominates their electronic, transport and magnetic properties [?, ?, 106, 107].

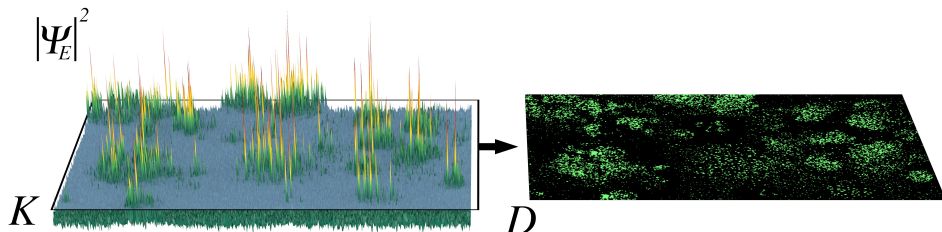


Figure 6.4: Schematic representation of 2D multifractality. The left panel shows a cartoon of the amplitude squared of a 2D wavefunction $|\Psi|^2$ in the multifractal regime. The broad distribution of peaks and valleys is a typical feature of multifractality. The right panel depicts the points for which the amplitude is larger than a given cut-off K . The amplitude is said to be multifractal only if the fractal dimension of the resulting points does depend on the cutoff value.

In the strong disorder regime beyond the critical value, Anderson localization disables long-range quantum coherence, thus quenching superconductivity in the material. For weak disorder, superconductivity has been shown to be remarkably robust [108, 109], persisting even in polycrystalline or amorphous materials near the Anderson localization transition [110]. Nonetheless, even weak disorder strongly affects the superconducting state. For example, recent experimental studies have shown that disorder leads to spatial inhomogeneity [109, 111, 112] and emergent granularity [113] in the superconducting order parameter. Even though these findings demonstrate the intricate interplay between disorder and superconductivity, the mere existence of the superconducting state in the multifractal regime remains unexplored, and the hypothetical signatures of multifractality on its fundamental properties have been mostly theoretically addressed so far [114–117]. Such investigation seems particularly suitable in 2D materials since, unlike in 3D materials where multifractality only arises in a narrow range of disorder near the critical point, multifractality is expected to emerge in 2D for a broad range of weak disorder strengths, which facilitates its experimental observation [84, 117].

2D is the marginal dimension for both localization and superconductivity. The scaling theory predicts that in an infinite 2D system all electronic

eigenstates are localized regardless of the disorder strength [?]. That would give rise to an insulating phase, thus precluding the development of the superconducting state. However, this is only valid for infinite 2D systems with time reversal symmetry. 2D systems with strong spin-orbit coupling and finite size may exhibit a metallic ground state for sufficiently weak disorder compatible with both the multifractal regime and superconductivity. 2D materials develop multifractality provided the size of the material is smaller than the localization length ξ , which can be extremely large in the weak disorder regime (it scales exponentially with the inverse of the disorder strength, i.e. $\xi \propto l \cdot \exp(\pi k l / 2)$, where k is the wavevector and l is the mean-free path).

6.3 Outline of Part II

In Section 7 we investigate iron porphyrin molecules on the Pb(111) superconductor. We show that FeTPP magnetic impurities present at least two pairs of Shiba bound states with distinct spatial distribution for the electron and hole components. We found that the FeTPP molecules lie in a Kondo-screened ground state, as extracted from the magnetic field and temperature responses of the Kondo resonance in the metallic state. The presence of multiple Shiba states combined with the Kondo resonance found in the metallic state situate FeTPP molecules in an underscreened Kondo scenario, with a total spin $S = 1$ partially screened by the bath of the substrate.

In Section 8, we will show the emergence of spatial fluctuations in a two-dimensional superconducting TMD material, single-layer NbSe₂, due to the presence of weak disorder. The spatial distribution of the superconducting gap width indicates that superconductivity is governed by the two-dimensional multifractal regime.

Chapter 7

Multiple Shiba bound states in the underscreened Kondo regime

A magnetic impurity placed on a superconductor locally distorts the Cooper pairs bath. As shown in Section 6, the coupling between the spin and the coherent superconducting state can be probed through the excitation of Shiba bound states [9–11].

In this Section we show that magnetic porphyrins on the Pb(111) superconductor create a Moiré pattern composed by alternating segments of decoupled and strongly coupled molecules. The latter present an integer spin $S = 1$ underscreened by the bath with one of the channels strongly coupled, leading to a Kondo-screened ground state. We found that the spatial distribution of the Shiba peaks at positive and negative energy correlates with different Kondo lineshapes in the metallic state. In contrast, decoupled FeTPP molecules show signatures of magnetic anisotropy that can be locally manipulated by both the adsorption site and the tip-molecule distance.

7.1 The Moiré molecular superstructure

Deposition of chlorine Fe-tetraphenyl porphyrin molecules results in their arrangement in close-packed islands as shown in Fig. 7.1a. The molecules lose the chlorine radical upon surface adsorption [37] leading to dechlorinated FeTPP, which preserve a $S = 1$ on the surface [65]. The organic phenyl ligands convey flexibility to the prophine core, acquiring a saddle-shape conformation that leads to two pairs of nonequivalent pyrroles. The Pb(111) surface accommodates an incommensurate square molecular lattice, performing a Moiré superstructure [13, 89, 89] visible in Fig. 7.1a as

segments of the two kinds of molecules. In Fig. 7.1b-c we show a zoom in the two types of FeTPP that conform such Moiré pattern, which at low biases show a dark/bright centers, respectively. In the following, we will refer to the two different kinds as dark and bright molecules, respectively. The differences between the two species rely not only on their topography, but also on their electronic and magnetic characteristics.

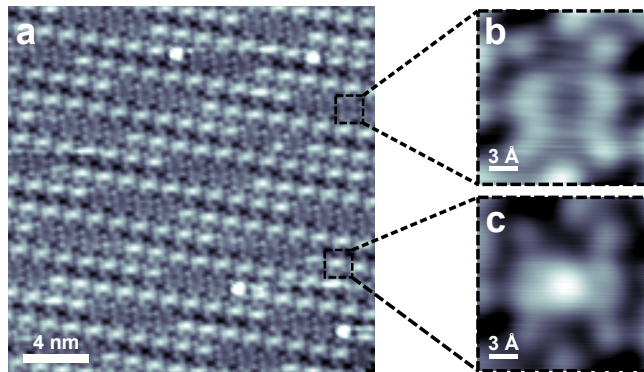


Figure 7.1: **a**, STM topography of a large island of FeTPP molecules showing the Moiré pattern. **b, c**, Constant-current STM topographs of single dark and bright molecules, respectively. ($V_S = 45$ mV, $I = 100$ pA).

Constant-height conductance maps obtained in bright and dark molecules show that the occupied and unoccupied frontier orbitals are spatially localized along one symmetry axis for both types of FeTPP molecules, presumably due to the saddle-shape conformation (see Fig. 7.2). Bright molecules present an extended occupied orbital along their symmetry axis, which is absent in the dark molecules. Conversely, dark molecules show an empty orbital at $V_S = +100$ mV spatially localized on both Fe and pyrrole sites. Long-range dI/dV spectra obtained on Fe and pyrrole sites reveal a broad state below the Fermi level in bright molecules, while the dark ones do not show strong features close to zero bias voltage (see Fig. 7.2e,f, respectively).

In order to understand the interaction between the magnetic molecules and the superconductor underneath, we show short-range dI/dV spectroscopy obtained on both dark and bright molecules in Fig. 7.3a,b, respectively. We used a superconducting lead-terminated tip to enhance the energy resolution beyond the thermal limit [?, ?, ?, 13]. In addition to the two coherence peaks of the Pb(111) surface observed at $V_S \approx 2.7$ mV [78], we observed in-gap states that we attribute to the excitation of Shiba bound states [?, ?, 9–11]. Even though both bright and dark molecules show in-gap states, the ones found on the dark molecules are rather faint. Bright FeTPP molecules show multiple Shiba resonances, whose number depends on their position within

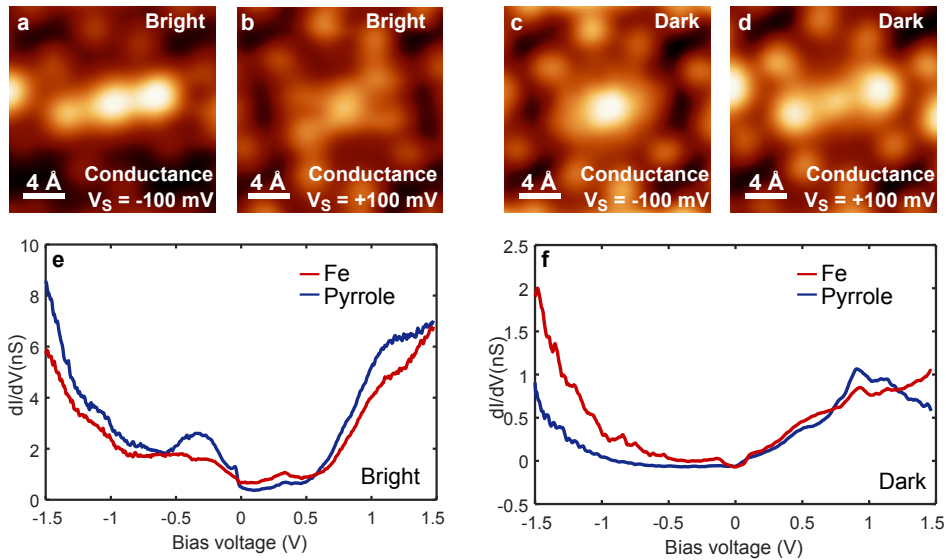


Figure 7.2: a-d, Constant height conductance maps of bright and dark molecules at $V_S = -100$ and $+100$ mV ($I = 200$ pA). e, f, Long-range dI/dV of bright and dark molecules, respectively ($V_S = 1.5$ V, $I = 3$ nA, $V_{rms} = 2$ mV).

the Moiré pattern. In Fig. 7.3c we show a stacked plot of dI/dV spectra each obtained on the center of 30 bright and dark molecules aligned along a row of the Moiré lattice. For both kinds, at the frontier between dark/bright molecules, the Shiba resonances generally appear closer to the coherence peaks. We found that such variations are much smaller than those reported in previous works [13], which were attributed to slight variations in the adsorption site of each molecule. In Section 7.1.1 we will focus on the origin of the multiple Shiba states, their spatial distribution and their coupling to the substrate on the bright molecules. Moreover, we will show the correlation between the Shiba bound states and the Kondo effect in the normal state. Finally, in Section 7.1.2 we will show the effect of magnetocrystalline anisotropy and its manipulation with the tip-sample separation in dark molecules.

7.1.1 Dark and bright FeTPP: two states of the same molecule

We found that bright molecules located at the end of the Moiré segment could be switched into the dark kind upon reduction of the tip-sample distance. In Fig. 7.4b we show the dI/dV spectra obtained on a bright

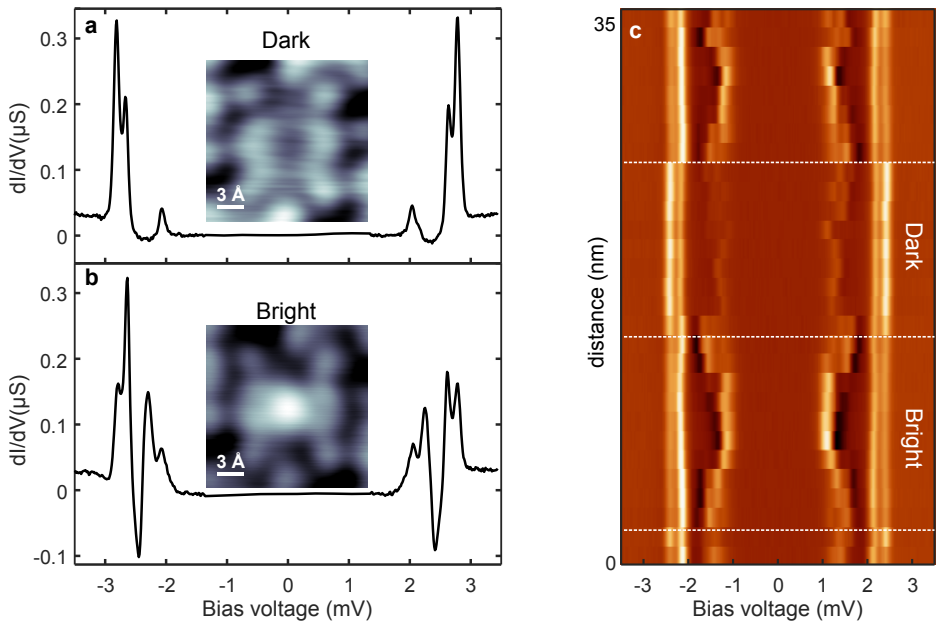


Figure 7.3: **a, b,** dI/dV spectra of dark and bright molecules showing Shiba states. **c** Stacked plot of point dI/dV spectra obtained along a single line of bright and dark molecules ($V_S = 3.5$ mV, $I = 100$ pA, $V_{rms} = 10$ μ V).

molecule at several tip-sample distances. As the tip-sample distance is decreased down to $\Delta z = -180$ pm, the STS lineshape drastically changes to the one found in dark molecules (see Fig. 7.4b). Close inspection of the in-gap states present in the bright and dark molecules in Fig. 7.4c show a mismatch in their energy position. We attribute it to the distinct coupling to the lead substrate driven by the distortion of the molecular conformation by the STM tip. Switching between bright/dark states was only possible in molecules at the border between the two kinds, while those at the center of the Moiré presented the characteristic bright dI/dV spectrum independently of the tip-sample distance.

The 150 μ eV splitting of the Pb(111) coherence peaks around $V_S \approx 2.7$ meV has been attributed to two different Fermi surfaces with distinct electron-phonon coupling strengths [78–80] (see Section 6). Furthermore, Ruby *et al.* [78] showed that the crystalline orientation of the lead substrate strongly determines the intensity of each of the two split coherence peaks. We show in Fig. 7.4 that dI/dV spectra obtained on dark molecules show an inversion in the intensity of the coherence peaks as compared to the bare Pb(111) surface (see Fig. 7.4a). This has been previously observed in non-magnetic adatoms, and attributed to the preferential hybridization of

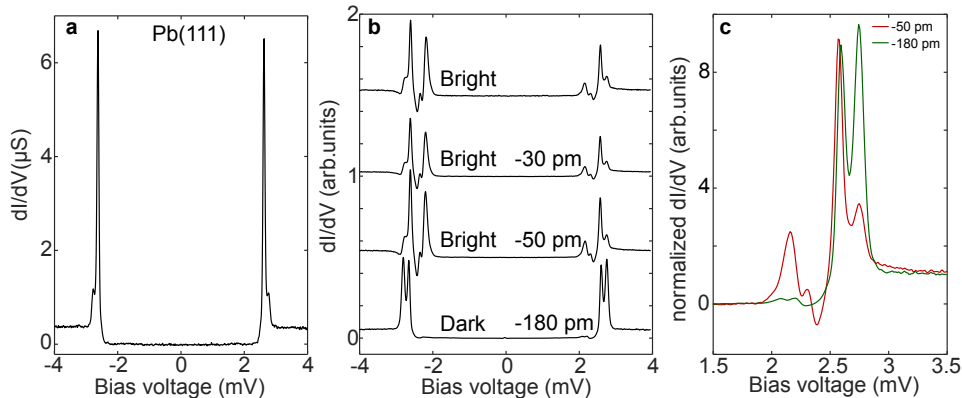


Figure 7.4: a, dI/dV spectrum obtained on a $Pb(111)$ crystal with a lead-terminated tip. ($V_S = 4$ mV, $I = 100$ pA, $V_{rms} = 10$ μV). b, Evolution from bright to dark-type of FeTPP molecule as the tip-sample distance is decreased. c, Zoom-in a showing the discrepancy in the energy values of the Shiba resonances in the bright and the dark state ($V_S = 4$ mV, $I = 100$ pA, $V_{rms} = 10$ μV).

the adatoms' localized d -states with the $p - d$ -derived lead Fermi surface, instead of with the $s - p$ band, what, therefore, increases its tunneling probability (see Fig. 6.1b,c).

Multiple Shiba bound states

We will now focus on the bright FeTPP molecules, which present strong Shiba states and show a continuous distribution of their energy position within the bias range of ± 2.0 to ± 2.3 mV, as shown in Fig. 7.5. The first and last molecules forming a bright segment usually show two/three Shiba resonances. As we go deeper inside the bright Moiré segment, a more intense peak closer to zero bias voltage emerges, as well as a faint peak in the negative differential conductance energy region. We attribute the variation of peak's position and intensity to the incommensurate lattice of the molecular islands over the lead atomic lattice. Every molecule lies on a slightly different adsorption site, causing variations in the overlap of the Fe d -orbitals with the superconductor, resulting in small variations in the magnetic exchange J between the molecular spin and the substrate Cooper pairs. Therefore, small differences in the coupling strength J give rise to variations in the energy position of the Shiba resonances.

The presence of sharp resonances in an absolute gap produces negative values for the conductance. These regions obscure the real value and intensity of the Shiba bound states. In order to remove the effect of the

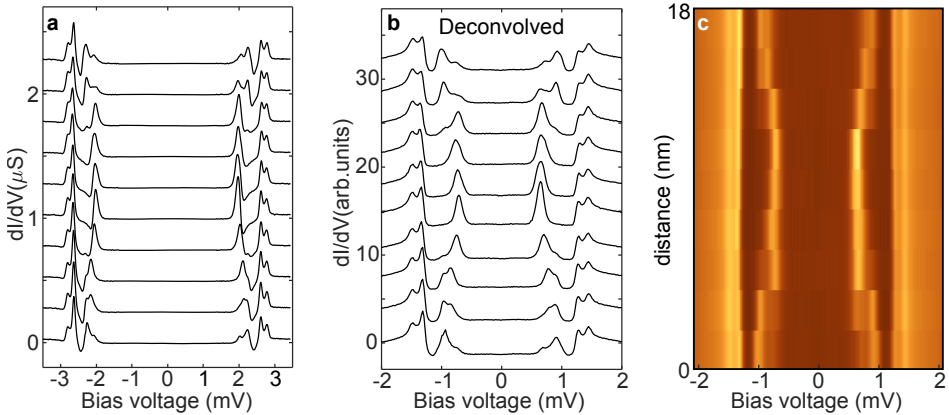


Figure 7.5: **a**, dI/dV spectra obtained on several bright molecules along a Moiré line. **b**, Deconvolved dI/dV spectra from **a**. **c**, Stacked plot of the single dI/dV spectra showed in **b** ($V_S = 3.5$ mV, $I = 100$ pA, $V_{rms} = 10$ μ V).

negative differential conductance and extract the intensity and peak areas of the Shiba resonances, we deconvolved the dI/dV spectra following the method shown in [?, 96], where the tip density of states is modeled as a BCS gap. The deconvolution procedure is then reduced to the calculation of the inverse of a convolution matrix. We deconvolved the dI/dV spectra of several bright FeTPP molecules that were contiguous to each other (Fig. 7.5b). Bright molecules usually show two in-gap peaks that differ in their intensity. Depending on the molecule, their energy position and intensity slightly change rather continuously. In Fig. 7.5c we show a stacked plot of dI/dV spectra obtained on each molecule along a bright segment. One can see that the most prominent Shiba peak moves towards the Fermi level as we approach the center of the segment, whereas at the edge multiple peaks closer to the coherent peaks are visible.

Distinct particle and hole spatial distributions of the Shiba states

As shown in Section 6, multiple Shiba states can have several origins. One scenario pictures independent spin-polarized d -orbitals that act as point scatterers, each of them giving rise to a Shiba bound state. Alternatively, previous studies on similar systems found that the presence of magneto-cystalline anisotropy at the impurity leads to the splitting of the Shiba resonances [12, 89–96]. In order to unveil the origin of the multiple Shiba peaks in FeTPP molecules, we probed their spatial distribution within the single FeTPP molecule. In Section 4 we showed that the very same FeTPP

molecules, deposited on a metallic substrate, present a spin $S = 1$ distributed along the molecule, which can be excited through two spatially-separated paths that represent the two spin-polarized orbitals that host the magnetic moment. In this Section we will probe how such orbital picture is modified in a superconducting substrate.

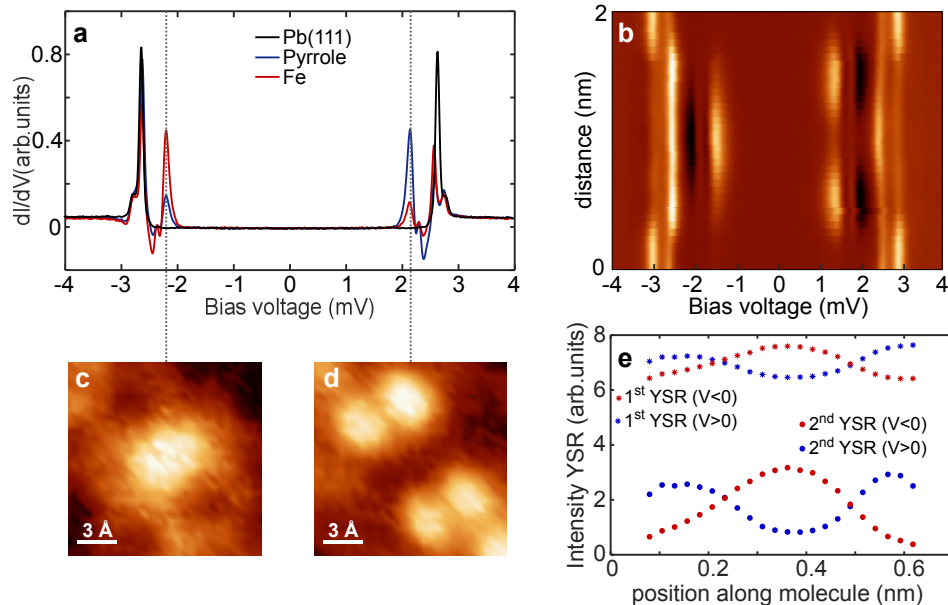


Figure 7.6: a, dI/dV spectroscopy obtained on the pyrrole (blue) and iron (red) sites of a FeTPP molecule. The Pb(111) STS is shown in black as a reference. b, Stacking plot of point dI/dV along the FeTPP molecule. c, d, Conductance maps at the energy of the hole and electron components of the Shiba states, respectively. e, Evolution of the intensity of each Shiba peak along a single FeTPP molecule. ($V_S = 4$ mV, $I = 100$ pA, $V_{rms} = 10$ μ V).

The saddle shape conformation of FeTPP results in two pairs of non-equivalent pyrroles [65], as shown in Section 4. Spectra obtained on both sites, pyrrole and Fe centers, show Shiba peaks at the same energy position. However, the amplitude of the particle and hole Shiba resonances differs with the intramolecular site. Figure 7.6b shows a spectral map of the sub-gap features measured along a line crossing the center of the FeTPP. The characteristic asymmetry in peak height with the bias polarity is inverted along the molecule. Over the Fe atom, Shiba peaks present larger intensity at $V_S < 0$, while over the two pyrroles the resonances are more intense at $V_S > 0$. Furthermore, dI/dV maps at the energy position of the most

intense Shiba resonances show such distribution in two dimensions (Fig. 7.6c and d, for negative and positive energies, respectively). The Shiba intensity at $V > 0$ shows a more complex structure composed by four lobes, a nodal line along the molecular axis, and low signal over the center.

In Fig. 7.6e we show that, at each polarity, both peaks' intensity follow the same spatial distribution, suggesting that they do not arise due to independent d channels, since in that case each peak should recover the renormalized spatial distribution of its corresponding orbital [12, 91, 92, 96].

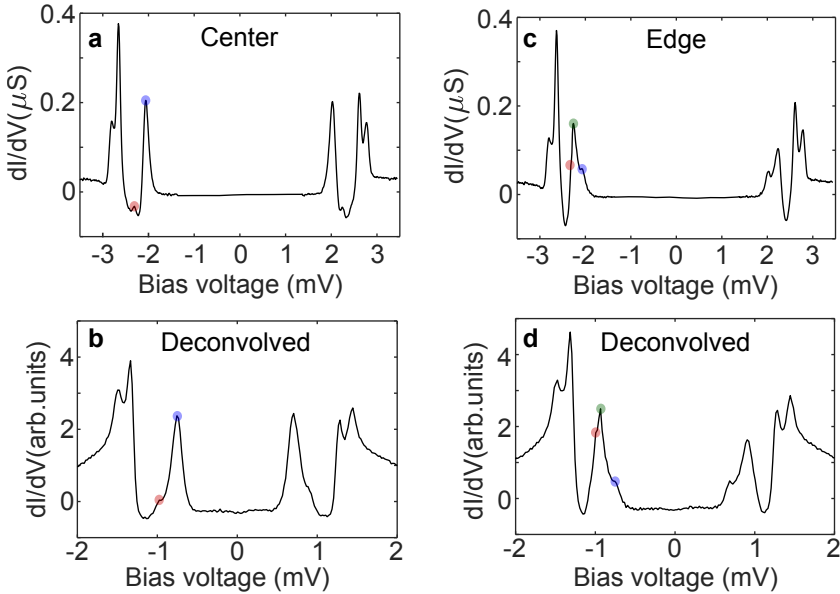


Figure 7.7: **a**, Characteristic dI/dV spectrum obtained at the center of a segment of bright molecules. **b**, Deconvolved spectrum of a. **c**, Characteristic dI/dV spectrum obtained at the edge of a segment of bright molecules. **d**, Deconvolved spectrum of c. ($V_S = 3.5$ mV, $I = 100$ pA, $V_{rms} = 10$ μ V).

A different scenario involves the splitting of the Shiba resonances due to magnetocrystalline anisotropy [93]. Previous works [89] showed that three Shiba peaks in a single-channel $S = 1$ system arise as a consequence of axial and transverse magnetic anisotropy. In this case, three Shiba peaks are expected, and their intensity reflects the excitation cross-section. This allows the determination of the configuration of the ground state between a weakly-interacting case (free-spin) and the Kondo-screened regime. In the free-spin case ($k_B T_K \ll \Delta$), the ground state hosts a spin multiplet ($|m_s = -1, 0, +1\rangle$), whose peaks' intensity follow a Boltzmann distribution at finite temperature due to the thermal occupation of the three states. In

contrast, if the spin multiplet occurs in the excited state, all excitations have the same probability and the Shiba resonances present equal areas [89].

In light of the variation of Shiba states' energy position and intensity, we distinguish between two extreme cases: FeTPP molecules at the center and at the edge of the bright segment described by the Moiré pattern. In Fig. 7.7 we show the dI/dV spectra obtained on both positions, as well as their deconvolved counterpart. Deconvolution finds that the intensity of the Shiba resonances does not describe a Boltzmann distribution, as would be expected for the free-spin case in the presence of magnetic anisotropy. Interestingly, the peaks do not exhibit either equal areas, fingerprint of a single-channel Kondo-screened spin [89]. Furthermore, FeTPP molecules present variations in peak amplitude and energy position of the Shiba resonances, as shown in Fig. 7.5c. Hence, the origin of these peaks in terms of anisotropy can be discarded.

Bright molecules in the underscreened Kondo regime

In this Section we interrogate the ground state of the molecular system in the normal state. To do so, we apply an external magnetic field of $B = 0.5$ T in order to quench superconductivity on both sample and tip. The spectra on the molecule dramatically changed in the normal state. In Fig. 7.8a we show the dI/dV signal obtained over the Fe and pyrrole sites of FeTPP molecules on the normal Pb(111) state. The Shiba states disappeared and, instead, zero energy features compatible with Kondo physics emerged. On the pyrroles, a sharp, logarithmic-like zero bias resonance appears in the low energy spectra. On the center of the FeTPP molecule, the resonance partly vanishes and transforms into an asymmetric dip-like lineshape. These features are interpreted in terms of the Kondo effect [22], where the electron bath of the substrate introduces high-order scattering processes that quench the spin of the magnetic molecule, as shown in Section 2.

From the fit to the dI/dV curves in Fig. 7.8a to a Fano function, we obtained a $T_K = 6.2 \pm 0.2$ K, which is fairly the same along the molecule. However, the lineshape strongly changes from a sharp Lorentzian-like peak over the pyrroles to an asymmetric Fano-lineshape over the Fe. We characterized such behavior with the Fano parameter q , which changes sign along the molecule, being $q_{Fe} = 0.6$ and $q_{pyrrole} = -5$. The q parameter captures the interference between tunneling paths through the d -orbitals of the magnetic molecule and direct tunneling. When the tip is positioned on top of the pyrrole groups, there is preferential tunneling through molecular orbitals hybridized with the iron d -resonances. On the other hand, on the Fe site the asymmetric lineshape depicts a larger Fano interference, as a result of the increased probability of direct tunneling to the substrate.

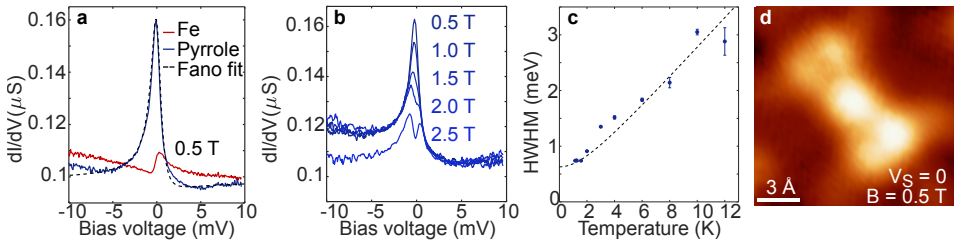


Figure 7.8: a, Kondo and Fano lineshapes obtained in the dI/dV spectra of bright molecules at $B = 0.5 \text{ T}$ on the pyrrole and iron sites, respectively. b, Magnetic field dependence of the Kondo resonance found on the pyrrole groups ($V_S = 10 \text{ mV}$, $I = 1 \text{ nA}$, $V_{rms} = 100 \mu\text{V}$). c, Temperature evolution of the half-width half-maximum of the Kondo resonance (blue dots). The expected behavior for the $\text{HWHM} = \frac{1}{2}\sqrt{(\alpha k_B T)^2 + (2k_B T_K)^2}$ is shown in black dashed line. d, Constant-height conductance map obtained at $V_S = 100 \mu\text{V}$ in the metallic state ($B = 0.5 \text{ T}$). The Fe site presents a higher conductance than expected from the lower intensity of the asymmetric Fano resonance. We attribute this to a topographic component in the constant-height Kondo map, that enhances the apparent conductance signal.

We further increased the magnetic field and observed the splitting of the Kondo resonance. In the case of a fully Kondo-screened impurity, i. e. $T \ll T_K$, the resulting Kondo resonance is expected to split due to the Zeeman energy above a critical magnetic field $B_c = 0.5k_B T_K/(g\mu_B)$ [?], which in the present case is $B_c \sim 2.3 \text{ T}$. In Fig. 7.8b is shown that the Zeeman splitting is resolved at lower magnetic field values. Such overestimation of the critical magnetic field might be caused by an enhancement in the response to the external magnetic field [118] in a partially screened $S > 1/2$ impurity. Numerical renormalization group calculations showed that for a $S = 1$ impurity, the critical magnetic field required to split an underscreened Kondo resonance scales as $B_c = k_B T_K/(8g\mu_B)$ [35, 118]. This brings $B_c \sim 0.6 \text{ T}$ for $T_K \sim 6.2 \text{ K}$. Therefore, at $B = 1 \text{ T}$ we should observe a Zeeman splitting of $280 \mu\text{V}$. However, the thermal energy at $T = 1.1 \text{ K}$ prevents the resolution of peaks separated by less than $\sim 300 \mu\text{V}$ with a metallic tip. Nevertheless, in Fig. 7.8b one can see a depletion in the resonance cusp at $B = 1.0 \text{ T}$, indicative of the response to the magnetic field, and a clear splitting at $B = 1.5 \text{ T}$. Furthermore, the Zeeman splitting observed at $B = 2.5 \text{ T}$ in Fig. 7.8b is $\sim 0.54 \text{ meV}$, in good agreement with the expected splitting for an underscreened spin $S = 1$ of $\sim 0.60 \text{ meV}$ [118] at $B = 2.5 \text{ T}$. An $S = 1$ impurity strongly interacting with a substrate may experience an incomplete screening of its magnetic moment, leading to the underscreened Kondo state. Therefore, one of the two unpaired electrons is

antiferromagnetically coupled to the bath, whereas the other one keeps its polarization.

To corroborate this picture, we performed temperature dependent measurements of the Kondo peak present over the pyrrole groups. We extracted the half-width half-maximum (HWHM) by fitting a Fano function to the Kondo resonance at different temperatures. In Fig. 7.8c, we plot the experimental widths as well as the quadratic temperature broadening of a Kondo resonance expected by the Fermi liquid treatment of the Kondo effect [?] $HWHM = \frac{1}{2}\sqrt{(\alpha k_B T)^2 + (2k_B T_K)^2}$. The α parameter indicates whether the impurity is in the weak-coupling ($T \gg T_K$) or strong-coupling ($T \ll T_K$) regime. Previous works [?] showed that a value of $\alpha = 2\pi$ corresponds to the strong-coupling regime, while deviations from this value indicate a weak-coupling mechanism due to $T \gg T_K$ [?, 119]. Our results yield to $\alpha = 2\pi$, indicating that the Kondo resonance is found in the strong-coupling regime $T \ll T_K$.

The enhanced sensitivity of the Kondo resonance to an external magnetic field is not the only feature expected for an underscreened $S = 1$ system. In the superconducting state, theoretical studies [93] predicted a decreased robustness of the free-spin state. As shown in Section 6, a $S = 1/2$ experiences a Quantum Phase Transition from a weakly-interacting free-spin configuration towards a Kondo-screened case at $T_K \sim 0.3\Delta/k_B$. However, in an underscreened $S = 1$, the value decreases to $T_K \sim 0.17\Delta/k_B$. In this particular case, the coupling strength J needed to drive the system from the free-spin to the Kondo-screened state would be $T_K \sim 1.6$ K. Since the experimentally determined value $T_K = 6.2 \pm 0.2$ K is larger than such quantum critical value, a Kondo-screened singlet is expected.

The Kondo map in Fig. 7.8d spatially locates the underscreened molecular spin. The stronger asymmetry in the Fano lineshape at the Fe site indicates a higher hybridization to the substrate, increasing the direct tunneling to the Pb(111). The zero-bias Kondo resonance found on the pyrroles indicates a less efficient Fano interference. Nevertheless, both are signatures of the underscreened Kondo spin $S = 1$ as can be extracted from their equal Kondo temperatures $T_K = 6.2 \pm 0.2$ K and the Zeeman splitting. The asymmetry described by the Fano factor q responds to the specific hybridization of the orbital at the Fe and pyrrole sites with the substrate, imposing the tunneling path. However, both signatures correspond to the same underscreened spin, distributed all along the molecule, presumably coupled through two hybridization channels (J_1 and J_2) to the Pb(111) substrate.

Multichannel configuration

Multiple Shiba states can also be interpreted in terms of multiple coupling channels between the impurity and the substrate [93]. A high spin $S > 1/2$ magnetic impurity on a surface is likely to present a low symmetric conformation that gives rise to a dominant coupling channel J_1 [93], which produces a Shiba bound state. A second hybridization channel, J_2 , may produce a second Shiba peak, although its spectral weight would be much smaller. In that scenario, two channels couple to the Cooper pairs' bath. Underscreening in the superconducting regime requires that one of the two channels fulfills $k_B T_{K_1} \gg \Delta$, and therefore the ground state of the impurity is $S = 1 - 1/2 = 1/2$. In the absence of magnetic anisotropy, two Shiba peaks are expected: one corresponding to a triplet excited state $S^* = 1$, and other to a singlet $S^* = 0$. Hence, we suggest that FeTPP molecules perform a multichannel coupling to the lead surface and the two Shiba resonances correspond to the two possible excitations mentioned above: an intense one closer to the Fermi level (J_1) and a faint one closer to the coherence peaks (J_2).

In the presence of a finite magnetic anisotropy D parameter, the Shiba resonance corresponding to J_1 would split into two, since two excitations become allowed due to the splitting of the excited state multiplet into $|m_S = \pm 1\rangle$ and $|m_S = 0\rangle$. In that scenario, the intensity of the resonance related to the $|m_S = \pm 1\rangle$ state would be more intense than the one to $m_S = 0$. In the presence of transverse anisotropy E , the coupling channel J_1 should exhibit three peaks of equal areas.

Deconvolution finds that the Shiba resonance close to the Fermi level is rather broad and exhibits a full-width half-maximum of 1.51 meV (see Fig. 7.7b). Such linewidth probably corresponds to the multiplet $|m_S = \pm 1, 0\rangle$, whose splitting is beyond our energy resolution due to weak magnetic anisotropy D . On the other hand, at the edge of the bright segment, three peaks can be resolved. We propose that the one corresponding to J_1 further splits due to the presence of stronger magnetic anisotropy D , and nearly overlaps with J_2 , as indicated in Fig. 7.7d.

Spatial asymmetry of the Shiba bound states

As mentioned in Section 6.2.1, the asymmetry in the intensity between the electron and hole components of the Shiba peaks reflects differences in the electron and hole wavefunctions of the Bogoliubov quasiparticle [100]. A finite potential scattering term breaks electron-hole symmetry in the normal state, leading to different intensities of the Shiba resonances at positive and negative bias [92, 94, 97, 101]. In terms of the single-impurity Anderson

model, a positive potential scattering term implies that the energy level ϵ_d hosting the electron would be far below the Fermi energy ϵ_F , therefore placing its empty counterpart $\epsilon_d + U_d$ close above ϵ_F . This configuration leads to a higher weight on the Shiba state at positive bias voltages.

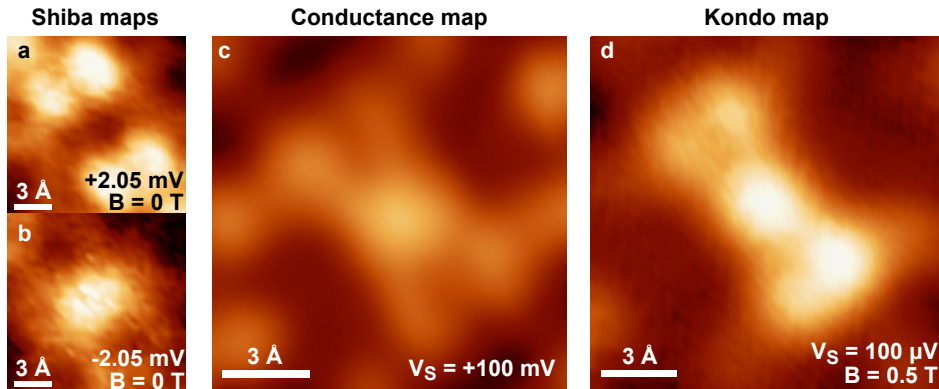


Figure 7.9: a, b, Electron and hole components of the Shiba bound state in the superconducting state ($B = 0$ T). c, Constant-height conductance map obtained at $V_S = 100$ mV. c, Constant-height conductance map obtained at $V_S = 100$ μ V in the metallic state ($B = 0.5$ T).

The spatial asymmetry of the Shiba resonances amplitude is opposite over the Fe pyrrole sites (see Fig. 7.1.1). Similar to the case of FeTPP on Au(111), we can define two tunneling paths: one on the center of the molecule n_1 and another one over the pyrrole groups n_2 . The two-fold symmetry found on the Shiba map in Fig. 7.9a at $V_S > 0$ is well reproduced by the orbital mapped at $V_S = +100$ mV in Fig. 7.9c. This is consistent with a positive potential scattering amplitude $\mathcal{U} > 0$, that leads to a higher weight on the Shiba resonances at positive energies. However, on the Fe site, the channel n_1 presumably has an associated potential scattering amplitude $\mathcal{U} < 0$ that inverts the intensity of the Shiba states. In spite of the spatial distribution of each channel, on both Fe and pyrrole sites the tunneling electrons excite both coherent quantum states, as extracted from the presence of the multiple Shiba peaks all along the molecule and from the Kondo map in Fig. 7.9d, which represents the screened spin distributed along the whole molecule. Nevertheless, each channel imposes its potential scattering term, thus inverting the intensity of the Shiba bound states from Fe to pyrrole sites.

7.1.2 Tuning the magnetic anisotropy in dark FeTPP molecules

We showed above the Moiré superstructure that conform bright and dark molecules. In addition to their different appearance in the STM topographs, they present an entirely different coupling with the superconducting substrate, as we will show in the following.

Inelastic spin excitations in the superconducting state.

In addition to the faint in-gap states, dark molecules showed two peak features symmetric with respect to the Fermi energy outside the superconducting gap (see Fig. 7.10a). Previous works [38, 48] on a similar paramagnetic molecule placed on top of superconductor, octa-ethyl FeTPP, attributed such peaks to the opening of an inelastic electron tunneling channel. In a normal metal, a symmetric step to zero bias voltage would be observed as a consequence of an inelastic spin excitation, as shown in Section 4. The superconducting tip and sample shift the excitation energy by $2\Delta \approx 2.7$ meV and repeats the coherence peaks DOS shape at the excitation threshold. Therefore, each peak corresponds to an inelastic spin excitation.

As shown in Section 2, inelastic spin excitations can be modeled by the phenomenological spin Hamiltonian [20, p. 15] $\hat{H}_s = D\hat{S}_z^2 + E(\hat{S}_x^2 - \hat{S}_y^2)$. Upon surface adsorption, FeTPP molecules typically maintain a $S = 1$. Therefore, an axial magnetic anisotropy term D would split the $|m_S = 0\rangle$ state from the $|m_S = \pm 1\rangle$ multiplet, and transverse anisotropy E would further split the $|m_S = \pm 1\rangle$ states. In order to extract the axial and transverse anisotropy values, we need to subtract twice the superconducting gap energy $2\Delta \approx 2.7$ meV to the inelastic peaks' energy position that appear at $|V_S| = 12.46$ mV and $|V_S| = 13.39$ mV. This yields to $D = 10.25$ meV and $E = 0.45$ meV.

Careful analysis of the excitation energy shows slight variations in the peak positions for different molecules in the range of $|V_S| = 12.46 \pm 0.16$ mV for the inner peak and $|V_S| = 13.39 \pm 0.08$ mV for outer peak. In Fig. 7.10b we show the dI/dV spectra of three neighboring dark FeTPP molecules and indicate with the dashed line the minor changes in the excitation energy between molecules. We attribute such slight differences in excitation energy to minor distortions of the individual molecules due to slightly different adsorption conformations of the incommensurate molecular island and the lead atomic lattice. However, as we will show in the following, stronger variations of the magnetic anisotropy energy can be induced with the STM tip.

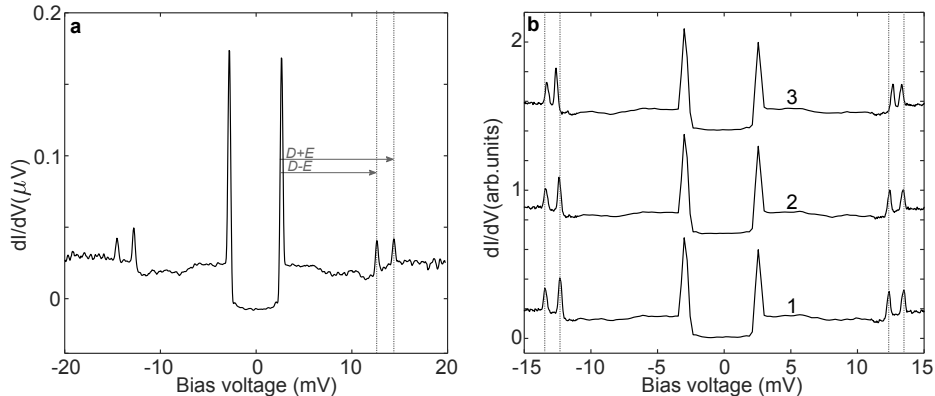


Figure 7.10: **a**, dI/dV spectra of a dark molecule showing anisotropy peaks, as indicated with the arrows. **b**, dI/dV spectra of three neighboring dark molecules. The slight differences in the energy position of the anisotropy peaks is indicated with a dashed line. ($V_S = 20$ mV, $I = 1$ nA, $V_{rms} = 30$ μ V).

Local distortions of magnetic anisotropy within a single molecule

Magnetocrystalline anisotropy governs the spin as a whole, which is distributed along the molecule due to the hybridization of the Fe d -shell with the molecular orbitals. Interestingly, we found that both the energy position and the separation between the inelastic peaks change within each molecule. In Fig. 7.11 we show the stacked plot of dI/dV spectra obtained along the same FeTPP molecules showed in fig. 7.10b. We observed that, at the Fe site, axial anisotropy D increased and transverse anisotropy E decreased with respect to the pyrrole sites. Therefore the local changes of the D and E parameters might be related to the tip interacting differently at Fe and pyrrole sites. Previous works probed the chemical forces that govern the tunneling current in atom-scale metallic junctions [120]. Farinacci and co-workers [?] showed that the interaction between the STM tip and a molecule was more efficient on the Fe site than on the organic ligands. Therefore, we can conclude that the changes in D and E anisotropy parameters in the FeTPP molecules come in response to the stronger attractive force of the tip at the Fe site, which drives the molecule towards a more planar (higher D) and less distorted (lower E) conformation.

In order to demonstrate the existence of such interaction, we performed z -dependent dI/dV spectra over the Fe site, as shown in Fig. 7.12a,b. As the tip-sample distance is decreased down to $\Delta z = -160$ pm, the axial term D monotonically increases, while transverse E decreases. This is precisely the effect observed along single molecules (see Fig. 7.11), corroborating the

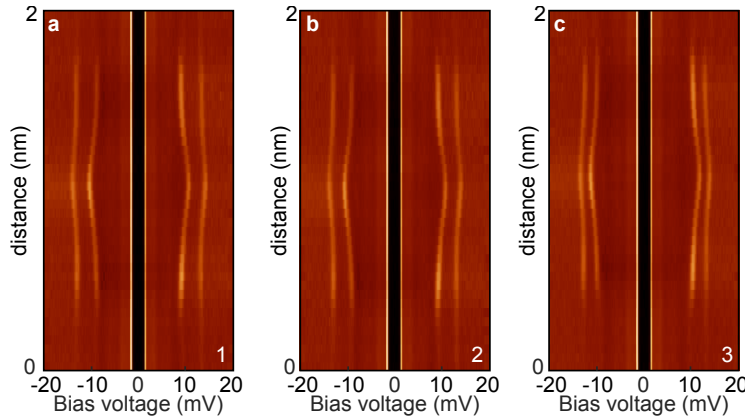


Figure 7.11: a, b, c Stacked plot of dI/dV spectra obtained along the three molecules showed in Fig. 7.10b. Along each single molecule slight differences in the anisotropy parameters D and E arise. ($V_S = 20$ mV, $I = 1$ nA, $V_{rms} = 30$ μ V).

attractive effect of the tip [?]. Interestingly, further reduction of tip-sample distance leads to the reopening of the inelastic peaks, increasing both D and E anisotropy terms, as sketched in fig. 7.12c. We attribute such behaviour to the repulsive regime reached at closer tip-molecule distances [?, 120], which pushes the molecule back towards the substrate.

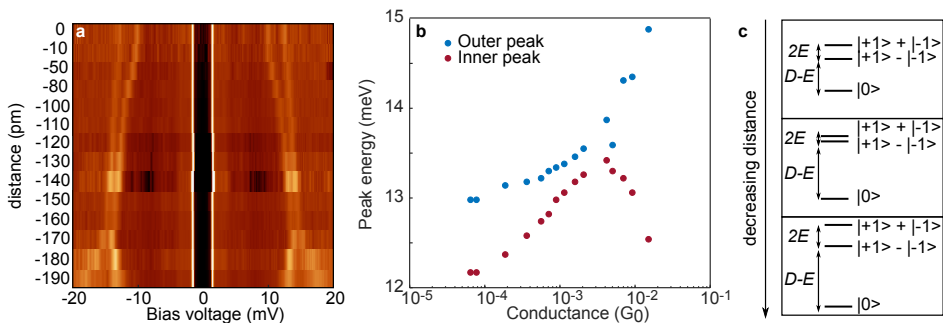


Figure 7.12: a, Evolution with tip-sample distance of dI/dV spectra taken on the Fe site of a dark molecule ($V_S = 20$ mV, $I = 100$ pA, $V_{rms} = 30$ μ V). b, Evolution of the anisotropy peaks energy with the normal-state conductance at $V_S = 20$ mV. c, Sketch representation of the energy levels splitting and the magnetic anisotropy values D and E as a function of the tip-sample distance.

Spin excitations in the normal state

In order to correlate the inelastic peaks outside the superconducting gap with the spin excitation conductance steps in the normal state, we applied an out-of-plane magnetic field of $B = 0.5$ T in order to quench superconductivity on both tip and sample. We found four inelastic steps as can be seen in Fig. 7.13a at $V_S = \pm 10.27 \pm 41.07$, ± 84.48 and ± 115.55 mV. Closer inspection of the ± 20 mV energy range reveals that the first inelastic step is actually split into two at $V_S = \pm 9.63$ and ± 10.90 mV, which correspond to the inelastic peaks observed in the superconducting state at $V_S = \pm 12.46$ and ± 13.39 mV that appear offset by 2Δ . The rest of the inelastic excitations in Fig. 7.13a at $V_S = \pm 41.07$, ± 84.48 and ± 115.55 mV most probably have vibrational origin, as expected for those energy values. We attribute the asymmetry in the inelastic excitations with the bias voltage in Fig. 7.13 to the symmetric and asymmetric contributions to the inelastic conductance for phononic excitations expected for asymmetric tunnel junctions [121,122].

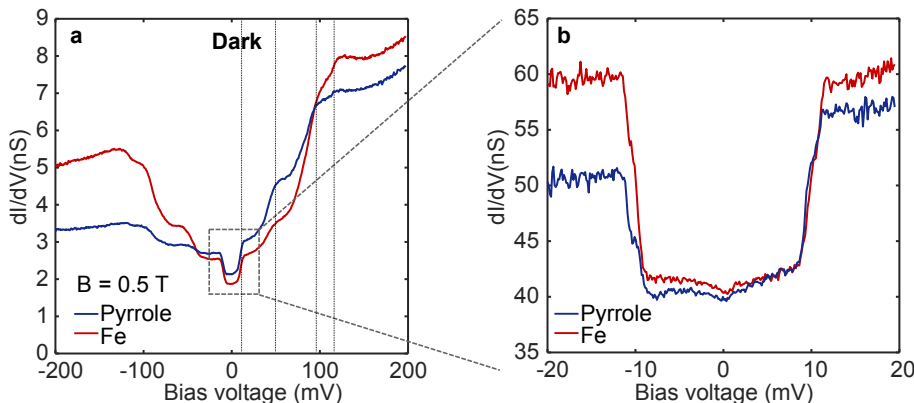


Figure 7.13: a, dI/dV spectra obtained on pyrrole (blue) and Fe (red) sites of dark FeTPP molecules ($V_S = 0.2$ V, $I = 1$ nA, $V_{rms} = 100$ μ V). b, Zoom-in shorter energy range of the dI/dV spectra showing two steps at $V_S = \pm 10$ mV due to the presence of transverse E magnetic anisotropy ($V_S = 20$ mV, $I = 1$ nA, $V_{rms} = 100$ μ V).

7.2 Conclusions

We found that FeTPP molecules perform a Moiré superstructure upon deposition on Pb(111). The incommensurability of the molecular island with the lead atomic structure determines the coupling of FeTPP to the substrate,

leading to two kinds of molecules: bright and dark.

Bright molecules show multiple Shiba bound states as a consequence of the coupling of the Fe magnetic moment with the superconductor underneath. We identified the origin of the multiple Shiba resonances as a consequence of a multichannel configuration in an underscreened Kondo $S = 1$. Close inspection of the intensity of the Shiba resonances found opposite intensities on the Fe and pyrrole sites, that we attribute to different potential scattering amplitudes on each tunneling path.

Dark FeTPP molecules present two peaks outside the superconducting gap at $V_S = \pm 12.46$ and ± 13.39 mV. We attribute them to inelastic excitations of the spin $S = 1$ from the ground state $|m_S = 0\rangle$ to the two excited states $|m_S = +1\rangle$ and $|m_S = -1\rangle$, split by the presence of axial D and transverse E magnetocrystalline anisotropy terms. Both D and E terms can be controlled by the tip-sample distance, due to the local distortions that the tip introduce, not only by its proximity to the molecule itself, but also by the different interaction of the tip with the Fe and pyrrole sites within a single molecule.

Chapter 8

Multifractal superconductivity in single-layer NbSe₂

Transition metal dichalcogenides (TMDs) are a family of materials of the type MX₂ where M is a transition metal atom (such as Nb, Mo, W) and X is a chalcogen atom (such as S, Se or Te). TMDs come in many forms, including semiconductors, metals, charge density wave (CDW) materials and superconductors [123,124]. Furthermore, their layered structure enables their scaling down to the monolayer limit, either by exfoliation method or by molecular beam epitaxy growth.

In this Section we show the characteristics of the superconducting state of the single-layer TMD NbSe₂, a recently discovered 2D superconductor [124] that exhibits a metallic ground state at low temperatures due to its spin-orbit coupling. Intrinsic weak disorder in our NbSe₂ monolayers triggers multifractality of the single-particle eigenstates, which dramatically impacts the superconducting properties of the 2D material. By means of spatially-resolved scanning tunneling spectroscopy at T = 1.1 K, well below the superconducting critical temperature of single-layer NbSe₂ ($T_c = 1.9$ K), we observe strong sub-nm-sized fluctuations in the superconducting order parameter amplitude (proportional to the SC width) as well as in the coherence-peak amplitude. We find that the spatial distribution of the SC order parameter amplitude corresponds to a log-normal type and, simultaneously, its spatial correlations show power-law decay for intermediate distances. These two features demonstrate that superconductivity in single-layer NbSe₂ is governed by the 2D multifractal regime of the electronic states induced by weak disorder.

This project is the result of a collaboration with Dr. Miguel M. Ugeda

(DIPC, San Sebastián, Spain) who design the experiment, Prof. Antonio M. García-García (Shanghai Center for Complex Physics, China) who performed the analytic calculations and Hyejin Ryu (LBNL, Berkeley, USA), Dr. Shujie Tang (LBNL, Berkeley, and Stanford University, USA), Prof. Zhi-Xun Shen (Stanford University, USA) and Prof. Sung-Kwan Mo (LBNL, Berkeley, USA) who grew the single-layer NbSe₂/BLG/SiC samples by molecular-beam epitaxy technique.

8.1 Spatial inhomogeneities of the superconducting gap

Our experiments were carried out on submonolayer NbSe₂ films grown on epitaxial bilayer graphene (BLG) on 6H-SiC(0001), as sketched in Fig. 8.1. The typical morphology of our samples (Fig. 8.2a) shows NbSe₂ islands uniformly distributed on the BLG/SiC(0001) terraces. Atomically resolved STM images of the islands (see Fig. 8.2b) exhibit high crystallinity of the NbSe₂ samples and show that the main source of defects are island edges as well as 1D grain boundaries (see Fig. 8.4b), a common type of defect in epitaxially grown TMD materials [125]. A previous work on single-layer NbSe₂ has revealed that superconductivity is severely depressed in the few- and single-layer limit [124, 126–128] as compared to the bulk case. Transport measurements in these type of samples (single-layer NbSe₂/BLG/SiC(0001)) have found a critical temperature (T_c) of 1.9 K (Refs. [124, 129]), a significant departure from the behavior of bulk NbSe₂, whose $T_c = 7.2$ K. At $T = 1$ K, charge density wave (CDW) order is fully developed in single-layer NbSe₂ as seen in the atomically resolved STM image in Fig. 8.2b and, therefore, should coexist with the superconducting state. STM dI/dV spectra of single-layer NbSe₂ (Fig. 8.2c) taken at different spatial locations of the same region confirm this coexistence. The spectra exhibit a dip in the density of states at the Fermi level (E_F) that corresponds to the superconducting gap. However, as can be noticed, the characteristic features of the SC gap, i.e. the depth, the width and the coherence peaks amplitude, are seen to locally

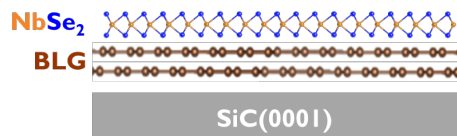


Figure 8.1: Side-view sketch of single-layer NbSe₂ grown on top of bilayer graphene/SiC by means of molecular beam epitaxy.

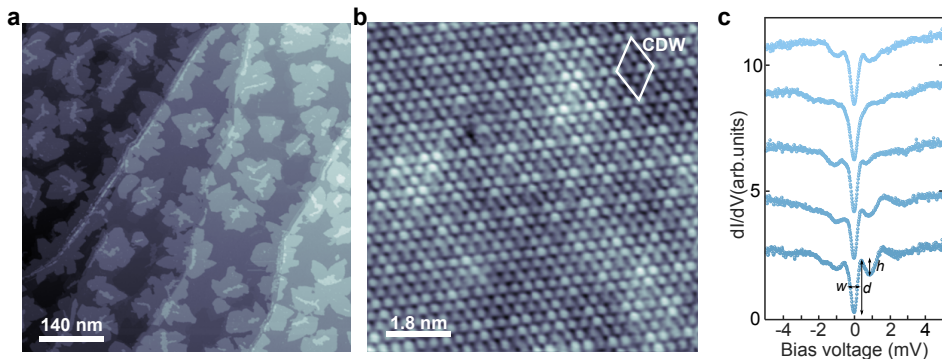


Figure 8.2: **a**, STM topograph of a large area of 0.7 ML NbSe₂/BLG ($V_S = 1$ V, $I = 10$ pA). **b**, Atomically resolved STM image of single-layer NbSe₂. The 3x3 CDW superlattice is indicated ($V_S = 14$ mV, $I = 1$ nA). **c**, Vertically offset dI/dV spectra acquired at several locations on a NbSe₂ island ($I = 1$ nA, $V_{rms} = 20\mu\text{V}$). The definition of superconducting gap width, depth and coherence peaks amplitude is indicated with arrows.

vary within the same nm-scale region of the 2D superconductor.

To better understand the nature of the SC fluctuations in single-layer NbSe₂, we first spatially mapped the width and depth of the SC gap in multiple monolayer regions with ~ 1 Å resolution (see Appendix for a detailed description of the fitting procedure of the SC gap). The width and depth of the SC gap are a measure of the local SC order parameter amplitude and the degree of development of the SC state, respectively. Figure 8.3a shows a representative map of the spatial distribution of the width of the SC gap in a 12.4 nm x 12.4 nm region (here a 90 x 90 mesh was used to yield 8100 width values). The width map unveils clear spatial fluctuations of the SC order parameter in single-layer NbSe₂ at the nm-scale. Fourier transform (FFT) analysis of this width map (Fig. 8.3b) yields a reciprocal-space ring of radius 0.46 ± 0.06 Å⁻¹, which reveals that a single wavelength of $\lambda = 7 \pm 1$ Å is involved in the complex pattern of the SC fluctuations in real space. The depth of the SC gap exhibits similar spatial fluctuations with the same wavelength (Fig. 8.3c).

To confirm the inhomogeneity of superconductivity in single-layer NbSe₂, we compare the spatial fluctuations of the order parameter (SC gap width, Fig. 8.3a) with the spatial distribution of the amplitude of the quasiparticle coherence peaks (Fig. 8.3d) acquired over the same region of Fig. 8.3a (12.4 x 12.4 nm²). The amplitude of these peaks is intimately related to long-range superconducting phase coherence and directly proportional to the quasiparticles' lifetime, which can be reduced by a variety of mecha-

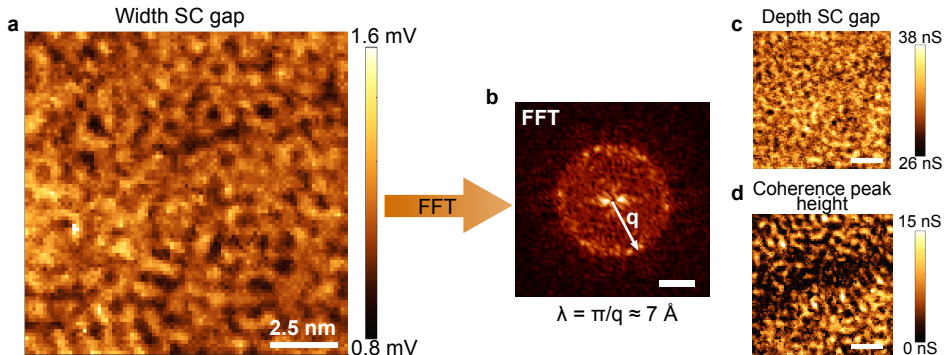


Figure 8.3: a, Spatial distribution of the superconducting gap width. b, FFT of the gap size distribution in a. The observed q vector corresponds to a wavelength of approximately 7 \AA . Scale bar is 0.25 \AA^{-1} . c, Real-space distribution of the depth of the superconducting gap on the same region in a. d, Spatial distribution of the coherence hole-peak amplitude on the same region in a.

nisms such as elastic scattering and thermal and quantum fluctuations that are typically enhanced in reduced dimensions and in the presence of disorder [109, 110, 112, 130]. The maps also show strong conductance (peak's amplitude) fluctuations over the same length scale as that seen for the SC width and depth (7 \AA), although surrounded by black patches which denote regions where the coherence peaks are depleted due to the intrinsic disorder in the 2D superconductor. Despite these fluctuations in the phase coherence at the submicron-scale, recent mesoscopic transport measurements in this kind of samples have revealed that the phase coherence still holds [124, 129].

Herein we focus on the origin of the characteristic wavelength of the SC order parameter and the coherence peaks amplitude fluctuations of $\sim 7 \text{ \AA}$. Such wavelength does not match either the atomic lattice (3.44 \AA) as in bulk [?], the CDW superlattice (10.3 \AA), or the underlying SiC reconstruction (32 \AA). In order to reveal its origin, we performed spatially resolved dI/dV mapping of the electronic structure of single-layer NbSe₂ at different bias voltages near E_F . Figure 8.4a shows a typical conductance map ($dI/dV(r, E)$) taken at $V_S = +40 \text{ mV}$ in a defective region (STM topograph of the same region in Fig. 8.4b). Defects act as scattering barriers and give rise to complex quasiparticle interference (QPI) patterns that extend several nanometers away from them, thus penetrating in pristine regions. Visualization of these QPI patterns allows us to analyze the momentum-space structure of the quasiparticle states. Figure 8.4c shows the Fourier analysis of the conductance map of Fig. 8.4a. The most rele-

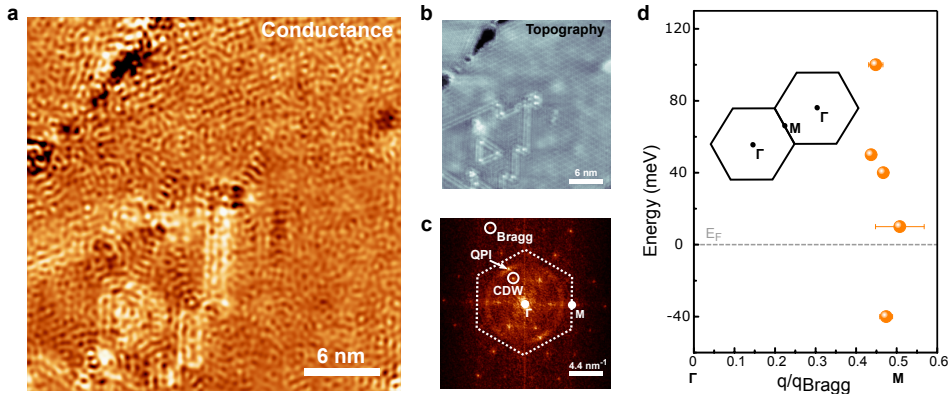


Figure 8.4: a, dI/dV conductance map taken at $V_S = 40$ mV. b, STM topograph of the region where the conductance map was acquired ($V_S = 40$ mV, $I = 1$ nA). This region illustrates the main source of intrinsic defects in our MBE-grown single layers of NbSe_2 , i.e., 1D grain boundaries and island edges. c, FFT of the conductance map in a. The anisotropic ring arising from the QPI is indicated as well as the points of the CDW and the atomic lattice (Bragg peaks). d, Energy dependence of the QPI wavevector along the ΓM direction extracted from the FFT of the dI/dV maps. The first and second Brillouin zones are shown in the inset.

vant feature of the FFT is the presence of an anisotropic ring with intensity maxima (q_{QPI}) along the same ΓM direction as the dispersionless CDW signal ($q_{CDW} \approx \Gamma M/3$). This feature is clearly observable in the Fourier transforms for all probed energies within ± 100 meV and shows a slight dispersion in k along ΓM as shown in Fig. 8.4d. The wavelength of the QPI patterns is $\lambda_{QPI} = 6.4 \pm 0.2$ Å, which nearly matches the periodicity of the SC fluctuations in real space. This suggests that both the SC fluctuations and the QPI-induced charge modulations are either intertwined or share a common origin. These QPI patterns have been previously observed in defective bulk 2H-NbSe₂ and are attributed to an enhancement of backscattering due to strong direction-dependent electron-phonon interactions [131]. *Ab initio* calculations in this material indicate that soft acoustic phonons along the ΓM direction are strongly coupled to electrons [?, ?]. This is a plausible origin of the spatial SC modulations given the significant role of acoustic phonons in the Cooper pairs formation. An alternative scenario is their correlation with the local DOS fluctuations within SC gap energy range according to the BCS formalism.

8.2 Statistical analysis of the SC gap width

Statistical analysis of the width values of the SC gap from the spatially resolved maps reveals relevant features of the SC fluctuations. Figure 8.5a shows the probability distribution of the SC gap width for the map shown in Fig. 8.3a. The values of the SC gap width are seen to fluctuate over a wide energy range of 0.8 meV around a mean value of 1.1 meV. Such a broad distribution reflects the large amplitude of the fluctuations of the SC order parameter (30% with respect to the mean value) induced by weak intrinsic disorder well below the critical temperature in single-layer NbSe₂.

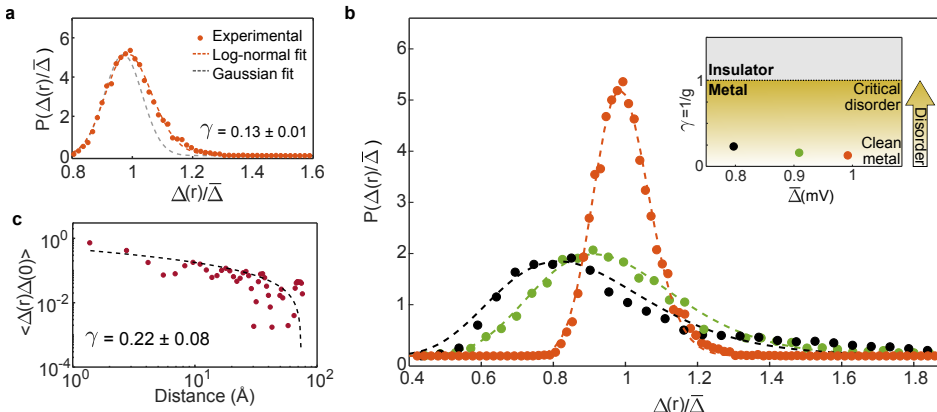


Figure 8.5: a, SC gap width probability distribution, normalized to the mean value of the gap. The deviation from a Gaussian distribution (grey dashed curve) and fit to a log-normal distribution from our theoretical model (orange dashed line) indicates the multifractal character. b, SC gap probability distribution for three regions of single-layer NbSe₂ with different disorder strengths ($\gamma = 1/g$, with g the Thouless conductance), which are quantified from the fit to a log-normal distribution. The inset shows the inverse relation between the disorder strength γ and the mean gap value ($\bar{\Delta}$) for the three regions, and illustrates the weak disorder regime (light yellow, $\gamma \ll 1$) probed in this work where multifractality emerges in the 2D limit. c, Two-point correlation function of the spatial SC gap width map (Fig. 8.3a) fitted to power-law decay.

Comparable spatial SC fluctuations have only been previously observed in the pseudogap regime of high T_c cuprates [132, 133]. Importantly, the distribution shows a marked right-skewed behavior, which is reproduced in all the single-layer regions studied here, although with different degrees of asymmetry as shown in Fig. 8.5b. Here we show a set of three experimental distributions of the SC width (dots) from regions with likely different degrees

of intrinsic disorder. Presumably, both the width of the distribution and its degree of asymmetry increase with the amount of disorder. The skewness is only observed in the statistics of the SC order parameter. In contrast, the distributions of the depth of the SC gap as well as the spatially resolved conductance around E_F (± 10 mV) for the same regions are seen symmetric and closely fit to a Gaussian distribution (see Appendix).

8.3 Theoretical modelling of the probability distribution of the superconducting gap

In order to understand the statistical distribution of the spatial modulations of the SC gap, Prof. Antonio M. García-García theoretically modelled single-layer NbSe₂ as a system close to the Anderson metal-insulator transition. In this regime, electronic states exhibit a multifractal nature characterized by an anomalous scaling of the inverse participation ratio and a power-law decay of eigenstate correlation functions [103–105] (see Appendix). The combination of multifractal electronic eigenstates and superconductivity leads to singular properties that largely depend on the spatial dimensionality. In 3D, where multifractality only emerges in the strong disordered limit ($\gamma = 1/g \approx 1$, with g the Thouless conductance), the superconducting state was predicted to be characterized by a spatially homogenous SC gap but substantially enhanced with respect to the clean limit [115, 116, 134]. In the 2D limit [135], multifractal superconductivity emerges in the weak disorder regime [117] ($\gamma \ll 1$). The SC gap shows a large spatial inhomogeneity well modelled by a log-normal distribution:

$$P\left(\frac{\Delta(r)}{\bar{\Delta}}\right) = \frac{\bar{\Delta}}{\Delta(r)\sqrt{2\pi\gamma\ln(E_0/\epsilon_D)}} \exp\left[-\frac{(\ln(\frac{\Delta(r)}{\Delta_\gamma}) - \frac{3}{2}\gamma\ln(\frac{\epsilon_D}{E_0}))^2}{2\gamma\ln(E_0/\epsilon_D)}\right] \quad (8.1)$$

with ϵ_D the Debye energy, E_0 an energy scale related to correlations of multifractal eigenvectors, and $\bar{\Delta}$ the average gap (see Appendix for details). Here γ is directly proportional to the disorder strength of the system and eq. 8.1 is valid for $\gamma = 8\pi/(k_Fl) \ll 1$. We have used this expression to fit the statistical distributions of the SC width maps measured in different regions of single-layer NbSe₂. As can be seen in Fig. 8.5a, the experimental right-skewed distribution of the SC width is well described by the log-normal distribution in the multifractal regime (dashed orange line). This fit yields a small γ value of 0.13 (within the range of applicability of eq. 8.1), which indicates that our NbSe₂ regions are barely defective. Regions with slightly different disorder can be nicely fitted to log-normal distributions (Fig. 8.5b),

yielding in all the cases small γ values ($\gamma \ll 1$) (see inset in Fig. 8.5b and Appendix). This set of distributions illustrates the evolution of the SC gap width with the disorder strength. As disorder (γ) increases, the statistical distribution of the SC gap width broadens and the mean SC gap value ($\bar{\Delta}$) decreases. This result implies that multifractality impacts 2D superconductivity even in the weak disorder regime and, therefore, it governs the fundamental properties of 2D superconductors throughout the metallic regime.

In the weak disorder regime, while superconductivity is largely affected by the multifractality of the electronic states, its effect on the conductance in the SC state is not observable in light of its nearly symmetric distribution (see Appendix for the conductance distributions). The reason for this is that, according to BCS theory, the SC gap depends exponentially on the coupling and, therefore, small changes in the coupling induce comparatively large changes in the gap. Therefore, superconductivity amplifies the effect of multifractality and enables its observation in nearly pristine 2D superconductors.

In order to corroborate the multifractal nature of the superconducting state in single-layer NbSe₂, we investigate the spatial correlations of the SC gap $\Delta(r)$, a fundamental property of the multifractal state. In addition to the log-normal distribution, another signature of multifractality is the power-law decay of eigenstate correlations for length scales larger than the mean free path [105] (\sim nm, see Appendix). Fig. 8.5c shows the two-point spatial correlation function of the SC order parameter, directly related to the two-point correlation of multifractal eigenstates, extracted from the SC gap width map of Fig. 8.3a. The observed decay of the correlations can be fitted to a power-law function restricted to intermediate distances as:

$$\langle \Delta(r)\Delta(r') \rangle \propto \left[\frac{1}{|r - r'|} \right]^{\gamma} \quad (8.2)$$

with the same exponent γ that governs the decay of the multifractal eigenstates ($\gamma = 0.22 \pm 0.08$ in Fig. 8.5a). The power-law decay is a robust feature in all the studied regions and for relatively long scales (0.7 nm $< |r - r'| <$ 7 nm). The fits to power-law functions in the studied regions yield γ values in qualitative agreement with those independently obtained from the log-normal distributions. In good agreement with our theoretical predictions [117], islands with smaller γ values present a power-law decay followed by faster decay (likely exponential) for longer distances.

8.4 Conclusions

In summary, we provide experimental evidence of the elusive multifractal superconducting state in a prototypical 2D correlated system triggered by disorder and low dimensionality. We demonstrate that multifractal characteristics fully manifest in the superconducting state even in the weak disorder regime. Multifractality is therefore expected to dominate the superconducting properties of the recently discovered family of highly crystalline 2D superconductors such as single layers of transition metal dichalcogenides. These 2D materials open the door for further investigation and eventual control of the intriguing multifractal regime.

Appendix

Superconducting gap fit

The fit of the superconducting gap to the prototypical Dynes' formula [?, 73] was elusive due to the spatial fluctuations of the coherence peaks and its absence in many positions. Instead, the superconducting gap parameters were obtained by fitting a reversed peak function to the gap, extracting its width and depth.

First, the dI/dV curves are selected in an energy range such as the Charge Density Wave gap [124] is excluded ($V_S = \pm 2.7$ mV, see shaded area in Fig. 8.6). Then, the algorithm obtains the minimum and the maximum values of the conductance that define the reversed peak function. The superconducting gap depth is calculated as the difference in conductance between these two points, and the width as the full-width-half-maximum of the reversed peak.

The coherence peaks height is obtained in a similar way. First, positive and negative energy ranges from the shaded area in Fig. 8.6 are separated. Then, a peak function is fitted to each energy range, obtaining the energy position of the center of the peak. We define a second point by adding up the energy of the center of the peak plus the full-width-half-maximum of the peak. The difference in conductance of the experimental data between these two points define the coherence peak height.

In Figure 8.6 we show a prototypical example of one dI/dV curve and the extracted values from the fitting procedure for the gap width, depth and coherence peak height.

Regarding the dI/dV curves that show no coherence peaks, we are aware that a slight deviation of the real width and depth values may be encountered. Nevertheless, these deviations do not change the real-space modulations of the superconducting gap width nor the asymmetry in the histograms since they represent only the 8% of the dI/dV curves.

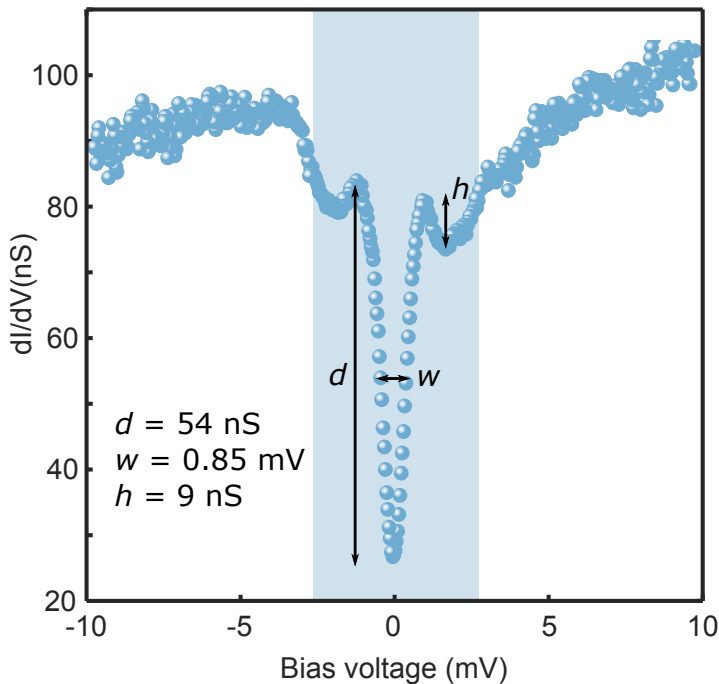


Figure 8.6: Example of width, depth and coherence peak height values extracted from the superconducting gap ($V_S = 10 \text{ mV}$, $I = 1 \text{ nA}$, $V_{rms} = 20 \mu\text{V}$).

Gap distribution for different areas

In Figure 8.7 we show the distribution of the superconducting gap width (Fig. 8.7a-c), superconducting gap depth (Fig. 8.7d-f), coherence peaks height (Fig. 8.7g-i) and conductance at $V_s = 0 \text{ mV}$ (Fig. 8.7j-l) for three different regions of single-layer NbSe₂ that show different disorder strength ($\gamma = 1/g = 0.13$, $\gamma = 1/g = 0.16$, $\gamma = 1/g = 0.23$, respectively). While the associated wave vector for the oscillations remains constant ($\lambda = 7 \pm 1 \text{ \AA}$), both the real-space pattern and the statistical distribution slightly change for different areas.

The asymmetry in the distribution of the superconducting gap width becomes more pronounced as the disorder strength increases, leading to a lower value for the mean gap width and a stronger right-skewed behaviour in the width distribution (see Fig. 8.7a-c), as expected for multifractal eigenstates in the presence of weak disorder.

For comparison, we show in Fig. 8.7d-f the distribution of the superconducting gap depth obtained with the same method as the width. Real-space oscillations are also visible as shown in the insets, reflecting the inhomogeneity of the superconducting gap overall shape. Nevertheless, the statistical distribution of the depth is symmetric regardless of the disorder strength. So far, no analytic models attempt to describe the behavior of the depth of the superconducting gap.

The distribution of the coherence peaks height shown in Fig. 8.7g is representative of a type that exhibits the maximum at finite heights, i.e., most of the coherence peaks are present and, therefore, the superconducting phase coherence persists. A second type of distributions (Fig. 8.7h) shows a Poisson shape with a clear maximum at zero height, which indicates much stronger phase fluctuations in those regions. We attribute this distinct behavior to variations in the density of defects among the studied regions, which is inversely proportional to the Thouless conductance (g).

In Fig. 8.7j-l we show the distribution of the conductance values at $V_s = 0$ mV over the same regions of single-layer NbSe₂. As discussed in Section 8, the distribution is expected to be symmetric since the non-trivial matrix elements induce a different coupling in each point of space. Since the superconducting gap depends exponentially on the coupling, small changes in the coupling will induce large changes in the superconducting gap. Therefore, multifractal effects are amplified and observable through the superconducting gap, while the distribution of the conductance remains symmetric at this level of weak-disorder in the weak-multifractality regime.

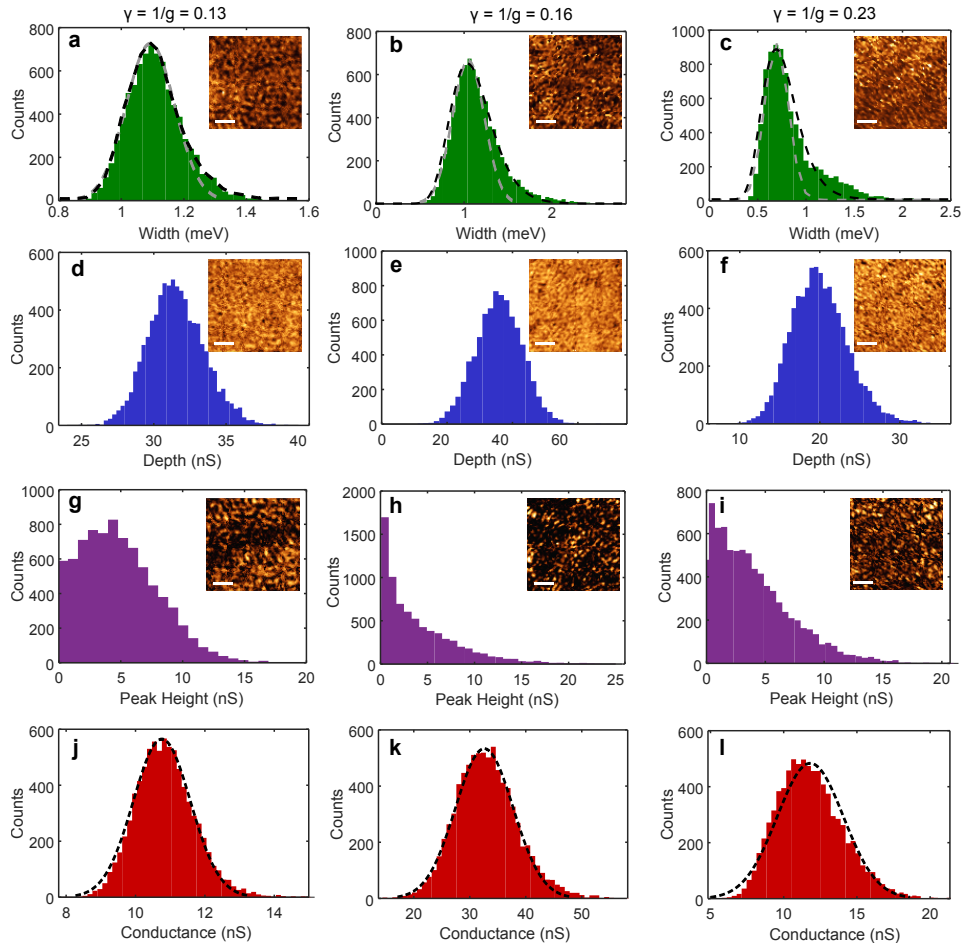


Figure 8.7: a-c, Distribution of the superconducting gap width on different areas of single-layer NbSe₂ and fit of a log-normal distribution (black dashed line). A Gaussian fit is shown in grey dashed line as a reference. The real-space distribution of the gap width is shown in the insets. The scalebar represents a, 2.5 nm, b, 3.6 nm, c, 2.5 nm. The colorbar range is a, 0.85-1.75 mV, b, 0.4-2.8 mV, c, 0-2.5 mV. d-f, Distribution of the coherence peak height on the same areas as a-c, respectively. The real-space distribution of the coherence peak height is shown in the insets. g-i, Distribution of the superconducting gap depth for the same areas. The real-space distribution is shown in the insets. j-l, Distribution of the conductance at $V_s = 0$ mV for different areas. The dashed line represents the fit to a Gaussian distribution.

Estimation of the mean free path

The mean free path (l) in a 2D system is $l = h/(2e^2) \cdot \sigma / \sqrt{\pi n}$, with σ and n the conductivity and electronic density of single-layer NbSe₂, respectively. Previous transport experiments in these type of samples have shown that $\sigma \approx 1/300 \Omega$ in the normal state, therefore $l = 24.4/\sqrt{n_{2D}}$. Literature values of n for single-layer NbSe₂ yield an electronic density per each atomic layer of $n = 1.1 \cdot 10^{15} \text{ cm}^{-2}$ [128]. Taking this value, the mean free path is $l \approx 7 \text{ nm}$. This estimation may largely vary due to other factors such as the presence of graphene, the exact geometry of the transport devices, and the exact value of n_{2D} . Therefore, we believe its validity restricts to its order of magnitude.

Inhomogeneous BCS superconductivity

We now provide a brief summary of the calculation leading to a log-normal distribution function of the order parameter amplitude and the two point correlation function employed in Section 8 developed by Prof. Antonio M. García-García. We follow Ref. [117] closely and refer to it for further details. The starting point of our analysis is the Bogoliubov-de Gennes(BdG) Hamiltonian [?, ?],

$$H = \int d\mathbf{r} \left[\sum_{\sigma} \Psi_{\sigma}^{\dagger}(\mathbf{r}) \left(-\frac{\hbar^2}{2m} \nabla^2 + U(\mathbf{r}) - \mu \right) \Psi_{\sigma}(\mathbf{r}) + \Delta(\mathbf{r}) \Psi_{\downarrow}^{\dagger}(\mathbf{r}) \Psi_{\uparrow}^{\dagger}(\mathbf{r}) + \text{h.c.} \right] \quad (8.3)$$

where $\Psi_{\sigma}^{\dagger}(\mathbf{r})$ creates an electron in position eigenstate \mathbf{r} and spin σ , $U(\mathbf{r})$ is a random potential,

$$\Delta(\mathbf{r}) = -\frac{\lambda}{\nu(0)} \langle \Psi_{\uparrow}(\mathbf{r}) \Psi_{\downarrow}(\mathbf{r}) \rangle, \quad (8.4)$$

λ is the dimensionless BCS coupling constant and $\nu(0)$ is the bulk density of states at the Fermi energy. Assuming that the spatial part of $\Psi_{\sigma}^{\dagger}(\mathbf{r})$ is proportional to the eigenstates of the one-body problem $\psi_{\mathbf{n}}(\mathbf{r})$, an approximation which should be valid in the limit of weak coupling and disorder [?, ?], it is possible to derive a modified BCS gap equation [?],

$$\Delta(\epsilon) = \frac{\lambda}{2} \int_{-\epsilon_D}^{\epsilon_D} \frac{I(\epsilon, \epsilon') \Delta(\epsilon')}{\sqrt{\epsilon'^2 + \Delta^2(\epsilon')}} d\epsilon' \quad (8.5)$$

where ϵ_D is the Debye energy and $\Delta(\epsilon)$ is the superconducting gap as a function of energy. The BCS interaction matrix elements are, $I(\epsilon, \epsilon') = V \int d\mathbf{r} |\psi(\epsilon, \mathbf{r})|^2 |\psi(\epsilon', \mathbf{r})|^2$ where $\psi(\epsilon, \mathbf{r})$ is the eigenstate of the one-body problem of energy ϵ .

As was mentioned previously, eigenfunctions of a disordered system close to a metal-insulator transition are multifractal [?, 105]. There are different ways to characterize this multifractality, for instance in the inverse participation ratio (IPR) [103, 104],

$$P_q = \int d\mathbf{r} |\psi(\mathbf{r})|^{2q} \sim L^{d_q(q-1)}, \quad (8.6)$$

is related to an anomalous scaling with the system size. A signature of multifractality in eigenstate correlation functions,

$$I(\epsilon, \epsilon') = \left(\frac{E_0}{|\epsilon - \epsilon'|} \right)^\gamma \quad (8.7)$$

is a slow power-law decay with $\gamma = 1 - \frac{d_2}{d}$ which is cutoff for energy differences smaller than the mean level spacing and larger than $E_0 \sim (\nu(0)L_0^2)^{-1}$ an energy scale related to the minimum length L_0 for which fractal behavior is observed. Typically L_0 is of the order of the mean free path, ℓ . For weak disorder in quasi-two dimensions, $L_0 \sim \ell \sim g/k_F$ and therefore $E_0/\epsilon_D \sim \frac{E_F}{\epsilon_D g^2}$ which we expect to be an energy scale between the Fermi and the Debye energy. The exponent γ is directly related to the disorder strength, $\gamma \approx 1/g \ll 1$ where $g \gg 1$ is the dimensionless conductance.

We have now all the information necessary to briefly summarize the calculation of the distribution function of the order parameter. In the limit $\gamma \ll 1$ it is possible to compute $\Delta(\epsilon)$ analytically by expanding $I(\epsilon, \epsilon')$ in powers of γ and solving the gap equation Eq. (8.5) order by order. The spatial dependence of the order parameter amplitude [?, ?] is given by,

$$\langle \Delta(\mathbf{r}) \rangle = \frac{\lambda V}{2} \int \frac{\Delta(\epsilon)}{\sqrt{\Delta(\epsilon)^2 + \epsilon^2}} |\psi(\epsilon, \mathbf{r})|^2 d\epsilon, \quad (8.8)$$

and higher moments,

$$\langle \Delta^n(\mathbf{r}) \rangle = \int d\mathbf{r} \prod_{j=1}^n \left(\frac{\lambda V}{2} \int \frac{\Delta(\epsilon_j)}{\sqrt{\Delta(\epsilon_j)^2 + \epsilon_j^2}} |\psi(\epsilon_j, \mathbf{r})|^2 d\epsilon_j \right), \quad (8.9)$$

are evaluated analytically by a similar expansion in $\gamma \ll 1$ keeping only the leading terms. The final result is,

$$\langle \Delta^n(\mathbf{r}) \rangle \propto e^{\gamma \ln(\epsilon_D/E_0)(3n-n^2)/2}. \quad (8.10)$$

A similar expression was derived in Ref. [115] in the limit of strong disorder $g \sim 1$ where the perturbative expansion in g should break down. These are the moments of a log-normal distribution,

$$\mathcal{P}\left(\frac{\Delta(\mathbf{r})}{\bar{\Delta}}\right) = \frac{\bar{\Delta}}{\Delta(\mathbf{r})\sqrt{2\pi}\sigma} \exp\left[-\frac{\left(\ln\left(\frac{\Delta(\mathbf{r})}{\bar{\Delta}}\right) - \mu\right)^2}{2\sigma^2}\right] \quad (8.11)$$

with $\mu = \gamma \ln(\epsilon_D/E_0)/2$, $\sigma = \sqrt{\gamma \ln(E_0/\epsilon_D)}$,

$$\bar{\Delta} = D(\gamma)\epsilon_D \left(1 + \frac{\gamma}{\lambda} \left(\frac{\epsilon_D}{E_0}\right)^\gamma\right)^{-\frac{1}{\gamma}} \left(\frac{\epsilon_D}{E_0}\right)^\gamma, \quad (8.12)$$

and

$$D(\gamma) = \left(\frac{\gamma\Gamma(\frac{1}{2}(1-\gamma))\Gamma(\frac{\gamma}{2})}{2\sqrt{\pi}}\right)^{\frac{1}{\gamma}}. \quad (8.13)$$

Finally, we compute the two point correlation function $\langle \Delta(r)\Delta(r') \rangle$. For multifractal eigenstates [105]

$$\langle |\psi(\epsilon, \mathbf{r})|^2 |\psi(\epsilon', \mathbf{r}')|^2 \rangle \sim \frac{1}{|r - r'|^\gamma |\epsilon - \epsilon'|^\gamma d} \quad (8.14)$$

where the decay in energy is cutoff in the way explained previously. Regarding the power-law decay in space, multifractality cannot be observed for distances shorter than the mean free path. For finite size systems, multifractality is also restricted to distances shorter than the system size. Similarly, for systems close but not at the critical point ϵ_c , multifractality is restricted to lengths smaller than $\zeta \sim |\epsilon - \epsilon_c|^{-\nu}$ even in the thermodynamic limit. Finally, we note [105] that, for eigenstates separated in energy by $\omega = \epsilon - \epsilon'$, the spatial power-law decay cannot hold for distances longer than $L_\omega \sim (\frac{1}{\omega\rho})^{1/d}$. The decay for distances larger than ζ, L_ω is not universal and likely exponential in most cases. From Eq.(8.8), it is straightforward to show that this power-law decay of eigenstate correlations translates into a similar power-law decay of the order parameter spatial correlations for intermediate distances $\ell < |r - r'| < L_\omega, \zeta$:

$$\langle \Delta(r)\Delta(r') \rangle \propto \frac{1}{|r - r'|^\gamma}. \quad (8.15)$$

In Section 8 we compare these analytical predictions with experimental results in different zones of the sample. Overall, we have found good agreement between theory and experiment in all zones for both the gap distribution function and the two-point correlation function. Each zone is described by a different $g \gg 1$ which is typical of two or quasi two dimensional

superconductors where features expected at the Anderson metal-insulator transition are observed for a broad range of values of the dimensionless conductance provided that the localization length is larger than the system size.

Chapter 9

Conclusions and Outlook

This Thesis comprises the study of magnetism and superconductivity at the atomic scale. The use of low-temperatures gives access to the atomic spin, the superconducting ground state and the interactions among them. By means of Scanning Tunneling Microscopy and Spectroscopy, and with the support of theoretical simulations and analytic calculations, we provide a fundamental understanding on the significant effects that minor modifications produce in atomic magnets and superconductors.

Our work demonstrates that small variations in the interactions between atomic spins and their environment govern the magnetic characteristics of single atoms and molecular magnets, where magnetic exchange coupling is extremely sensitive to the surface effect.

The magnetic moment of single transition metal atoms is conserved upon deposition on an insulating surface. The magnetic properties of Cr and Fe adatoms are governed by two energy scales that coexist in such a system: the Kondo effect and magnetic anisotropy, which can be tuned by the adsorption of a hydrogen molecule. Thorough analysis of the impurities' spectroscopic fingerprints showed that the low, axial anisotropic configuration of Cr atoms can be tuned towards a high-anisotropic one by the adsorption of a hydrogen molecule. Conversely, upon adsorption of H₂, the highly anisotropic system that is Fe/Cu₂N shift towards a low-anisotropy configuration and hybridized strongly with the metallic substrate, enabling Kondo-like processes.

Using a molecular core to host a magnetic impurity is a promising approach for achieving large anisotropy energies, such as the ones host by FeTPP molecules on Au(111). We combined the single-impurity Anderson model, Density Functional Theory simulations and high-order perturbation theory and developed the understanding of the high-order scattering processes that govern the magnetic properties of iron porphyrins. Given the distribution of the total spin $S = 1$ in two spatially-separated spin-polarized

orbitals along molecule, two excitation paths arise, each of them determining the symmetry of the low-energy spin-flip features.

Stabilization of high magnetic moments requires the arrangement of several spins in coupled structures, such as organic platforms. Our study in double iron porphyrin structures suggests that the indirect exchange coupling between the two Fe atoms is quenched upon surface deposition, due to the hybridization between the π -organic backbone and the electron bath of the metal underneath.

The study of FeTPP molecules on a superconducting substrate reported a more complete description of the substrate-spin interactions. Analysis of the multiple Shiba states present in the molecular spin found the system in a multichannel configuration with a partially quenched magnetic moment that lies in an underscreened Kondo ground state.

Future work considering different decoupling layers, such as insulating NaCl islands or semiconducting MoS₂ would provide the required isolation for the spins to hold stable magnetization. In that scenario, organic multi-center molecules would presumably preserve the intramolecular coupling, leading to stable high-spin molecular magnets.

Motivated by the exploration of new superconducting materials, we investigate crystalline two-dimensional single-layer NbSe₂. We found that the local superconducting characteristics are extremely sensitive to weak disorder due to the two-dimensional nature of the superconductor, and follow the expected behavior for a system governed by multifractal eigenstates. In light of such exotic behaviour of the two-dimensional superconductor, it is envisioned as a unique platform for tailoring the superconducting characteristics as well as for the study of the interaction with the single spins.

In conclusion, our work has broaden the overall picture of single atomic spins and their interactions, which govern their magnetic ground state, and contributes to provide the tools to design single-atom magnets. The emergence of multifractal eigenstates in a two-dimensional superconductor offers a new platform to tune and control superconductivity in two-dimensional materials.

Bibliography

- [1] C. Joachim, J. Gimzewski, and A. Aviram, “Electronics using hybrid-molecular and mono-molecular devices,” *Nature*, vol. 408, pp. 541–548, 2000.
- [2] S. A. Wolf, “Spintronics: A Spin-Based Electronics Vision for the Future,” *Science*, vol. 294, pp. 1488–1495, 2001.
- [3] L. Bogani and W. Wernsdorfer, “Molecular spintronics using single-molecule magnets,” *Nature Materials*, vol. 7, pp. 179–186, 2008.
- [4] S. Schmaus, A. Bagrets, Y. Nahas, T. K. Yamada, A. Bork, M. Bowen, E. Beaurepaire, F. Evers, and W. Wulfhekel, “Giant magnetoresistance through a single molecule,” *Nature Nanotechnology*, vol. 6, pp. 185–189, 2011.
- [5] V. A. Dediu and L. E. Hueso, “Spin routes in organic semiconductors,” *Nature Materials*, vol. 8, pp. 707–716, 2009.
- [6] X. Sun, S. V\’elez, A. Atxabal, A. Bedoya-Pinto, S. Parui, X. Zhu, R. Llopis, F. Casanova, and L. E. Hueso, “A molecular spin-photovoltaic device,” *Science*, vol. 357, pp. 677–680, 2017.
- [7] J. Kondo, “Effect of Ordinary Scattering on Exchange Scattering from Magnetic Impurity in Metals,” vol. 169, no. 2, pp. 437–440, 1968.
- [8] C. F. Hirjibehedin, C. Y. Lin, A. F. Otte, M. Ternes, C. P. Lutz, B. A. Jones, and A. J. Heinrich, “Large magnetic anisotropy of a single atomic spin embedded in a surface molecular network,” *Science*, vol. 317, no. 5842, pp. 1199–1203, 2007.
- [9] L. Yu, “Bound state in superconductors with paramagnetic impurities,” *Acta Phys. Sin.*, vol. 21, pp. 75–91, 1965.
- [10] H. Shiba, “Classical Spins in Superconductors,” *Prog. Theo. Phys.*, vol. 40, no. 3, p. 435, 1968.
- [11] A. I. Rusinov, “Superconductivity near a Paramagnetic Impurity,” *ZhETF Prisma Redaktsiiu*, vol. 9, p. 146, 1968.

- [12] S. H. Ji, T. Zhang, Y. S. Fu, X. Chen, X. C. Ma, J. Li, W. H. Duan, J. F. Jia, and Q. K. Xue, “High-resolution scanning tunneling spectroscopy of magnetic impurity induced bound states in the superconducting gap of Pb thin films,” *Physical Review Letters*, vol. 100, no. 22, pp. 16–18, 2008.
- [13] K. J. Franke, G. Schulze, and J. I. Pascual, “Competition of superconducting phenomena and Kondo screening at the nanoscale,” *Science*, vol. 332, no. 6032, pp. 940–944, 2011.
- [14] B. Stipe, M. Rezaei, and W. Ho, “Single-molecule vibrational spectroscopy and microscopy,” *Science*, vol. 280, pp. 1732–1735, 1998.
- [15] I. Horcas and R. Fernández, “{WSXM}: {A} software for scanning probe microscopy and a tool for nanotechnology,” *Review of Scientific Instruments*, vol. 78, p. 013705, 2007.
- [16] M. Ruby, “Spectrafox: A free open-source data management and analysis tool for scanning probe microscopy and spectroscopy.,” *SoftwareX*, vol. 5, 2016.
- [17] P. Anderson, “Localized magnetic states in metals,” *Physical Review*, vol. 124, p. 41, 1961.
- [18] J. R. Schrieffer and P. A. Wolff, “Relation between the Anderson and Kondo Hamiltonians,” *Phys. Rev.*, vol. 149, no. 2, p. 491, 1966.
- [19] M. Ternes, “Spin Excitations and Correlations in Scanning Tunneling Spectroscopy Markus,” *arXiv.org*, pp. arXiv:1505.04430 [cond-mat.mes-hall], 2015.
- [20] D. Gatteschi, R. Sessoli, and J. Villain, *Molecular nanomagnets*. 2006.
- [21] J. Kondo, “Resistance Minimum in Dilute Magnetic Alloys,” *Progress of Theoretical Physics*, vol. 32, no. 1, pp. 37–49, 1964.
- [22] A. Hewson, *The Kondo Problem to Heavy Fermions*, edited by D. Edwards and D. Melville. 1997.
- [23] T. Choi, C. D. Ruggiero, and J. A. Gupta, “Incommensurability and atomic structure of c (2Å—2) N/Cu (100): A scanning tunneling microscopy study,” *Physical Review B - Condensed Matter and Materials Physics*, vol. 78, no. 3, pp. 1–5, 2008.
- [24] A. J. Heinrich, J. A. Gupta, C. P. Lutz, and D. M. Eigler, “{Single-{Atom} {Spin}-{Flip} {Spectroscopy}},” *Science*, vol. 306, pp. 466–469, 2004.

- [25] U. Fano, “Effects of Configuration Interaction on Intensities and Phase Shifts,” vol. 124, no. 6, p. 1866, 1961.
- [26] Q. Dubout, F. Donati, C. Wäckerlin, F. Calleja, M. Etzkorn, A. Lehnert, L. Claude, P. Gambardella, and H. Brune, “Controlling the spin of Co atoms on Pt(111) by hydrogen adsorption,” *Physical Review Letters*, vol. 114, no. 10, pp. 1–5, 2015.
- [27] F. Donati, Q. Dubout, G. Autès, F. Patthey, F. Calleja, P. Gambardella, O. V. Yazyev, and H. Brune, “Magnetic moment and anisotropy of individual Co atoms on graphene,” *Physical Review Letters*, vol. 111, no. 23, pp. 2–6, 2013.
- [28] M. Pivetta, M. Ternes, F. Patthey, and W. D. Schneider, “Diatom molecular switches to enable the observation of very-low-energy vibrations,” *Physical Review Letters*, vol. 99, no. 12, pp. 21–24, 2007.
- [29] M. Ternes, A. J. Heinrich, and W. D. Schneider, “Spectroscopic manifestations of the Kondo effect on single adatoms,” *Journal of Physics Condensed Matter*, vol. 21, no. 5, 2009.
- [30] F. D. Natterer, F. Patthey, and H. Brune, “Quantifying residual hydrogen adsorption in low-temperature STMs,” *Surface Science*, vol. 615, pp. 80–87, 2013.
- [31] D. Serrate, M. Moro-Lagares, M. Piantek, J. I. Pascual, and M. R. Ibarra, “Enhanced hydrogen dissociation by individual co atoms supported on ag(111),” *Journal of Physical Chemistry C*, vol. 118, no. 11, pp. 5827–5832, 2014.
- [32] S. J. Altenburg and R. Berndt, “Tungsten-hydrogen complexes on graphene on Ir(111),” *New Journal of Physics*, vol. 16, 2014.
- [33] B. Bryant, A. Spinelli, J. J. T. Wagenaar, M. Gerrits, and A. F. Otte, “Local control of single atom magnetocrystalline anisotropy,” *Physical Review Letters*, vol. 111, no. 12, pp. 1–5, 2013.
- [34] V. Iancu, A. Deshpande, and S.-W. Hla, “Manipulating Kondo temperature via single molecule switching,” *Nano Letters*, vol. 6, pp. 820–823, 2006.
- [35] J. J. Parks, A. R. Champagne, T. A. Costi, W. W. Shum, A. N. Pasupathy, E. Neuscamman, S. Flores-Torres, P. S. Cornaglia, A. A. Aligia, C. A. Balseiro, G. K. L. Chan, H. D. Abruña, and D. C. Ralph, “Mechanical Control of Spin States in Spin-1 Molecules and the Underscreened Kondo Effect,” *Science*, vol. 328, no. 5984, pp. 1370–1373, 2010.

- [36] T. Komeda, H. Isshiki, J. Liu, T. F. Zhang, N. Lorente, K. Katoh, B. K. Breedlove, and M. Yamashita, “Observation and electric current control of a local spin in a single-molecule magnet,” *Nature Communications*, vol. 2, p. 217, 2011.
- [37] B. W. Heinrich, G. Ahmadi, V. L. Müller, L. Braun, J. I. Pascual, and K. Franke, “Change of the magnetic coupling of a metal–organic complex with the substrate by a stepwise ligand reaction,” *Nano Letters*, vol. 13, pp. 4840–4843, 2013.
- [38] B. W. Heinrich, L. Braun, J. I. Pascual, and K. J. Franke, “Tuning the Magnetic Anisotropy of Single Molecules,” *Nano Letters*, vol. 15, pp. 4024–4028, 2015.
- [39] W. Auwarter and D. EciJA, “Porphyrins at interfaces,” *Nature Chemistry*, v –120, 2015.
- [40] G. Kuang, Q. Zhang, T. Lin, R. Pang, X. Shi, H. Xu, and N. Lin, “Mechanically-Controlled Reversible Spin Crossover of Single Fe-Porphyrin Molecules,” *ACS Nano*, vol. 11, pp. 6295–6300, 2017.
- [41] S. Karan, C. Garc\'ia, M. Karolak, D. Jacob, N. Lorente, and R. Berndt, “Spin control induced by molecular charging in a transport junction,” *Nano Letters*, vol. 18, no. 1, pp. 88–93, 2018.
- [42] A. Zhao, Q. Li, L. Chen, H. Xiang, W. Wang, S. Pan, B. Wang, X. Xiao, J. Yang, J. G. Hou, and G. Zhu, “Controlling the Kondo effect of an adsorbed magnetic ion through its chemical bonding,” *Science*, vol. 309, pp. 1542–1544, 2005.
- [43] V. Iancu, A. Deshpande, and S.-W. Hla, “Manipulation of the Kondo effect via two-dimensional molecular assembly.,” *Physical Review Letters*, vol. 97, p. 266603, 2006.
- [44] A. Zhao, H. Zhenpeng, B. Wang, X. Xiao, J. Yang, and J. G. Hou, “Kondo effect in single cobalt phthalocyanine molecules adsorbed on Au(111) monoatomic steps,” *Journal Chemical Physics*, vol. 128, p. 234705, 2008.
- [45] A. Str\"o\"om if mode\\$dotz\\$else\\$z\\$fiecka, M. Soriano, and J. I. Pascual, “Revers
- [46] J. C. Oberg, M. R. Calvo, F. Delgado, M. Moro-Lagares, D. Serrate, D. Jacob, J. Fernández-Rossier, and C. F. Hirjibehedin, “Control of single-spin magnetic anisotropy by exchange coupling,” *Nature Nanotechnology*, vol. 9, pp. 64–68, 2014.
- [47] T. Gopakumar, H. Tang, J. Morillo, and R. Berndt, “Transfer of {Cl} {Ligands} between {Adsorbed} {Iron} {Tetraphenylporphyrin} {Molecules},” *Journal of the American Chemical Society*, vol. 134, pp. 11844–11847, 2012.

- [48] B. W. Heinrich, L. Braun, J. I. Pascual, and K. J. Franke, “Protection of excited spin states by a superconducting energy gap,” *Nature Physics*, vol. 9, pp. 765–768, 2013.
- [49] H. Chen, T. Pope, A. Y. Wu, D. Wang, L. Tao, D. L. Bao, W. Xiao, J. L. Zhang, Y. Y. Zhang, S. Du, S. Gao, S. T. Pantelides, W. A. Hofer, and H. J. Gao, “Evidence for ultralow-energy vibrations in large organic molecules,” *Nano Letters*, vol. 17, no. 8, pp. 4829–4933, 2017.
- [50] P. Boyd, D. Buckingham, R. McMeeking, and S. Mitra, “Paramagnetic anisotropy, average magnetic susceptibility, and electronic structure of intermediate-spin $\{S\} = 1$ (5, 10, 15, 20-tetraphenylporphyrin) iron ($\{II\}$)”, *Inorganic Chemistry*, vol. 18, pp. 3585–3591, 1979.
- [51] S. Frank and D. Jacob, “Orbital signatures of fano-kondo line shapes in stm adatom spectroscopy,” *Physical Review B*, vol. 92, p. 235127, 2015.
- [52] M. Ormaza, N. Bachellier, M. N. Faraggi, B. Verlhac, P. Abufager, P. Ohresser, L. Joly, M. Romeo, F. Scheurer, M. L. Bocquet, N. Lorente, and L. Limot, “Efficient spin-flip excitation of a nickelocene molecule,” *Nano Letters*, vol. 17, pp. 1877–1882, 2017.
- [53] J. Soler, E. Artacho, J. D. Gale, A. García, J. Junquera, P. Ordejón, and D. Sánchez-Portal, “The siesta method for \textit{Ab Initio} order-n materials simulation,” *Journal of Physics: Condensed Matter*, vol. 14, pp. 2745–2779, 2002.
- [54] I. E. Brumboiu, S. Haldar, J. Lüder, O. Eriksson, H. C. Herper, B. Brena, and B. Sanyal, “Influence of Electron Correlation on the Electronic Structure and Magnetism of Transition-Metal Phthalocyanines,” *Journal of Chemical Theory and Computation*, vol. 12, no. 4, pp. 1772–1785, 2016.
- [55] S. Vancoillie, H. Zhao, V. Tran, M. F. Hendrickx, and K. Pierloot, “Multiconfigurational second-order perturbation theory restricted active space (raspt2) studies on mononuclear first-row transition-metal systems,” *Journal of Chemical Theory and Computation*, vol. 7, pp. 3961–3977, 2011.
- [56] M.-S. Liao, J. Watts, and M.-J. Huang, “Electronic structure of some substituted iron(ii) porphyrins. are they intermediate or high spin?,” *Journal of Physical Chemistry A*, vol. 111, pp. 5927–5935, 2007.
- [57] M. A. Ruderman and C. Kittel, “Indirect Exchange Coupling of Nuclear Magnetic Moments by Conduction Electrons,” *Physical Review*, vol. 96, no. 3, pp. 72–75, 1954.
- [58] T. Kasuya, “A Theory of Metallic Ferro- and Antiferromagnetism on Zener’s Model,” *Progress of Theoretical Physics*, vol. 16, no. 1, pp. 45–57, 1956.
- [59] K. Yosida, “Magnetic Properties of Cu-Mn Alloys,” *Physical review*, vol. 106, no. I, pp. 893–898, 1957.

- [60] H. A. Kramers, "L'INTERACTION ENTRE LES ATOMES MAGNETOGENES DANS UN CRISTAL PARAMAGNETIQUE," *Physica*, vol. 1, p. 182, 1934.
- [61] P. W. Anderson, "Antiferromagnetism. Theory of Superexchange Interaction," *Physical Review*, vol. 79, no. 2, pp. 350–356, 1950.
- [62] C. Kittel, "Indirect Exchange Interactions in Metals," *Solid State physics*, vol. 22, p. 1, 1968.
- [63] H. M. McConnell, "Intramolecular Charge Transfer in Aromatic Free Radicals," vol. 508, 1961.
- [64] M. Treier, C. A. Pignedoli, T. Laino, R. Rieger, K. Mu, D. Passerone, and R. Fasel, "Surface-assisted cyclodehydrogenation provides a synthetic route towards easily processable and chemically tailored nanographenes Å," vol. 3, no. November 2010, pp. 61–67, 2011.
- [65] C. Rubio-Verdú, A. Sarasola, D.-J. Choi, Z. Majzik, R. Ebeling, M. R. Calvo, M. M. Ugeda, A. Garcia-Lekue, D. Sánchez-Portal, and J. I. Pascual, "Orbital-selective spin excitation of a magnetic porphyrin," *Communications Physics*, vol. 1, p. 15, 2018.
- [66] S. Karan, M. Karolak, D. Jacob, N. Lorente, and R. Berndt, "Spin control induced by molecular charging in a transport junction Spin control induced by molecular charging in a transport junction," 2017.
- [67] J. Li, N. Merino-díez, E. Carbonell-sanromà, M. Vilas-varela, D. G. D. Oteyza, D. Peña, M. Corso, and J. I. Pascual, "Survival of spin state in magnetic porphyrins contacted by graphene nanoribbons," no. February, 2018.
- [68] D. Jacob, "Renormalization of single-ion magnetic anisotropy in the absence of the Kondo effect," *Physical Review B*, vol. 97, no. 7, pp. 1–8, 2018.
- [69] H. Kamerlingh Onnes, "No Title," *Leiden Comm.*, vol. 120b, 122b, 1911.
- [70] W. Meissner and R. Ochsenfeld, "No Title," *Naturwissenschaften*, vol. 21, p. 787, 1933.
- [71] W. S. Corak, B. B. Goodman, C. B. Satterthwaite, and A. Wexler, "Exponential Temperature Dependence of the Electronic Specific Heat of Superconducting Vacuum," *Physical Review*, vol. 108, no. 5, p. 1442, 1954.
- [72] W. S. Corak, B. B. Goodman, C. B. Satterthwaite, and A. Wexler, "Atomic Heats of Normal and Superconducting Vanadium," *Phys. Rev.*, vol. 102, no. 1699, pp. 656–661, 1956.
- [73] J. Bardeen, L. N. Cooper, and J. R. Schrieffer, "Theory of Superconductivity," *Physical Review*, vol. 108, no. 5, p. 1175, 1957.
- [74] M. Tinkham, *Introduction to Superconductivity*. 1973.

- [75] V. L. Ginzburg and L. D. Landau, "No Title," *Fiz., Zh. Eksperim. i Teor.*, vol. 20, p. 1064, 1950.
- [76] L. P. Gor'kov, "Microscopic derivation of the Ginzburg-Landau equations in the theory of superconductivity," *Sov. Phys. JETP*, vol. 9, no. 6, p. 1364, 1959.
- [77] B. D. Josephson, "Possible new effects in superconductive tunnelling," *Physics Letters*, vol. 1, no. 7, pp. 251–253, 1962.
- [78] M. Ruby, B. W. Heinrich, J. I. Pascual, and K. J. Franke, "Experimental demonstration of a two-band superconducting state for lead using scanning tunnelling spectroscopy," *Physical Review Letters*, vol. 114, no. 15, pp. 1–5, 2015.
- [79] A. Floris, A. Sanna, S. Massidda, and E. K. U. Gross, "Two-band superconductivity in Pb from ab initio calculations," *Physical Review B*, vol. 75, p. 054508, 2007.
- [80] I. Y. Sklyadneva, R. Heid, P. M. Echenique, K. B. Bohnen, and E. V. Chulkov, "Electron-phonon interaction in bulk Pb: Beyond the Fermi surface," *Physical Review B - Condensed Matter and Materials Physics*, vol. 85, no. 15, pp. 1–6, 2012.
- [81] G. Rochlin, "Determination of the anisotropy of the energy gap in superconducting Pb by superconductive tunnelling," *Physical Review*, vol. 153, pp. 513–532, 1967.
- [82] L. S. Norman, "Far-Infrared Absorption Spectra of Thick Superconducting Films," *Physical Review*, vol. 167, no. 2, pp. 393–407, 1968.
- [83] E. N. Bratus', V. S. Shumeiko, and G. Wendin, "Theory of Subharmonic Gap Structure in Superconducting Mesoscopic Tunnel Contacts," *Physical Review Letters*, vol. 74, no. 11, pp. 2110–2113, 1995.
- [84] J. Cuevas, A. Martín-Rodero, and A. L. Yeyati, "Hamiltonian approach to the transport properties of superconducting quantum point contacts," *Physical Review B - Condensed Matter and Materials Physics*, vol. 54, no. 10, pp. 7366–7379, 1996.
- [85] M. Hurd, S. Datta, and P. F. Bagwell, "Current-voltage relation for asymmetric ballistic superconducting junctions," *Physical Review B*, vol. 54, no. 9, pp. 6557–6567, 1996.
- [86] M. Hurd, S. Datta, and P. F. Bagwell, "Ac Josephson effect for asymmetric superconducting junctions," *Physical Review B - Condensed Matter and Materials Physics*, vol. 56, no. 17, pp. 11232–11245, 1997.
- [87] M. Ternes, W. D. Schneider, J. C. Cuevas, C. P. Lutz, C. F. Hirjibehedin, and A. J. Heinrich, "Subgap structure in asymmetric superconducting tunnel

- junctions,” *Physical Review B - Condensed Matter and Materials Physics*, vol. 74, no. 13, pp. 3–6, 2006.
- [88] A. I. Rusinov, “On the Theory of Gapless Superconductivity in Alloys Containing Paramagnetic Impurities,” *Soviet Journal of Experimental and Theoretical Physics*, vol. 29, no. 6, p. 1101, 1969.
- [89] N. Hatter, B. W. Heinrich, M. Ruby, J. I. Pascual, and K. J. Franke, “Magnetic anisotropy in Shiba bound states across a quantum phase transition,” *Nature Communications*, vol. 6, pp. 1–6, 2015.
- [90] D. M. Ginsberg, “Consequences of Shiba’s theory of magnetic impurities in superconductors, beyond s-wave scattering,” *Physical Review B*, vol. 20, no. 3, pp. 960–962, 1979.
- [91] A. B. Kunz and D. M. Ginsberg, “JSNP,” vol. 22, no. 7, 1980.
- [92] M. E. Flatté and J. M. Byers, “Local electronic structure of a single magnetic impurity in a superconductor,” *Physical Review Letters*, vol. 78, no. 19, pp. 3761–3764, 1997.
- [93] R. Žitko, O. Bodensiek, and T. Pruschke, “Effects of magnetic anisotropy on the subgap excitations induced by quantum impurities in a superconducting host,” *Physical Review B - Condensed Matter and Materials Physics*, vol. 83, no. 5, pp. 30–32, 2011.
- [94] Y. Kim, J. Zhang, E. Rossi, and R. M. Lutchyn, “Impurity-Induced Bound States in Superconductors with Spin-Orbit Coupling,” *Physical Review Letters*, vol. 114, no. 23, pp. 1–5, 2015.
- [95] M. Ruby, F. Pientka, Y. Peng, F. Von Oppen, B. W. Heinrich, and K. J. Franke, “Tunneling Processes into Localized Subgap States in Superconductors,” *Physical Review Letters*, vol. 115, no. 8, pp. 1–5, 2015.
- [96] D. J. Choi, C. Rubio-Verdú, J. De Bruijckere, M. M. Ugeda, N. Lorente, and J. I. Pascual, “Mapping the orbital structure of impurity bound states in a superconductor,” *Nature Communications*, vol. 8, no. May, pp. 1–6, 2017.
- [97] M. Salkola and A. Balatsky, “Spectral properties of quasiparticle excitations induced by magnetic moments in superconductors,” *Physical Review B - Condensed Matter and Materials Physics*, vol. 55, no. 18, pp. 12648–12661, 1997.
- [98] T. Matsuura, “The Effects of Impurities on Superconductors with Kondo Effect,” *Prog. Theo. Phys.*, vol. 57, no. 6, pp. 1823–1835, 1977.
- [99] O. Sakai, Y. Shimizu, H. Shiba, and K. Satori, “Numerical Renormalization Group Study of Magnetic Impurities in Superconductors. II. Dynamical Excitation Spectra and Spatial Variation of the Order Parameter,” 1993.

- [100] A. V. Balatsky, I. Vekhter, and J. X. Zhu, “Impurity-induced states in conventional and unconventional superconductors,” *Reviews of Modern Physics*, vol. 78, no. 2, pp. 373–433, 2006.
- [101] J. Bauer, J. I. Pascual, and K. J. Franke, “Microscopic resolution of the interplay of Kondo screening and superconducting pairing: Mn-phthalocyanine molecules adsorbed on superconducting Pb(111),” *Physical Review B - Condensed Matter and Materials Physics*, vol. 87, no. 7, pp. 1–7, 2013.
- [102] P. W. Anderson, “Absence of diffusion in certain random lattices,” *Physical Review*, vol. 109, no. 5, pp. 1492–1505, 1958.
- [103] F. Wegner, “Inverse participation ratio in $2+\delta$ dimensions,” *Zeitschrift für Physik B Condensed Matter and Quanta*, vol. 36, pp. 209–214, 1980.
- [104] C. Castellani and L. Peliti, “Multifractal wavefunction at the localisation threshold,” *J. Phys. A: Math. Gen.*, vol. 19, pp. L429–L432, 1986.
- [105] A. D. Mirlin and F. Evers, “Multifractality and critical fluctuations at the Anderson transition,” *Physical Review B - Condensed Matter and Materials Physics*, vol. 62, no. 12, pp. 7920–7933, 2000.
- [106] M. Morgenstern, J. Klijn, C. Meyer, and R. Wiesendanger, “Real-Space Observation of Drift States in a Two-Dimensional Electron System at High Magnetic Fields,” *Physical Review Letters*, vol. 90, no. 5, p. 56804, 2003.
- [107] K. Hashimoto, C. Sohrmann, J. Wiebe, T. Inaoka, F. Meier, Y. Hirayama, R. A. Römer, R. Wiesendanger, and M. Morgenstern, “Quantum hall transition in real space: From localized to extended states,” *Physical Review Letters*, vol. 101, no. 25, p. 256802, 2008.
- [108] M. Mondal, A. Kamlapure, M. Chand, G. Saraswat, S. Kumar, J. Jesudasan, L. Benfatto, V. Tripathi, and P. Raychaudhuri, “Phase fluctuations in a strongly disordered s-wave nbn superconductor close to the metal-insulator transition,” *Physical Review Letters*, vol. 106, no. 4, p. 47001, 2011.
- [109] C. Brun, T. Cren, V. Cherkez, F. Debontridder, S. Pons, D. Fokin, M. C. Tringides, S. Bozhko, L. B. Io, B. L. Altshuler, and D. Roditchev, “layers of lead on silicon,” vol. 10, no. June, pp. 444–450, 2014.
- [110] B. Sacépé, T. Dubouchet, C. Chapelier, M. Sanquer, M. Ovadia, D. Shahar, M. Feigel, and L. Ioffe, “Localization of preformed Cooper pairs in disordered superconductors,” *Nature Physics*, vol. 7, no. 3, pp. 239–244, 2011.
- [111] G. Lemarié, A. Kamlapure, D. Bucheli, L. Benfatto, J. Lorenzana, G. Seibold, S. C. Ganguli, P. Raychaudhuri, and C. Castellani, “Universal scaling of the order-parameter distribution in strongly disordered superconductors,” *Physical Review B*, vol. 87, no. 18, p. 184509, 2013.

- [112] Y. Noat, V. Cherkez, C. Brun, T. Cren, C. Carbillet, F. Debontridder, K. Ilin, M. Siegel, A. Semenov, H.-W. Hübers, and D. Roditchev, “Unconventional superconductivity in ultrathin superconducting NbN films studied by scanning tunneling spectroscopy,” *Physical Review B*, vol. 88, no. 1, p. 14503, 2013.
- [113] N. Trivedi, J. P. Conf, N. Trivedi, Y. L. Loh, and K. Bouadim, “Related content Emergent granularity and pseudogap near the superconductor-insulator transition Emergent granularity and pseudogap near the superconductor-insulator transition,” 2012.
- [114] M. V. Feigel'man, L. B. Ioffe, V. E. Kravtsov, and E. A. Yuzbashyan, “Eigenfunction Fractality and Pseudogap State near the Superconductor-Insulator Transition,” vol. 027001, no. January, pp. 1–4, 2007.
- [115] M. V. Feigel'man, L. B. Ioffe, V. E. Kravtsov, and E. Cuevas, “Fractal superconductivity near localization threshold,” *Annals of Physics*, vol. 325, no. 7, pp. 1390–1478, 2010.
- [116] I. S. Burmistrov, I. V. Gornyi, and A. D. Mirlin, “Enhancement of the critical temperature of superconductors by anderson localization,” *Physical Review Letters*, vol. 108, no. 1, p. 17002, 2012.
- [117] J. Mayoh and A. M. García-García, “Global critical temperature in disordered superconductors with weak multifractality,” *Physical Review B - Condensed Matter and Materials Physics*, vol. 92, no. 17, p. 174526, 2015.
- [118] N. Roch, S. Florens, T. A. Costi, W. Wernsdorfer, and F. Balestro, “Observation of the underscreened kondo effect in a molecular transistor,” *Physical Review Letters*, vol. 103, no. 19, pp. 1–4, 2009.
- [119] N. Hatter, B. W. Heinrich, D. Rolf, and K. J. Franke, “Scaling of Yu-Shiba-Rusinov energies in the weak-coupling Kondo regime,” *Nature Communications*, vol. 8, no. 1, pp. 1–7, 2017.
- [120] M. Ternes, C. González, C. P. Lutz, P. Hapala, F. J. Giessibl, P. Jelínek, and A. J. Heinrich, “Interplay of conductance, force, and structural change in metallic point contacts,” *Physical Review Letters*, vol. 106, no. 1, pp. 1–4, 2011.
- [121] M. Paulsson, T. Frederiksen, and M. Brandbyge, “Phonon scattering in nanoscale systems: Lowest order expansion of the current and power expressions,” *Journal of Physics: Conference Series*, vol. 35, no. 1, pp. 247–254, 2006.
- [122] T. Frederiksen, M. Paulsson, M. Brandbyge, and A. P. Jauho, “Inelastic transport theory from first principles: Methodology and application to nanoscale devices,” *Physical Review B - Condensed Matter and Materials Physics*, vol. 75, no. 20, pp. 1–22, 2007.

- [123] M. Chhowalla, H. S. Shin, G. Eda, L. J. Li, K. P. Loh, and H. Zhang, “The chemistry of two-dimensional layered transition metal dichalcogenide nanosheets,” *Nature Chemistry*, vol. 5, no. 4, pp. 263–275, 2013.
- [124] M. M. Ugeda, A. J. Bradley, Y. Zhang, S. Onishi, Y. Chen, W. Ruan, C. Ojeda-Aristizabal, H. Ryu, M. T. Edmonds, H. Z. Tsai, A. Riss, S. K. Mo, D. Lee, A. Zettl, Z. Hussain, Z. X. Shen, and M. F. Crommie, “Characterization of collective ground states in single-layer NbSe₂,” *Nature Physics*, vol. 12, no. 1, pp. 92–97, 2016.
- [125] S. Barja, S. Wickenburg, Z.-f. Liu, Y. Zhang, H. Ryu, M. M. Ugeda, Z. Hussain, Z.-x. Shen, S.-k. Mo, E. Wong, M. B. Salmeron, F. Wang, M. F. Crommie, D. F. Ogletree, J. B. Neaton, and A. Weber-bargioni, “Charge density wave order in 1D mirror twin boundaries of single-layer MoSe₂,” vol. 12, no. August, 2016.
- [126] R. F. Frindt, “Superconductivity in Ultrathin NbSe₂ Layers,” *Physical Review Letters*, vol. 28, no. 5, pp. 299–301, 1972.
- [127] N. E. Staley, J. Wu, P. Eklund, and Y. Liu, “Electric field effect on superconductivity in atomically thin flakes of NbSe₂,” pp. 1–6, 2009.
- [128] Y. Cao, A. Mishchenko, G. Yu, E. Khestanova, A. P. Rooney, E. Prestat, A. V. Kretinin, P. Blake, M. B. Shalom, C. Woods, J. Chapman, I. Grigorieva, K. S. Novoselov, B. Piot, M. Potemski, T. Taniguchi, S. J. Haigh, A. K. Geim, and R. V. Gorbachev, “Quality heterostructures from two dimensional crystals unstable in air by their assembly in inert atmosphere Quality heterostructures from two dimensional crystals unstable in air by their assembly in inert atmosphere,” 2015.
- [129] S. Onishi, M. M. Ugeda, Y. Zhang, Y. Chen, C. Ojeda-aristizabal, H. Ryu, S.-k. Mo, Z. Hussain, Z.-x. Shen, M. F. Crommie, and A. Zettl, “) of superconductivity as the layer number is reduced and predicted the monolayer T,” pp. 3–6, 2016.
- [130] K. Bouadim, Y. L. Loh, M. Randeria, and N. Trivedi, “Single- and two-particle energy gaps across the disorder-driven superconductor-insulator transition,” *Nature Physics*, vol. 7, no. 11, pp. 884–889, 2011.
- [131] C. J. Arguello, E. P. Rosenthal, E. F. Andrade, W. Jin, P. C. Yeh, N. Zaki, S. Jia, R. J. Cava, R. M. Fernandes, A. J. Millis, T. Valla, R. M. Osgood, and A. N. Pasupathy, “Quasiparticle interference, quasiparticle interactions, and the origin of the charge density wave in 2H-NbSe₂,” *Physical Review Letters*, vol. 114, no. 3, p. 37001, 2015.
- [132] K. K. Gomes, A. N. Pasupathy, A. Pyshp, S. Ono, Y. Ando, and A. Yazdani, “Visualizing pair formation on the atomic scale in the,” *Nature*, vol. 447, no. May, pp. 569–572, 2007.

- [133] M. H. Hamidian, S. D. Edkins, S. H. Joo, A. Kostin, H. Eisaki, S. Uchida, M. J. Lawler, E. A. Kim, A. P. Mackenzie, K. Fujita, J. Lee, and J. C. Séamus Davis, “Detection of a Cooper-pair density wave in $\text{Bi}_2\text{Sr}_2\text{CaCu}_2\text{O}_{8+x}$,” *Nature*, vol. 532, pp. 343–347, 2016.
- [134] M. V. Feigei'man, L. B. Ioffe, V. E. Kravtsov, and E. A. Yuzbashyan, “Eigenfunction fractality and pseudogap state near the superconductor- insulator transition,” *Physical Review Letters*, vol. 98, no. 2, p. 27001, 2007.
- [135] V. I. Falko and K. B. Efetov, “Multifractality: Generic property of eigenstates of 2d disordered metals,” *EPL*, vol. 32, no. 8, pp. 627–632, 1995.

Publications

PhD Thesis

- *Orbital-selective spin excitation of a magnetic porphyrin*
Carmen Rubio-Verdú, Ane Sarasola, Deung-Jang Choi, Zsolt Majzik, René Ebeling, M. Reyes Calvo, Miguel M. Ugeda, Aran Garcia-Lekue, Daniel Sánchez-Portal and José Ignacio Pascual
Communications Physics, **1**, 15 (2018)
- *Influence of Magnetic Ordering between Cr Adatoms on the Yu-Shiba-Rusinov States of the β -Bi₂Pd Superconductor*
Deung-Jang Choi, Carlos García Fernández, Edwin Herrera, Carmen Rubio-Verdú, Miguel M. Ugeda, Isabel Guillamón, Hermann Suderow, José Ignacio Pascual and Nicolás Lorente
Physical Review Letters **120**, 167001 (2018)
- *Mapping the orbital structure of impurity bound states in a superconductor*
Deung-Jang Choi, Carmen Rubio-Verdú, Joeri de Bruijckere, Miguel M. Ugeda, Nicolás Lorente and José Ignacio Pascual
Nature Communications **8**, 15175 (2017)
- *Spin-polarised edge states in atomic Mn chains supported on Cu₂N*
Deung-Jang Choi, Roberto Robles, Jean-Pierre Gauyacq, Carmen Rubio-Verdú, Nicolás Lorente and José Ignacio Pascual
Journal of Physics: Condensed Matter **28**. 23LT01. (2016)
- *Real-space visualization of multifractal superconductivity in single-layer NbSe₂*
Carmen Rubio-Verdú, Antonio M. García-García, Hyejin Ryu, Deung-Jang Choi, Javier Zaldívar, Shujie Tang, Zhi-Xun Shen, Sung-Kwan Mo, José Ignacio Pascual and Miguel M. Ugeda
Submitted

- *Robustness of Yu-Shiba-Rusinov resonances in presence of a complex superconducting order parameter*

Jacob Senkpiel, Carmen Rubio-Verdú, Markus Etzkorn, Robert Drost, Leslie M. Schoop, Simon Dambach, Ciprian Padurariu, Björn Kubala, Joachim Ankerhold, Christian R. Ast and Klaus Kern

Submitted

Master Thesis

- *Graphene flakes obtained by local electro-exfoliation of graphite with a STM tip*

Carmen Rubio-Verdú, Giovanni Sáenz-Arce, Jesús Martínez-Asencio, David C. Milan, Mohammed Moaied, Juan José Palacios, María José Caturla and Carlos Untiedt

Physical Chemistry Chemical Physics **19**, 8061 (2017)

Resumen Extendido

Esta Tesis estudia los fenómenos de magnetismo y superconducibilidad a escala atómica por medio de Microscopía y Espectroscopía de Efecto Túnel a bajas temperaturas (STM/STS) en condiciones de ultra-alto vacío. Estos resultados han sido obtenidos en colaboración con el grupo del Prof. Nicolás Lorente y del Prof. Daniel Sánchez-Portal, que realizaron simulaciones *ab initio* de Teoría del Funcional de Denstidad (DFT). Las nuevas plataformas moleculares utilizadas para el estudio de acople magnético fueron sintetizadas en el grupo del Prof. Pei Nian Liu en colaboración con el grupo del Prof. Nian Lin. El modelo analítico que predice las variaciones espaciales del gap superconductor, gobernadas por estados multifractales, ha sido desarrollado por el Prof. Antonio M. García-García.

El magnetismo es un fenómeno colectivo que emerge debido a dos efectos mecanocuánticos: el espín y la interacción de canje. Un material cuyos átomos tienen electrones desapareados en sus orbitales *d*, tendrán asociado un espín que puede alinearse paralela o antiparalelamente con el espín de un átomo vecino a través de la interacción de canje, dando lugar a orden ferromagnético o antiferromagnético, respectivamente. Si reducimos el tamaño del sistema hasta llegar a un solo átomo, veremos que no existe una dirección preferencial para que los espines se orienten: los átomos son isótropos. Y aquí es donde recae la importancia de la anisotropía magnética, que rompe la degeneración de las tres direcciones del espacio y proporciona al átomo una dirección preferencial para orientar su espín. Cuando medimos la energía de la anisotropía magnética, medimos la estabilidad de la magnetización.

Los discos duros que utilizamos para almacenar información funcionan con memorias magnéticas. y la industria tecnológica demanda reducir las dimensiones de sus componentes cada vez más. El problema surge al reducir el tamaño del material hasta tal punto que pierde la capacidad de mantener su magnetización: es lo que se conoce como el límite superparamagnético. Por lo tanto, el avance tecnológico necesita de nuevos sistemas magnéticos que sean estables en la escala nanométrica, lo que lleva irremediablemente a la necesidad de desarrollar estudios fundamentales que arrojen luz sobre los mecanismos que gobiernan los espines atómicos.

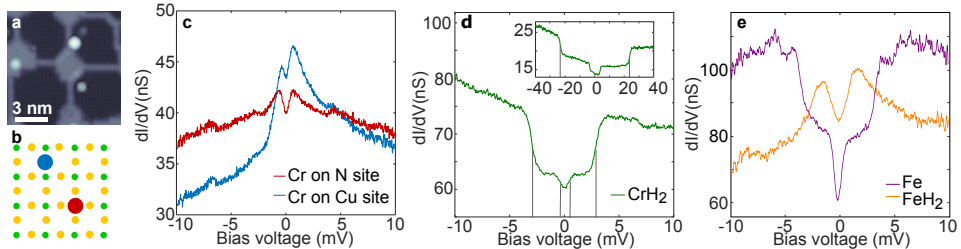


Figure 1: a, Imagen topográfica de STM con resolución atómica de la superficie de Cu₂N con átomos de cromo adsorbidos en el Cu (azul) y en el N (rojo). b, Dibujo de la superficie de Cu₂N con los átomos de Cu en amarillo, los de N en verde y los adátomos de Cr adsorbidos en Cu (azul) y N (rojo). c, Espectroscopía túnel de los átomos de Cr adsorbidos en el Cu (azul) y en el nitrógeno (rojo). ($V_S = 10$ mV, $I = 400$ pA, $V_{rms} = 50$ μ V). d, Espectroscopía túnel de un átomo de Cr hidrogenado (CrH₂). Se incluye un espectro de mayor energía ($V_S = 10$ mV, $V_S = 40$ mV, $I = 1$ nA, $V_{rms} = 50$ μ V). e, Espectroscopía túnel comparando un espectro tomado en el Fe (púrpura) y otro en el FeH₂ (naranja) ($V_S = 10$ mV, $I = 1$ nA, $V_{rms} = 50$ μ V).

En esta Tesis presentamos varias plataformas para entender y profundizar en los mecanismos fundamentales que rigen el magnetismo atómico. El primer impedimento que nos encontramos al colocar un átomo magnético en una superficie, es el apantallamiento de su espín por el mar de electrones del metal. Una manera de desacoplar el momento magnético es utilizando capas aislantes, como el nitruro de cobre Cu₂N. En la Fig. 1a se muestra una imagen de STM con resolución atómica de los parches de Cu₂N. Las zonas brillantes corresponden al cristal de Cu(100) que se encuentra debajo, visible debido a la incommensurabilidad de ambos materiales [23]. Tras depositar átomos de cromo encima se vio que éstos se adsorben en dos posiciones distintas: sobre un átomo de cobre o sobre uno de nitrógeno, como se muestra en la Fig. 1b.

La espectroscopía túnel nos permite acceder al espín de un átomo magnético mediante su excitación intelástica, debido a la transferencia de energía y momento angular por parte de los electrones túnel. En la Fig. 1c mostramos los espectros obtenidos para impurezas de Cr en los dos lugares de adsorción. En ambas configuraciones existe una apertura al nivel de Fermi que interpretamos en términos de excitaciones de espín inelásticas [24]. Adicionalmente, los átomos que se encuentran encima del Cu de la superficie muestran una resonancia centrada a voltaje cero que surge como resultado del acople con los electrones de conducción: es lo que se denomina el efecto Kondo [7, 21, 22].

Las simulaciones de DFT obtienen un espín $S = 5/2$ para Cr sobre N, y

una configuración de anisotropía magnética en el plano de $D = 0.15$, $E = 0$ meV. Con el objetivo de manipular el momento magnético de los átomos de Cr, expusimos la muestra a una atmósfera de hidrógeno. Las moléculas de hidrógeno reaccionan con el Cr y se enlazan a él, cambiando sus propiedades magnéticas por completo. La espectroscopía tomada en los compuestos CrH₂ muestra un aumento sustancial de la anisotropía magnética ($D = -1.55$, $E = 0.35$ meV), visible como escalones a mayores energías (Fig. 1d) si lo comparamos con el átomo sin hidrógeno. Para comprobar cómo la adsorción de hidrógeno afecta a los distintos metales de transición, repetimos el mismo experimento con hierro en lugar de cromo. En la Fig. 1e mostramos la espectroscopía de Fe y FeH₂. La adsorción de hidrógeno tiene dos efectos: reducir el valor de anisotropía de $D = -1.55$, $E = 0.31$ meV a $D = 0.38$, $E = 0$ meV, y aumentar el acople con la superficie, visible en la resonancia que emerge a energía cero. Por lo tanto, podemos concluir que es posible manipular el momento magnético de los átomos de metales de transición mediante la adsorción de una molécula de hidrógeno.

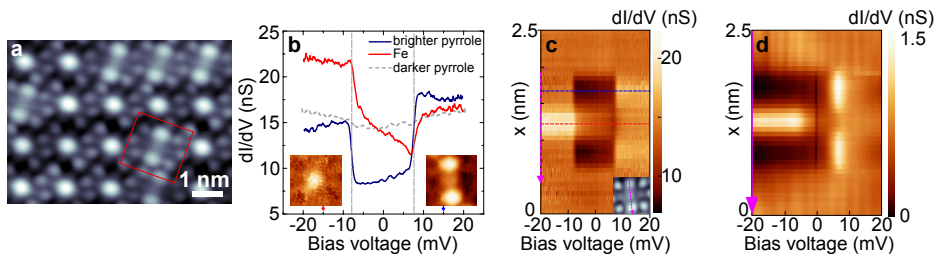


Figure 2: **a,** Imagen topográfica de STM de una isla de porfirinas de hierro **b,** Espectroscopía dI/dV característica de las moléculas FeTPP medida sobre uno de los dos pirroles brillantes (azul) y sobre el Fe (rojo). Como referencia, se muestra un espectro medido sobre un pirrol oscuro (gris) ($V_S = 20$ mV, $I = 300$ pA, $V_{rms} = 50\mu V$). **c,** Mapa de la excitación de espín a lo largo de la molécula. **d,** Mapa de orbitales a lo largo de la molécula.

Otra aproximación para estudiar el momento magnético atómico son los imanes moleculares, que muestran un espín protegido por una anisotropía magnética alta. Sin embargo, cuando se depositan en una superficie, emergen interacciones entre los electrones de conducción y el espín. En la Fig. 2a se muestra una imagen de STM de unas porfirinas de hierro depositadas sobre Au(111). Al analizar los detalles de la excitación de espín en distintas posiciones de la molécula, vimos que su forma variaba considerablemente al tomar la curva dI/dV en el pirrol o en el hierro, siendo mucho más asimétrica en el hierro (Fig. 2b,c).

Las porfirinas de hierro tienen un espín entero que se distribuye a lo largo de toda la molécula. El momento magnético se encuentra en dos orbitales polarizados en espín hibridado con estados moleculares, cuya interacción con el sustrato lleva a ambos fuera de la simetría de electrón-hueco debido a la presencia de Potential Scattering \mathcal{U} . Cada orbital da lugar a un camino de excitación, y el signo de \mathcal{U} marca la asimetría de la excitación de espín.

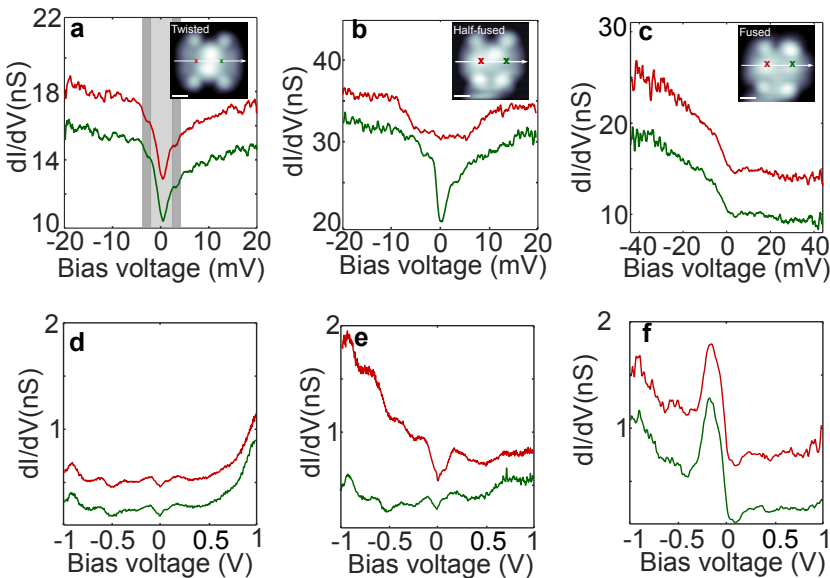


Figure 3: Espectroscopía dI/dV de corto (a, b, c) y largo (d, e, f,) rango medida en ambos Fe como se indica en la imagen. La escala representa 5 Å.

Un paso más allá en el estudio de espines individuales es investigar el efecto de una segunda impureza magnética. En la Fig. 3 mostramos la espectroscopía tomada en una plataforma orgánica bimetálica, en la que se esperan interacciones espín-espín. Simulaciones de DFT encontraron que en dicho sistema existía una fuerte interacción de canje entre los dos átomos de hierro. Sin embargo, al depositar la doble porfirina en la superficie del oro, encontramos que cada átomo magnético era independiente. Además, la molécula reacciona intramolecularmente, activada por la superficie, generando tres especies distintas de doble porfirina. Cada una de ellas muestra una configuración de anisotropía magnética distinta, como sugiere la espectroscopía túnel que se muestra en Fig. 3a-c. Su estructura orbital también se ve afectada por la reacción intramolecular (Fig. 3d-f). Estos resultados sugieren que el acople de la estructura orgánica con los electrones de conducción del oro hace que el acople de canje entre los Fe desaparezca y haga que cada espín se comporte de manera independiente.

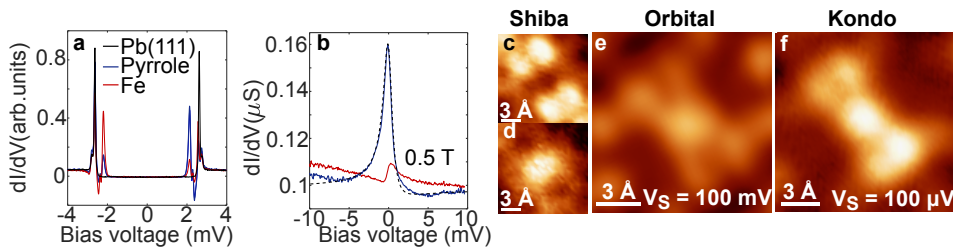


Figure 4: FeTPP brillantes. a, Espectroscopía túnel tomada en el pirrol (azul) y en el Fe (rojo) de una molécula de FeTPP. Se muestra el espectro tomado en la superficie de Pb(111) como referencia. b, Resonancias Fano tomadas en la posición del pirrol y del hierro bajo la influencia de un campo magnético externo de $B=0.5$ T. c, d, Mapas de conductancia de los estados Shiba de partícula y hueco. e, Mapa de conductancia tomado a altura constante a $V_S = +100$ mV. f, Mapa de conductancia Kondo tomado a altura constante a $V_S = +100$ μ V ($B = 0.5$ T).

Los sustratos superconductores son una plataforma única para investigar espines individuales. Su interacción da lugar a estados ligados localizados protegidos por el gap superconductor que exhiben tiempos de vida largos, lo cual permite el estudio de los fenómenos magnéticos con gran resolución energética. En este contexto, el espín entero de las porfirinas de hierro se hibrida con el plomo superconductor, dando lugar a multiples estados ligados Shiba como se puede observar en la Fig. 4a. Aplicando un campo magnético externo se destruye el estado superconductor de punta y muestra. En la Fig. 4b se muestra la espectroscopía tomada en la molécula FeTPP en el estado normal, que revela huellas del efecto Kondo. Analizando la distribución espacial de los estados Shiba en Fig. 4c,d vemos que su convolución se corresponde tanto con la distribución de la resonancia Kondo (Fig. 4e) como con un orbital vacío cerca del nivel de Fermi (Fig. 4f). De la respuesta de la resonancia Kondo al campo magnético y a la subida de la temperatura vemos que el espín $S = 1$ se encuentra en el régimen de acople fuerte ($T \ll T_K$) en un estado de underscreened Kondo.

Además de las moléculas brillantes que muestran estados Shiba en el Pb(111), encontramos otro tipo de moléculas que además de las resonancias Shiba dentro del gap superconductor, presentan picos extra fuera del gap, que corresponden a anisotropía magnética que prevalece debido al bajo acople con el sustrato (Fig. 5a). La punta del STM interacciona de manera diferente a lo largo de la molécula, provocando cambios en los valores de anisotropía D y E (Fig. 5b). Reduciendo la distancia punta-muestra en el centro de la porfirina (Fig. 5c), vimos que existen dos regímenes de inter-

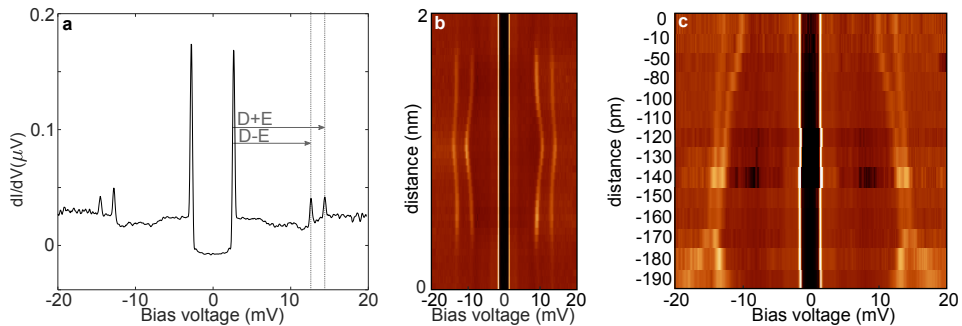


Figure 5: FeTPP oscuras. a, Espetroscopía dI/dV tomada en una molécula oscura que muestra picos de anisotropía magnética, como se indica con las flechas ($V_S = 20$ mV, $I = 1$ nA, $V_{rms} = 30$ μ V). b Mapa de excitación tomado a lo largo de la molécula que se muestra en a, mostrando diferencias de anisotropía dependiendo de la posición de la punta ($V_S = 20$ mV, $I = 1$ nA, $V_{rms} = 30$ μ V).

acción: al principio, la punta atrae al átomo de Fe fuera del plano, lo que aumenta el valor de D y disminuye el de E . A partir de -160 pm, se entra en el régimen repulsivo, que empuja el átomo de hierro hacia la superficie y hace que aumenten los valores de anisotropía D y E .

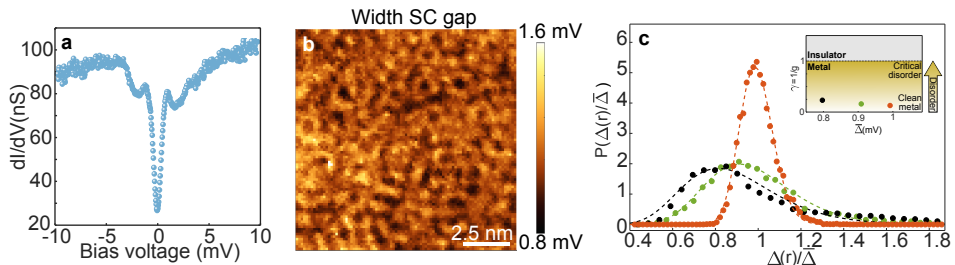


Figure 6: a, Espectroscopía dI/dV obtenida en una isla de $NbSe_2$, mostrando el gap superconductor y el gap de la Charge Density Wave ($V_S = 5$ mV, $I = 1$ nA, $V_{rms} = 20$ μ V). b, Distribución espacial de la anchura del gap superconductor. c, Distribución de probabilidad del tamaño del gap superconductor normalizado al valor medio, para distintos valores de desorden.

Finalmente, motivados por la búsqueda de nuevas plataformas superconductoras, investigamos el superconductor cristalino bidimensional $NbSe_2$. Debido a la presencia de acople espín-órbita fuerte, presenta un estado fundamental metálico a bajas temperaturas. Además, presenta un estado superconductor por debajo de $T = 1.9$ K. La espectroscopía túnel muestra un

gap superconductor lejos de ser simétrico, además de cambiar en forma y tamaño en distintas posiciones de las islas de NbSe₂ (Fig. 6a).

El mapa de la distribución del gap superconductor muestra oscilaciones de su valor en el rango de 0.8-1.6 mV para una zona determinada (Fig. 6b). Dichas variaciones se deben a la presencia de desorden débil, que favorece la aparición de estados multifractales que gobiernan las características locales del parámetro de orden. A pesar de las fluctuaciones espaciales del gap superconductor, la coherencia de fase se mantiene, y el estado superconductor se manifiesta en la escala mesoscópica. Esto es visible en la distribución de probabilidad del gap superconductor que se muestra en la Fig. 6c. La asimetría en la distribución es una huella de estados multifractales, donde una mayor asimetría implica un mayor nivel de desorden.

